10.05 Gravity and Topography of the Terrestrial Planets

MA Wieczorek, University Paris Diderot, Paris Cedex 13, France

10.05.1 Introduction

One of the most precise ways to investigate the subsurface structure of a planet is through the analysis of seismic waves. While such endeavors have proved to be remarkably successful for Earth, the emplacement of a geophysical network that includes seismometers on a terrestrial body such as Mercury, Venus, Mars, or the Moon is both costly and technologically challenging (see Chapter 10.03). Fortunately, alternative means exist to probe the interior structure of the terrestrial planets from orbit. One such method, reviewed in Chapter 10.04, is through analyses of a planet's time-variable rotation. By the measurement of precessional and tidal signals, the moment of inertia factor and k_2 Love number can be constrained, from which constraints on the density and viscosity profile can be obtained. The magnetic induction response of a planet to time-variable magnetic fields can be used to determine how the body's electrical conductivity (and hence

 http://dx.doi.org/10.1016/B978-0-444-53802-4.00169-X

composition) varies with depth. Finally, because the gravitational field of a planet is sensitive to its internal density structure, another powerful method that can be used to probe the subsurface, and which is the subject of this review, is the joint analysis of gravitational and topographic data.

The past two decades have witnessed dramatic advancements in our understanding and knowledge of the gravitational fields and topography of the terrestrial planets. These advances are intimately related to the acquisition of radio tracking data from orbiting spacecraft, measurements of the range and range rate between co-orbiting satellites, measurements of gravitational gradients from orbit, the collection of data from orbiting altimeters, and the construction of terrain models from stereo imagery. As examples, from data collected by NASA's Lunar Reconnaissance Orbiter (LRO; Vondrak et al., 2010) and Gravity Recovery and Interior Laboratory (GRAIL) (Zuber et al., 2013a) missions, respectively, launched in 2009 and 2011, the gravity and topography of the Moon are now known better globally than any other planetary object, including Earth. The topography of Venus was mapped by the technique of radar altimetry during the Magellan mission (placed in orbit in 1990; Saunders et al., 1990), and radio tracking data acquired during this mission has led to the construction of a global gravity model. From the laser altimeter onboard the Mars Global Surveyor (MGS) mission (placed in orbit in 1997; Smith et al., 2001a), the topography of Mars has been mapped to high resolution, and radio tracking of this and subsequent spacecraft has allowed for continued improvement to the Martian gravity field. In a similar manner, radio tracking and laser altimetry are being used by the MESSENGER spacecraft that is currently in orbit about Mercury (Solomon et al., 2001). Finally, the topography and gravitational field of Earth are continually being refined, most notably by a series of recent and ongoing missions such as GRACE (Gravity Recovery and Climate Experiment; Tapley et al., 2005) and GOCE (Gravity Field and Steady-State Ocean Circulation Explorer; Drinkwater et al., 2003).

From a geophysical and comparative planetology perspective, the motivation for obtaining high-resolution gravitational and topographic data is to place constraints on the formation, interior structure, and geologic evolution of a planet. The magnitude and direction of the gravitational acceleration exterior to a planet are completely determined by its internal distribution of mass, a result of Newton's law of gravitation. When combined with topographic data and reasonable geologic assumptions, it becomes possible to invert for important geophysical parameters, such as crustal thickness, elastic thickness, and crustal and mantle densities. These model parameters can then be used to address questions concerning planetary differentiation, crust formation, thermal evolution, and magmatic processes. Since the spatial resolving power of gravitational measurements decreases with increasing distance from the object, these investigations are generally restricted to the crust and upper mantle.

Very few research articles have been written that review the gravitational fields and topography of the terrestrial planets from a comparative planetology perspective: useful summaries can be found in Phillips and Lambeck (1980), Balmino (1993), Bills and Lemoine (1995), and Rummel (2005). The purpose of this chapter is both to review the current state of knowledge of the gravitational fields and topography of the terrestrial planets and to review the tools that are used to describe and analyze these data. While gravitational and topographic datasets can each be used independently to make inferences about the interior structure of a planet, such results are often based upon hypotheses that are not easily testable or models that are highly underconstrained. Thus, although regional topographic models have been constructed for some moons and asteroids (such as Phobos (Wählisch et al., 2010), 433 Eros (Gaskell et al., 2008; Zuber et al., 2000a), Itokawa (Abe et al., 2006; Gaskell et al., 2008), Vesta (Jaumann et al., 2012), Ganymede (Giese et al., 1998), Europa (Nimmo et al., 2003a,b; Nimmo et al., 2007), Iapetus (Giese et al., 2008), Mimas (Dermott and Thomas, 1988), Enceladus (Thomas et al., 2007), Tethys (Thomas et al., 2007), Dione (Thomas et al., 2007), Rhea (Thomas et al., 2007), and many of the irregularly shaped satellites of Saturn (Thomas, 2010)) and the longest wavelength gravitational fields and topography have been constrained for others (such as Io (Anderson et al., 2001a; Thomas et al., 1998), Europa (Anderson et al., 1998), Ganymede (Anderson et al., 1996b; Palguta et al., 2006), Callisto (Anderson et al., 2001b), Rhea (Anderson and Schubert, 2010), Titan (Iess et al., 2010; Lorenz et al., 2013), and Vesta (Konopliv et al., 2013a)), this chapter will focus on those planetary bodies for which the gravity and topography are both characterized to high resolution, namely, Earth, Venus, Mars, Mercury, and the Moon.

The outline of this chapter is as follows. First, in **Section 10.05.2**, a general review of the mathematical formalism that is used in describing the properties of gravitational fields and topography is given. In **Section 10.05.3**, the basic properties of the gravitational fields and topography of Earth, Venus, Mars, Mercury, and the Moon are characterized. Following this, **Sections 10.05.4–10.05.7** discuss the relationship between gravity and topography and how the two datasets can be used to invert for geophysical parameters. These methods include crustal thickness modeling, the analysis of geoid/topography ratios (GTRs), modeling of the spectral admittance and correlation functions, and localized spectral analysis and wavelet techniques. **Section 10.05.8** summarizes the major results that have been obtained for these planetary bodies, and **Section 10.05.9** concludes by discussing future developments that can be expected in this domain.

10.05.2 Mathematical Preliminaries

This section reviews the mathematical background that is required to understand how gravitational fields and topography are characterized and manipulated. As most analysis techniques make use of spherical harmonics, the first subsection defines these functions and introduces certain concepts such as the power spectrum. The following subsection gives definitions that are specific to the gravitational potential, gravitational field, and geoid. For further details, the reader is referred to several key books and articles such as **Chapter 3.02**, Jeffreys (1976), Kaula (1967), Kaula (2000), Heiskanen and Moritz (1967), Lambeck (1988), and Hofmann-Wellenhof and Moritz (2006).

10.05.2.1 Spherical Harmonics

Spherical harmonics are the natural set of orthogonal basis functions on the surface of the sphere. As such, any real square-integrable function can be expressed as a linear combination of these as

$$f(\theta, \phi) = \sum_{l=0}^{\infty} \sum_{m=-l}^{l} f_{lm} Y_{lm}(\theta, \phi) \quad [1]$$

where Y_{lm} is the spherical harmonic function of degree l and order m, f_{lm} is the corresponding expansion coefficient, and θ and ϕ represent the position on the sphere in terms of planetocentric colatitude and longitude, respectively. Alternative representations include the use of ellipsoidal harmonics (e.g., Garmier and Barriot, 2001; Jekeli, 1988) when the function is known globally and Slepian functions (Simons et al., 2006) or spherical cap harmonics (e.g., Haines, 1985; Hwang and Chen, 1997; Thébault et al., 2006, 2004) when the function is known only regionally. This chapter will use exclusively planetocentric coordinates, where colatitude is measured with respect to the polar axis, but the reader should be aware that many datasets for Earth make use of planetographic coordinates. Planetographic latitude differs from planetocentric latitude in that it is defined as the angle between the normal to an ellipsoid and the equatorial plane.

In geodesic and gravitational applications, the real spherical harmonics are defined as

$$Y_{lm}(\theta, \phi) = \begin{cases} \overline{P}_{lm}(\cos\theta)\cos m\phi & \text{if } m \geq 0 \\ \overline{P}_{l|m|}(\cos\theta)\sin|m|\phi & \text{if } m < 0 \end{cases} \quad [2]$$

where the normalized associated Legendre functions are given by

$$\overline{P}_{lm}(\mu) = \sqrt{(2-\delta_{0m})(2l+1)\frac{(l-m)!}{(l+m)!}} P_{lm}(\mu) \quad [3]$$

and where δ_{ij} is the Kronecker delta function. The unnormalized Legendre functions in the aforementioned equation are defined in relation to the Legendre polynomials by

$$P_{lm}(\mu) = \left(1-\mu^2\right)^{m/2} \frac{\mathrm{d}^m}{\mathrm{d}\mu^m} P_l(\mu) \quad [4]$$

$$P_l(\mu) = \frac{1}{2^l l!} \frac{\mathrm{d}^l}{\mathrm{d}\mu^l} \left(\mu^2 - 1\right)^l \quad [5]$$

The normalized associated Legendre functions are orthogonal for a given value of m according to

$$\int_{-1}^{1} \overline{P}_{lm}(\mu)\overline{P}_{l'm}(\mu)\mathrm{d}\mu = 2(2-\delta_{0m})\delta_{ll'} \quad [6]$$

and the spherical harmonics are orthogonal over both l and m with the normalization

$$\int_{\Omega} Y_{lm}(\theta, \phi) Y_{l'm'}(\theta, \phi)\mathrm{d}\Omega = 4\pi\delta_{ll'}\delta_{mm'} \quad [7]$$

where $\mathrm{d}\Omega = \sin\theta\ \mathrm{d}\theta\ \mathrm{d}\varphi$. Multiplying eqn [1] by $Y_{l'm'}$ and integrating over all space, the spherical harmonic coefficients of the function f can be obtained from the integral

$$f_{lm} = \frac{1}{4\pi} \int_{\Omega} f(\theta, \phi) Y_{lm}(\theta, \phi)\mathrm{d}\Omega \quad [8]$$

A useful visualization property of the spherical harmonic functions is that they possess $2|m|$ zero crossings in the longitudinal direction and $l-|m|$ zero crossings in the latitudinal direction. In addition, for a given spherical harmonic degree l, the equivalent Cartesian wavelength is $\lambda \approx 2\pi R/\sqrt{l(l+1)}$, where R is the mean planetary radius, a result known as the Jeans relation. It should be noted that those coefficients and spherical harmonics where $m=0$ are referred to as zonal, those with $l=|m|$ are sectoral, and the rest are tesseral. Furthermore, the zonal coefficients C_{l0} are often written as $-J_l$.

Using the orthogonality properties of the spherical harmonic functions, it is straightforward to verify that the total power of a function f is related to its spectral coefficients by a generalization of Parseval's theorem:

$$\frac{1}{4\pi} \int_{\Omega} f^2(\theta, \phi)\mathrm{d}\Omega = \sum_{l=0}^{\infty} S_{ff}(l) \quad [9]$$

where

$$S_{ff}(l) = \sum_{m=-l}^{l} f_{lm}^2 \quad [10]$$

is referred to as the power spectrum of the function. (The term 'power' is here used in the sense of the signal processing literature; namely, the square of the function divided by the area that it spans.) It can be shown that S_{ff} is unmodified by a rotation of the coordinate system. Similarly, the cross power of two functions f and g is given by

$$\frac{1}{4\pi} \int_{\Omega} f(\theta, \phi) g(\theta, \phi)\mathrm{d}\Omega = \sum_{l=0}^{\infty} S_{fg}(l) \quad [11]$$

where

$$S_{fg}(l) = \sum_{m=-l}^{l} f_{lm} g_{lm} \quad [12]$$

is defined as the cross power spectrum. If the functions f and g have a zero mean (i.e., their degree-0 terms are equal to zero), then $S_{ff}(l)$ and $S_{fg}(l)$ represent the contributions to the variance and covariance, respectively, for degree l. Some authors plot routinely the power per degree, $S/(2l+1)$, or the root-mean-square (rms) amplitude of the spherical harmonic coefficients, $\sqrt{S/(2l+1)}$.

One source of confusion with spherical harmonic analyses is that not all authors use the same definitions for the spherical harmonic and Legendre functions. In contrast to the 'geodesy' or '4π' normalization of eqn [7] (cf. Kaula, 2000), the seismology (e.g., Dahlen and Tromp, 1998) and physics (e.g., Varshalovich et al., 1988) communities often use orthonormal harmonics, whose squared integral is equal to unity. The geomagnetic community employs Schmidt seminormalized harmonics whose squared integral is $4\pi/(2l+1)$ (e.g., Blakely, 1995). A more subtle problem is related to a phase factor of $(-1)^m$ (the Condon–Shortley phase) that is sometimes applied to either eqn [3] or [4]. Whereas the spherical harmonics used by the geodesy and geomagnetic communities both exclude this phase factor, those in the physics and seismology communities often include it. To convert the spherical harmonic coefficients from one normalization to another (here labeled by

superscripts 1 and 2), it is necessary only to recognize that the product of the spherical harmonic coefficient and function is independent of the normalization:

$$f_{lm}^{(1)}Y_{lm}^{(1)} = f_{lm}^{(2)}Y_{lm}^{(2)} \qquad [13]$$

In order to obtain the spherical harmonic coefficients f_{lm} of a function f, it is necessary to be able to calculate accurately both the normalized Legendre functions of eqn [3] and the integral of eqn [8]. Methods for efficient calculation of the normalized associated Legendre functions depend upon the use of well-known three-term recursion formulas. If starting values used in the recursion are appropriately scaled, as is summarized by Holmes and Featherstone (2002), these can be computed to high accuracy up to a maximum spherical harmonic degree of about 2700. To obtain a similar accuracy at higher degrees would require the use of an alternative scaling algorithm (e.g., Fukushima, 2011; Jekeli et al., 2007).

The integrals of eqn [8] are most easily performed if the function f is known on a set of evenly spaced grid points in longitude. Numerical methods for calculating this integral involve Fourier transforming each latitudinal band and then integrating over latitude for each l and m (e.g., Sneeuw, 1994). If the function is sampled on an $n \times n$ grid, with n even, and if the function is known to be bandlimited to a maximum degree $n/2-1$, then the spherical harmonic transform can be computed exactly (see Driscoll and Healy, 1994). Alternatively, the integral over latitude can be performed using Gauss–Legendre quadrature (e.g., Press et al., 1992, pp. 140–149). While the integrand of eqn [8] is not in general a terminating polynomial, if the function is bandlimited to a maximum degree n, $n+1$ points in latitude are sufficient to calculate accurately the spherical harmonic expansion coefficients. Publicly available software packages, such as SHTOOLS developed by the author, are readily available for performing the calculations in this manuscript (see **Table 1** for a list of Internet resources).

10.05.2.2 Gravity, Potential, and Geoid

The gravitational acceleration $\mathbf{g}$ at position $\mathbf{r}$ that results from a mass dm at position $\mathbf{r}'$ is given by Newton's law of gravitation:

$$\mathbf{g}(\mathbf{r}) = -G\mathrm{d}m\frac{\mathbf{r}-\mathbf{r}'}{|\mathbf{r}-\mathbf{r}'|^3} \qquad [14]$$

Given that the curl of $\mathbf{g}$ is zero, this vector force field is conservative, and the gravitational acceleration can be expressed as the gradient of a scalar potential U:

$$\mathbf{g}(\mathbf{r}) = \nabla U(\mathbf{r}) \qquad [15]$$

where the gradient operator in spherical coordinates is

$$\nabla = \hat{r}\frac{\partial}{\partial r} + \hat{\theta}\frac{1}{r}\frac{\partial}{\partial \theta} + \hat{\phi}\frac{1}{r\sin\theta}\frac{\partial}{\partial \phi} \qquad [16]$$

The gravitational potential can be calculated at an arbitrary point by a simple integral over the mass distribution

$$U(\mathbf{r}) = \int_V \frac{G\rho(\mathbf{r}')}{|\mathbf{r}-\mathbf{r}'|}\mathrm{d}V' \qquad [17]$$

where ρ is the mass density and V signifies that space occupied by the body. Whereas the sign convention of eqns [15] and [17] are consistent with that used in the geodesy literature, it should be noted that other disciplines, such as physics, place a negative sign in front of each of these equations.

Exterior to the mass distribution V, it can be shown that the potential satisfies Laplace's equation (e.g., Kaula, 2000, chap. 1):

$$\nabla^2 U(\mathbf{r}) = 0 \qquad [18]$$

By using this relationship and the method of separation of variables, the potential U exterior to V can be expressed alternatively as a sum of spherical harmonic functions:

$$U(\mathbf{r}) = \frac{GM}{r}\sum_{l=0}^{\infty}\sum_{m=-l}^{l}\left(\frac{R_0}{r}\right)^l C_{lm}Y_{lm}(\theta,\phi) \qquad [19]$$

Here, the C_{lm}s represent the spherical harmonic coefficients of the gravitational potential at a reference radius R_0, G is the gravitational constant, and M is the total mass of the object. In practice, the infinite sum is truncated beyond a maximum degree L that is justified by the data resolution. The coefficients C_{lm} of eqn [19] are related uniquely to the internal mass distribution of the body, and methods for calculating these

Table 1 Internet resources

Resource	*Internet address*
SHTOOLS: Fortran 95 spherical harmonics software archive	http://shtools.ipgp.fr/
ETOPO1: Earth 1 arc minute topography model	http://www.ngdc.noaa.gov/mgg/global/global.html
GTOPO30: Earth 30 arc second topography model	https://lta.cr.usgs.gov/GTOPO30
GLOBE: Earth 30 arc second global topography	http://www.ngdc.noaa.gov/mgg/topo/globe.html
SRTM: Earth topography model	http://dds.cr.usgs.gov/srtm/
STRM30_PLUS: Earth 30 arc second topography and bathymetry model	http://topex.ucsd.edu/WWW_html/srtm30_plus.html
Earth2012: Spherical harmonic models of the Earth's topography and potential	http://geodesy.curtin.edu.au/research/models/Earth2012/
WGS84 ellipsoid and 'WGS84 EGM96 geoid'	http://earth-info.nga.mil/GandG/wgs84/
ICGEM: International Center for Global Earth Models (collection of gravity models)	http://icgem.gfz-potsdam.de/ICGEM/ICGEM.html
Planetary Data System (PDS) Geosciences node	http://geo.pds.nasa.gov/
Spherical harmonic models of planetary topography	http://www.ipgp.fr/~wieczor/SH/SH.html
GTDR3.2: Venusian topography	ftp://voir.mit.edu/pub/mg3003/
Generic Mapping Tools	http://gmt.soest.hawaii.edu/

are deferred until Section 10.05.4. Here, it is only noted that the degree-0 coefficient C_{00} is equal to unity and that if the coordinate system has been chosen such that it coincides with the center of mass of the object, the degree-1 terms (C_{10}, C_{11}, and $C_{1,-1}$) are identically zero. The negative order coefficients $C_{l,-m}$ are often referred to as S_{lm}.

As a result of the factor $(R_0/r)^l$ that multiplies each term in eqn [19], the high-frequency components in this sum (i.e., those with large l) will be attenuated when the observation radius r is greater than the reference radius R_0. In contrast, if the coefficients were determined at the altitude of an orbiting satellite, and if this equation were used to determine the potential field on the surface of the planet, then the high-frequency terms would instead be relatively amplified. Since the spherical harmonic coefficients always possess some uncertainty, which generally increases with increasing l, the process of downward continuing a potential field is not stable and must generally be compensated by some form of filtering (e.g., Fedi and Florio, 2002; Phipps Morgan and Blackman, 1993; Wieczorek and Phillips, 1998).

If the body under consideration is rotating, an additional nongravitational force must be taken into account when one is on the surface. In the reference frame of the rotating body, this can be accounted for by adding to eqn [19] a pseudopotential term that is a result of the centrifugal force. This rotational potential, as well as its spherical harmonic expansion, is given by

$$U^{\text{rot}} = \frac{\omega^2 r^2 \sin^2\theta}{2} = \omega^2 r^2 \left(\frac{1}{3} Y_{00} - \frac{1}{3\sqrt{5}} Y_{20} \right) \qquad [20]$$

where ω is the angular velocity of the rotating object. For some applications, especially concerning Earth and Moon, it is necessary to include the tidal potential of the satellite or parent body when calculating the potential (see Dermott, 1979; Zharkov et al., 1985). For a synchronously locked satellite on a circular orbit, the combined tidal and rotational potential in the rotating frame is given approximately by

$$U^{\text{tide+rot}} \simeq \omega^2 r^2 \left(\frac{1}{3} Y_{00} - \frac{5}{6\sqrt{5}} Y_{20} + \frac{1}{4} \sqrt{\frac{12}{5}} Y_{22} \right) \qquad [21]$$

For eccentric and inclined orbits, the reader is referred to Murray and Dermott (2008).

An important quantity in both geodesy and geophysics is the geoid, which is defined to be a surface that possesses a specific value of the potential. (Although one could come up with imaginative names for equipotential surfaces on Mercury, Venus, Eros, Io, and Titan, among others, the term geoid will here be used for all.) As there are no tangential forces on an equipotential surface (see eqn [15]), a static fluid would naturally conform to the geoid. The oceans of Earth are approximately static and are well approximated by such a surface. In geophysics, stresses within the lithosphere are often calculated by referencing the vertical position of a density contrast to an equipotential surface. This is necessary when performing lithospheric flexure calculations, especially when considering the longest wavelengths.

The height N of an equipotential surface above a spherical reference radius R can be obtained by approximating the potential by a Taylor series

$$U(R+N) \simeq U(R) + \frac{\mathrm{d}U(R)}{\mathrm{d}r} N + \frac{1}{2} \frac{\mathrm{d}^2 U(R)}{\mathrm{d}^2 r} N^2 \qquad [22]$$

and setting this expression equal to a constant

$$U(R+N) = \frac{GM}{R} + \frac{\omega^2 R^2}{3} \qquad [23]$$

the value of which is here chosen to be the degree-0 term of the potential at the reference radius R for a rotating planet. Since this equation is quadratic in N, the geoid height can be solved for analytically at any given position. Analytic expressions for the partial derivatives of the potential are obtained easily in the spectral domain from eqns [19] and [20] (see also eqn [25]). It is noted that an analytic expression for the geoid using a third-order expansion of eqn [22] also exists.

For some cases, it is sufficient to use only the first-order term of eqn [22]. If the first derivative of U is approximated by $-GM/R^2$, then the geoid is simply given by

$$N \simeq R \sum_{l=2}^{\infty} \sum_{m=-l}^{l} \left(\frac{R_0}{R} \right)^l C_{lm} Y_{lm} - \frac{\omega^2 R^4}{3\sqrt{5} GM} Y_{20} \qquad [24]$$

where the degree-1 terms have been assumed to be zero. Although the maximum difference between the first- and second-order methods is less than half a meter for the Moon, Mercury, and Venus, differences of up to 26 and 42 m are obtained for Earth and Mars, respectively. The poor performance of the first-order approximation for Earth and Mars is a result of the large rotationally induced flattening of these two planets.

Despite the simplicity of the aforementioned method for obtaining the height to an equipotential surface, the question arises as to *which* equipotential surface should be used. For Earth, a natural choice is the potential corresponding to mean sea level. However, for the other planets, the choice is more arbitrary (but often not important). As the aforementioned equations for calculating the potential are strictly valid only when the observation point is exterior to the body, one manner of picking a specific potential might be to choose that value for which all points on the geoid are exterior to the body. (Calculation of the potential below the surface of a planet would require knowledge of the interior density distribution.) Another approach that could be used would be to use the mean potential on the planet's equator. Alternatively, the geoid could be chosen such that it best fits, in a least squares sense, the observed shape of the planet (Ardalan et al., 2010).

The radial component of the gravitational field is calculated by taking the first radial derivative of eqn [19]. Ignoring the rotational potential, and using the sign convention that gravitational accelerations are positive when directed downward, this is given by the expression

$$g_r = \frac{GM}{r^2} \sum_{l=0}^{\infty} \sum_{m=-l}^{l} \left(\frac{R_0}{r} \right)^l (l+1) C_{lm} Y_{lm} \qquad [25]$$

Note that this equation differs from the potential only by the inclusion of the additional factors $1/r$ and $(l+1)$. The second factor gives a greater importance to the higher-degree terms, and it is for this reason that plots of the potential and geoid appear to be smooth when compared to components of the gravitational field. In terrestrial applications, it is common to calculate the gravitational field on the geoid. By inserting

eqn [24] into eqn [25] and ignoring rotational and higher-order terms, it can be shown that the radial component of the gravitational field on the geoid can be approximated simply by replacing the term $(l+1)$ in eqn [25] by $(l-1)$. If it is necessary to calculate the gravity field on an irregular surface, this can be accomplished by using a Taylor series that makes use of the known field and higher-order derivatives on a spherical interface (Hirt, 2012). The standard unit for quantifying gravitational perturbations is the galileo, where $1\ \text{Gal} = 10^{-2}\ \text{m s}^{-2}$, and when plotting gravitational anomalies in map form, it is conventional to use milligals.

Finally, it will be useful to characterize the relationship between the gravitational field and topography in the spectral domain. For this, let us presume that the radial gravity g_{lm} and topography h_{lm} are related by

$$g_{lm} = Q_{lm} h_{lm} + I_{lm} \quad [26]$$

where Q_{lm} is a linear nonisotropic transfer function and I_{lm} is that portion of the gravitational signal, such as noise, that is not predicted by the model (the topography can often be considered noise-free). If I_{lm} is uncorrelated with the topography, then it is straightforward to show that the expectation of S_{gh} will be unaffected by this signal. (This can be shown by multiplying eqn [26] by h_{lm}, summing over all m, and taking the expectation.) In contrast, the expectation of the gravitational power spectrum will depend upon the magnitude of I_{lm}. In particular, for the case where I_{lm} is a random variable that is independent of the surface topography, the expectation of the observed gravitational power spectrum is simply

$$S_{gg}^{\text{obs}}(l) = S_{gg}(l) + S_{II}(l) \quad [27]$$

where S_{gg} is the power spectrum predicted exclusively by the model Q_{lm} and S_{II} is the expectation of the power spectrum of I_{lm}. Thus, gravitational measurement noise will bias the gravitational power spectrum by an additive constant.

In quantifying the relationship between gravity and topography, it is useful to work with ratios of their cross power spectra. One quantity, referred to as the *admittance*, is defined by the cross power of the two functions divided by the power of the topography (e.g., Dorman and Lewis, 1970):

$$Z(l) = \frac{S_{hg}(l)}{S_{hh}(l)} \quad [28]$$

This function is not biased by the presence of noise, and when the transfer function Q_{lm} is isotropic (i.e., independent of m), it is an unbiased estimate of Q_l. Another ratio that is commonly used and that is dimensionless is the *correlation*:

$$\gamma(l) = \frac{S_{hg}(l)}{\sqrt{S_{hh}(l) S_{gg}(l)}} \quad [29]$$

If the coefficients h_{lm} and g_{lm} possess a zero mean, the aforementioned function is simply the correlation coefficient of the two sets of harmonic coefficients for a given degree l, which is bounded between 1 and -1. Whereas noise will not bias the admittance function, it will bias the degree correlation function toward lower values as a consequence of the gravitational power spectrum in the denominator of this expression. The term *coherence* is usually reserved for the correlation squared, but this definition is not universally followed. Since squaring the correlation discards information (its sign), its use is not advocated here. It is noted that the isotropic version of eqn [26] predicts that the spectral correlation coefficient should always be ± 1. Nevertheless, as discussed in Section 10.05.7, nonisotropic models yield expressions that are degree-dependent. Whereas other ratios of cross power spectra could be constructed, only two will be independent. Since the relationship between gravity and topography is nonlinear (see eqn [33]), in the following section, it will be useful to plot the correlation between the observed gravity and the gravity predicted from surface topography.

10.05.3 The Data

10.05.3.1 Earth

10.05.3.1.1 Topography

Despite the fact that the measurement of the Earth's topography and bathymetry has been the subject of numerous government-supported campaigns, large portions of the Earth's surface, namely, the oceans, remain poorly characterized. Indeed, from a global perspective, it can be said that the shapes of Mars and the Moon are known better than that of the planet we call home. Until recently, even the elevations of the aerial portions of the continents possessed long-wavelength uncertainties, a result of mosaicking numerous elevation models, each with its own reference surface, along artificial political boundaries. While major advances have been made in the past decade toward generating global models, the main deficiency is still the sparse bathymetry of the oceans.

Numerous topographic models of the Earth's landmass have been assembled from various sources over the past few decades, including ETOPO1 (1 arc minute resolution; Amante and Eakins, 2009), GLOBE (30 arc second resolution; Hastings and Dunbar, 1999), and GTOPO30 (detailed documentation for these and all following topography models can be found at the appropriate web addresses listed in Table 1). Currently, the most accurate model of the Earth's landmass comes from radar interferometric data collected by the Shuttle Radar Topography Mission (SRTM). During its 10 days of operation onboard the US space shuttle in year 2000, this mission mapped nearly 80% of the landmass between 60°N and 54°S with a horizontal sampling of 1 arc second (~30 m) and an absolute vertical accuracy better than about 10 m (Rabus et al., 2003; Rodríguez et al., 2005). Because of the 5.6 cm wavelength of the radar, elevations correspond to the top of the canopy when vegetation is present.

The bathymetry of the oceans has been measured from ship surveys using echo sounding for over half a century. Unfortunately, the ship tracks sometimes possess large navigational errors, and large data gaps exist. As reviewed by Marks and Smith (2006), many datasets exist that are based upon these measurements, but each has its own peculiarities. In the absence of additional ship survey data, one method that can be used to improve the bathymetry of the oceans is by combining ship survey data with marine gravity data. As is detailed by Smith and Sandwell (1994, 1997), marine gravitational anomalies (as obtained from altimeter-derived sea surface slopes) are highly correlated with seafloor topography over a restricted wavelength band. By combining predicted topography from

bandpassed gravitational anomalies with the long-wavelength bathymetry from shipboard sounding, it has been possible to obtain near-global 2 arc second resolution estimates of seafloor topography. Nevertheless, it should be emphasized that such data products are indeed estimates and that they may be inappropriate for certain types of geophysical modeling.

Global Earth's topography models that combine oceanic bathymetry and landmass topography include ETOPO1 and SRTM30_PLUS. The latter of these represents a combination of the SRTM 30 arc second data and the Smith and Sandwell (1997)-predicted bathymetry, with gaps filled by GTOPO30 data, among others. Using the SRTM, SRTM30_PLUS, and ETOPO1 datasets, a suite of high-degree spherical harmonic models has been constructed by Hirt et al. (2012) (Earth2012) that include models of planetary shape, relief with respect to the geoid, and rock-equivalent topography. An image of this global topographic model is displayed in **Figure 1**, where the elevations are plotted with respect to the EGM96 geoid, which is a good approximation of mean sea level (see Internet documentation in **Table 1** for precise definitions). To obtain absolute radii of Earth (as is necessary for most methods that calculate gravity from topography), it is necessary to add the elevation of the geoid, which is referenced to the WGS84 ellipsoid, and the shape of the WGS84 ellipsoid itself. The WGS84 ellipsoid is a good representation of the Earth's zonal shape and possesses a 21 km rotationally induced difference in elevation between the equator and polar axis. A summary of fundamental planetary constants is given in **Table 2**.

10.05.3.1.2 Gravity

The gravitational field of Earth has been mapped by several techniques, including analyses of satellite radio tracking data, ranging between co-orbiting spacecraft, measurement of gravitational gradients from orbit, and terrestrial measurement campaigns. Satellite altimetry of the ocean surface provides additional constraints, as geoid slopes are proportional to the gravity field in the spectral domain (see, among others, Hwang and Parsons, 1996; Sandwell and Smith, 1997). The construction of global high-resolution models consists of combining the long-wavelength information from satellite tracking data with the short-wavelength information in the terrestrial and oceanic altimeter surveys. The model EGM96 (Lemoine et al., 1998) has been the standard reference for much of the past decade, and this was recently superseded by the model EGM2008 (Pavlis et al., 2012). EGM2008 is complete to degree and order 2160 and makes use of a global 180 degree and order GRACE-based solution, gravitational anomalies over the ocean derived from satellite altimetry, and terrestrial and airborne gravity data. The EIGEN-6c2 gravity model (Förste et al., 2012), developed to degree and order 1949, is largely consistent with EGM2008 and makes use of GRACE intersatellite ranges, GOCE gravity gradients, LAGEOS satellite laser ranging data, ocean geoid, and terrestrial data.

The analysis of data from the ongoing missions (Challenging Mini-Satellite Payload (CHAMP); launched in 2000; Reigber et al., 2004), GRACE (launched in 2002; Tapley et al., 2004), and GOCE (launched in 2009; Floberghagen et al., 2011; Rummel et al., 2011) is providing highly accurate estimates of the Earth's long-wavelength gravity field (corresponding to spherical harmonic degrees less than about 200; Pail et al., 2011) and time variations in gravity resulting from geologic processes. These satellites all utilize continuous satellite to GPS (global positioning system) tracking data for orbit determination. CHAMP and GOCE are single satellites, but the primary payload of GOCE is a three-axis gravity gradiometer. GRACE consists of two satellites on identical orbits, of which the distance between the two is measured to high accuracy by a microwave communication link. The analyses of data from GRACE have been providing monthly global gravity solutions since 2003, allowing for study of hydrogeologic, postseismic deformation, and postglacial rebound phenomena.

The images of the total gravitational and geoid anomalies, as determined from eqn [25] and the second-order approximation of eqns [22] and [24], are shown in **Figure 1** for the model EMG2008. The total gravitational anomaly is here defined as the total gravitational acceleration on the rotating WGS84 ellipsoid after removal of the predicted 'normal gravity' of a homogeneous ellipsoid (e.g., Hofmann-Wellenhof and Moritz, 2006). Though this terminology is in common usage in the geophysics community, geodesists would call this the total gravity disturbance. (In terrestrial geodesy, the gravitational anomaly is defined as the gravity on the geoid minus the normal gravity on the reference ellipsoid, where the two quantities are calculated at different points in space.) The largest gravitational anomalies are seen to be correlated with topography (such as trenches and seamounts), and the geoid height is found to vary by about 200 m.

10.05.3.1.3 Spectral analysis

Spectral and cross-spectral properties of the shape model Earth2012 RET and the EGM2008 potential are plotted in **Figure 2**. For this shape model, the radius of the ocean floor was increased by 1030/2670 times its depth in order to convert the mass of the overlying sea water into 'rock-equivalent topography.' As demonstrated in the left panel, the power spectrum of the geoid is about five orders of magnitude less than that of the topography, which is a reflection of the low amplitudes of the geoid undulations present in **Figure 1**. The error spectrum of the potential model demonstrates that the coefficients are well determined at low degrees, with relative uncertainties gradually increasing to 100% near degree 1800. As a result of the ~260 km altitude of GOCE and the ~400–500 km altitudes of GRACE and CHAMP, the contribution to the gravitational field from these spacecraft is necessarily limited to degrees less than about 250; the higher-degree terms are constrained almost entirely by surface measurements.

The admittance and correlation spectra between the radial gravity and topography are plotted in the right panel of **Figure 2**. Given that the relationship between gravity and topography is nonlinear, especially at high degrees, the correlation spectrum is here calculated using the spherical harmonic coefficients of the free-air gravity and the gravity predicted from topography. The correlation for many of the lowest degrees is seen to be small and in some cases negative. The correlation increases beyond degree 12 from about 0.7 to attain a nearly constant value close to 0.9 near degree 500. The slight decrease in correlation that is observed beyond degree 1800 is likely a result of the sparse gravity coverage over portions of the oceanic and continental crust. If the correlation were calculated using the observed topography,

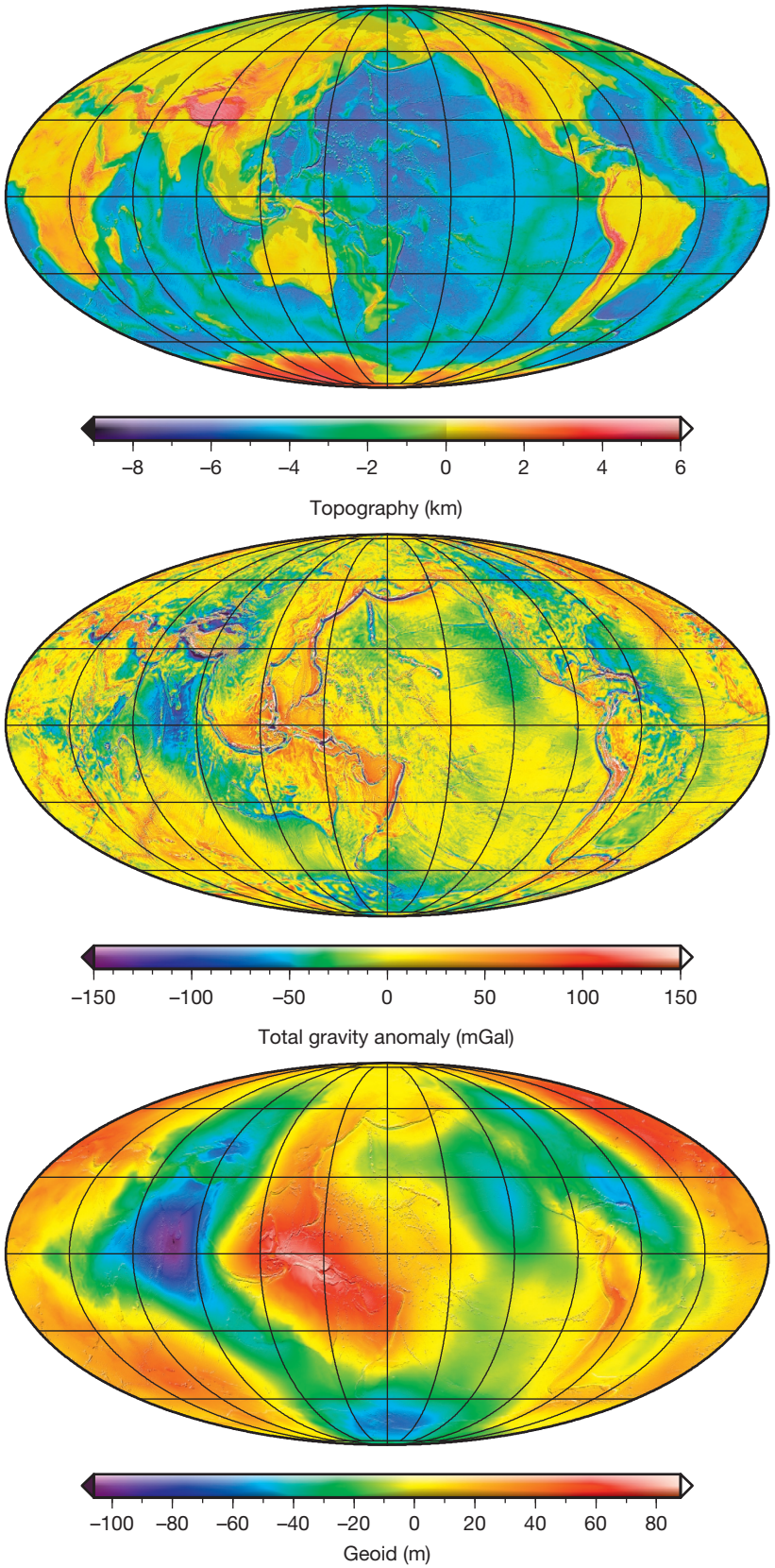

Figure 1 (Top) Global topography and bathymetry of Earth (model Earth2012), referenced to the WGS84 EGM96 geoid, (middle) the EGM2008 total gravitational anomaly on the WGS84 ellipsoid, and (bottom) the height of the EGM2008 geoid above the WGS84 ellipsoid. All images are in a Mollweide projection with a central meridian of 180°W longitude and are overlain by a gradient image derived from the topographic model.

Table 2 Gravitational and shape constants

Parameter	*Value*	*Source*
G	$6.67384(80) \times 10^{-11}$ m^3 kg^{-1} s^{-2}	Committee on Data for Science and Technology; Mohr et al. (2012)
Earth		
GM	$398.6004415 \times 10^{12}$ m^3 s^{-2}	EGM2008; Pavlis et al. (2012)
Semimajor axis	6378.137 km	WGS84; National Imagery and Mapping Agency (2000)
Semiminor axis	6356.7523142 km	WGS84; National Imagery and Mapping Agency (2000)
Radius of sphere of equal volume	6371.00079 km	WGS84; National Imagery and Mapping Agency (2000)
ω	72.921150×10^{-6} rad s^{-1}	WGS84; National Imagery and Mapping Agency (2000)
Venus		
GM	$324.858592 \times 10^{12}$ m^3 s^{-2}	MGNP180U; Konopliv et al. (1999)
Mean planetary radius	6051.878 km	VenusTopo719; this chapter
ω	-299.24×10^{-9} rad s^{-1}	Konopliv et al. (1999)
Mars		
GM	$42.8283748313 \times 10^{12}$ m^3 s^{-2}	JGMRO_110c; Konopliv et al. (2011)
Mean planetary radius	3389.500 km	MarsTopo2600; this chapter
ω	$70.8821807 \times 10^{-6}$ rad s^{-1}	Jacobson (2010)
Mercury		
GM	$22.031839224 \times 10^{12}$ m^3 s^{-2}	GGMES_20v04; Smith et al. (2012)
Mean planetary radius	2439.372 km	GTMES_24v01
ω	$1.2400172589 \times 10^{-6}$ rad s^{-1}	Rambaux and Bois (2004)
The Moon		
GM	$4.90280007 \times 10^{12}$ m^3 s^{-2}	DE430; Williams et al. (2014)
Mean planetary radius	1737.151 km	LOLA2600p; this chapter
ω	2.6617073×10^{-6} rad s^{-1}	Yoder (1995)

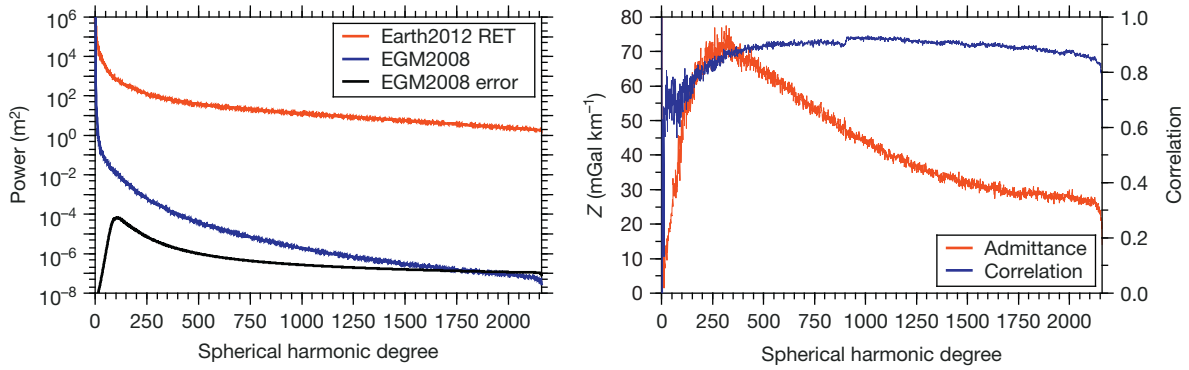

Figure 2 Power and cross power spectra of the Earth's radial gravity and topography. (Left) Power spectra of the topography (Earth2012 RET), geoid (EGM2008), and geoid error. (Right) Admittance and correlation spectra of the radial gravity and topography. The correlation spectrum is calculated using the spherical harmonic coefficients of the observed free-air gravity and gravity predicted from topography.

instead of gravity predicted from topography, the correlation would decrease to less than 0.5 at the highest degrees.

If the surface topography were completely uncompensated, which should be a good approximation beyond degree 300, the admittance would have a near-constant value of $2\pi\rho G$, or 42 mGal km^{-1} times the surface density in units of g cm^{-3}. The observed function is everywhere lower than this theoretical value by about a factor of 2. The low admittances at high degrees are a consequence of the fact that the gravity and surface topography are not perfectly correlated on a global scale as a result of subsurface loads (see discussion in **Section 10.05.6.2**).

10.05.3.2 Venus

10.05.3.2.1 Topography

The planet Venus possesses a dense atmosphere and is perpetually enshrouded by opaque clouds of sulfuric acid. In order to obtain measurements of the surface, it is necessary to make use of electromagnetic frequencies, such as microwaves, where the atmosphere is transparent. Surface elevations of Venus have been measured from orbit using radar altimeters onboard the missions Pioneer Venus Orbiter, Venera 15 and 16, and Magellan. Of these, the Magellan spacecraft, which was in orbit between 1990 and 1994, collected the highest resolution measurements on a near-global scale (for a detailed description, see Ford and Pettengill, 1992).

As a result of the elliptical orbit of the Magellan spacecraft, the spatial resolution of the elevation measurements varied between 8×10 km at periapse and 19×30 km at the north pole (Rappaport et al., 1999). Over 4 million range measurements were ultimately collected, and these were used to construct a 5×5 km gridded elevation model. With the exception of a few relatively minor data gaps covering about 2.6% of the planet's surface area, coverage of the planet is fairly uniform.

(If data from previous missions are used to fill the gaps, then just less than 1% of the planet is not covered at this resolution.) Though the spacecraft-surface range measurements are estimated to have an accuracy of less than 10 m (errors can be larger over rough and steeply sloping terrain), uncertainties in the spacecraft orbit at the time of initial processing were sometimes much greater, especially during superior conjunction. The most recent gravity model of Konopliv et al. (1999) has improved considerably the spacecraft navigational errors, and these improved orbit predictions have been used by Rappaport et al. (1999) in a complete reprocessing of the altimetry dataset (archived as GTDR3.2). Horizontal uncertainties in the footprint locations are insignificant in comparison with the footprint size, and the rms radial uncertainty is estimated to be less than 20 m.

An image of the Venusian topography (derived from the spherical harmonic model VenusTopo719; **Section 10.05.3.2.3**) is shown in **Figure 3**, where it is referenced to the geoid. Whereas the hypsometry of Venus is unimodal (e.g., Ford and Pettengill, 1992; Rosenblatt et al., 1994), in contrast to that of Earth that is bimodal, Venus can be broadly characterized by its low-lying plains, 'continental' plateaus, and volcanic swells. The most prominent highlands include Aphrodite Terra, which lies along the equator, and Ishtar Terra, which is located at high northern latitudes. Ishtar Terra and Aphrodite Terra differ in that the former is flanked by high-elevation mountain ranges. Isolated domical volcanic provinces that possess prominent rift valleys include Atla (0°N, 200°E) and Beta (25°N, 280°E) Regiones. The highest topographic excursion corresponds to Maxwell Montes, located in Ishtar Terra, which reaches more than 10 km above the surrounding plains.

10.05.3.2.2 Gravity

Models of the gravitational field of Venus have been constructed through the analyses of tracking data from the Pioneer Venus Orbiter and Magellan spacecraft (for a review, see Sjogren et al., 1997). The orbit of the Pioneer Venus spacecraft was highly eccentric and possessed periapse altitudes as low as 150 km near the equator. The Magellan spacecraft was initially on an eccentric orbit as well, but through the technique of aerobraking during the gravity mapping phase of the mission, the orbit was transformed to a more circular one, with periapse and apoapse altitudes varying between 155–220 and 350–600 km, respectively.

The most recent model of the Venusian gravitational field is the 180 degree and order JPL (Jet Propulsion Laboratory) model MGNP180U of Konopliv et al. (1999). Because of computational constraints at the time, this model was constructed in three phases. In the first step, a model to spherical harmonic degree 120 was generated using the full unconstrained covariance matrix and a spatial a priori constraint that depended on the strength of the gravitational accelerations (such models are labeled SAAP for Surface Acceleration A Priori). The second step used this model as the nominal solution and then solved for the coefficients from degrees 116 to 155 using the same spatial constraint. For the third step, the coefficients were determined from degrees 154 to 180, but instead of using a spatial constraint, the spherical harmonic coefficients were biased toward a global power law (i.e., a 'Kaula rule'). Future models could be improved by performing the inversion in a single step. As a result of the spatial constraint that was employed in the first two steps, the spatial resolution of the model varies dramatically with position on the surface. Spectral resolutions approaching spherical harmonic degree 180 may be realized close to the equator, but other regions possess resolutions as low as degree 40 (see **Figure 3** of Konopliv et al., 1999).

Images of the MGNP180U radial gravitational field and geoid are presented in **Figure 3**, evaluated at a radius of 6051 km, where the spectral coefficients have been truncated beyond degree 65. As a result of the slow retrograde rotation of Venus, there is no appreciable rotational flattening of the planet. These plots show that most gravitational and geoid anomalies are highly correlated with the surface topography. The largest radial gravitational anomalies are associated with the volcanoes Maat and Ossa Mons in Atla Regio, with values reaching about 270 mGal. The high elevations of Maxwell Montes, Beta Regio, and numerous smaller volcanic provinces are also seen to possess significant anomalies. Uncertainties in the radial component of the gravitational field are typically 10 mGal at the surface but can be as high as 50 mGal in places.

Like Earth, the geoid undulations of Venus possess a dynamic range of only ~200 m. The largest geoid anomalies correspond to the volcanic swells of Atla and Beta Regiones and the continental regions of Aphrodite Terra and Ishtar Terra. It is also seen that the plains with the lowest elevations possess negative geoid anomalies. Uncertainties in the geoid are typically 1 m but can reach values as high as 4 m.

10.05.3.2.3 Spectral analysis

A 719 degree and order spherical harmonic shape model (VenusTopo719) of Venus was constructed by the author based on the Magellan GTDR3.2 sinusoidally projected data product (see **Table 1**). Missing nodes were filled by data obtained by the Pioneer Venus and Venera 15/16 missions; the remaining gaps were filled by interpolation using the Generic Mapping Tools (GMT) (Wessel and Smith, 1991) command <pr>surface</pr> with a tension parameter of 0.35, and the spherical harmonic expansion was performed using the sampling theorem of Driscoll and Healy (1994). The resulting power spectrum was found to be insensitive to changes in the tension parameter, and the mean planetary radius varied by about 1 m among the various models. A comparison between this spherical harmonic model and the one of Rappaport et al. (1999) shows that the latter suffers from an increasing loss of fidelity with increasing degree (the degree correlation between the two models is ~0.93 at 360°).

Power spectra of the Venusian topography (VenusTopo719) and geoid (MGNP180U) are shown in the left panel of **Figure 4**. These are similar to those of Earth, with the exception that the amplitudes of the degree-1 and degree-2 topographic terms for Venus are relatively smaller. On a log–log plot (data not shown), a change in slope of the topographic power spectrum occurs near degree 100 (Rappaport et al., 1999). This feature might be real, but it is also possible that it is related to interpolating over data gaps before performing the spherical harmonic expansion. The error spectrum of the geoid is seen to be greater than the geoid itself for degrees greater than 65. Though the global values of the potential coefficients are generally unreliable beyond this degree, it should be noted that the spatial resolution of the gravitational field is a strong function of position on the surface. Discontinuities in the error spectrum

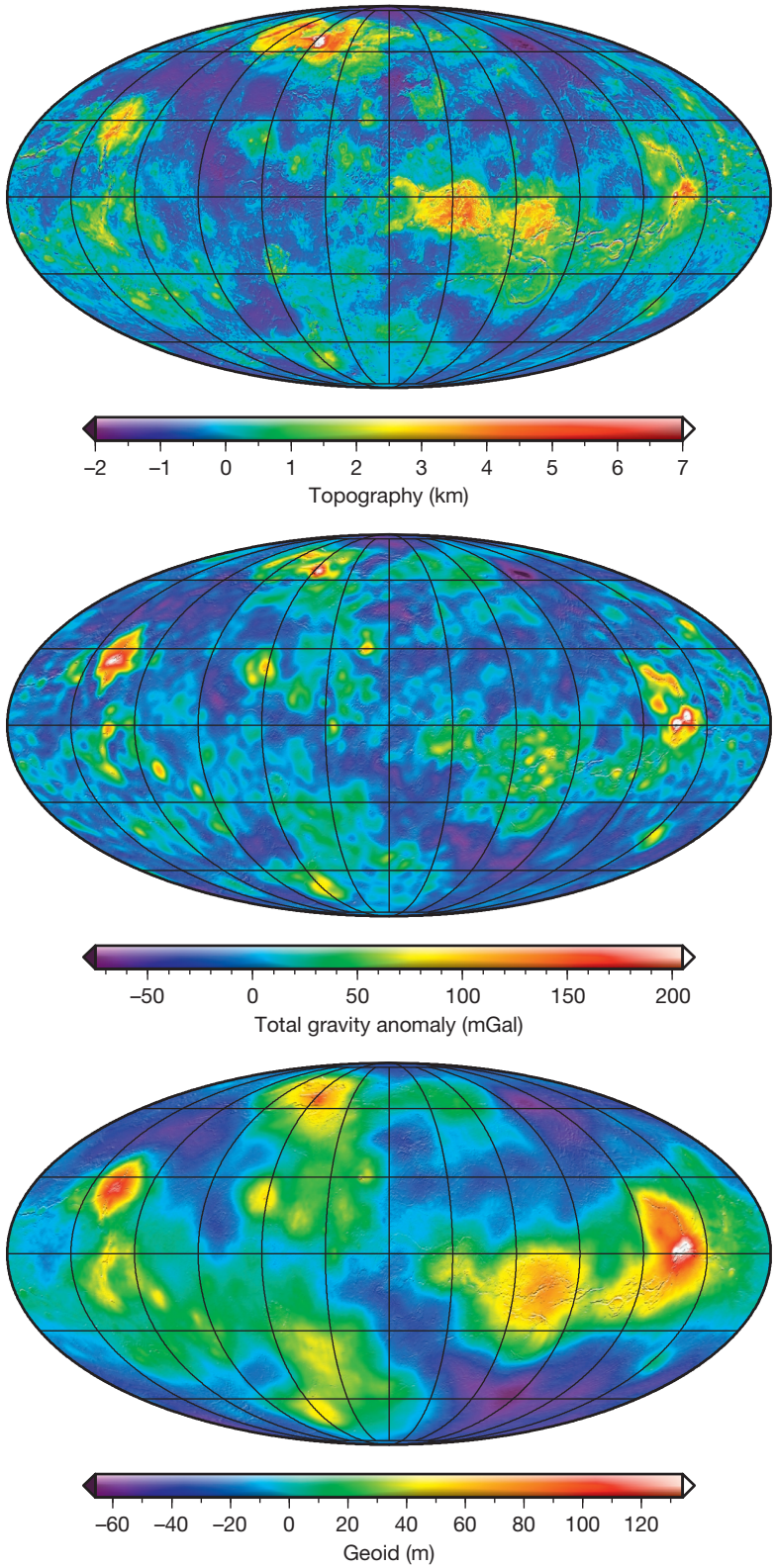

Figure 3 (Top) Global topography of Venus, derived from the spherical harmonic model VenusTopo719, referenced to the geoid. (Middle) Total free-air gravitational anomaly, obtained after truncating the spherical harmonic coefficients of MGNP180U beyond degree 65. (Bottom) Second-order approximation to the geoid. All images are in a Mollweide projection with a central meridian of 60°E longitude and are overlain by a gradient image derived from the topographic model.

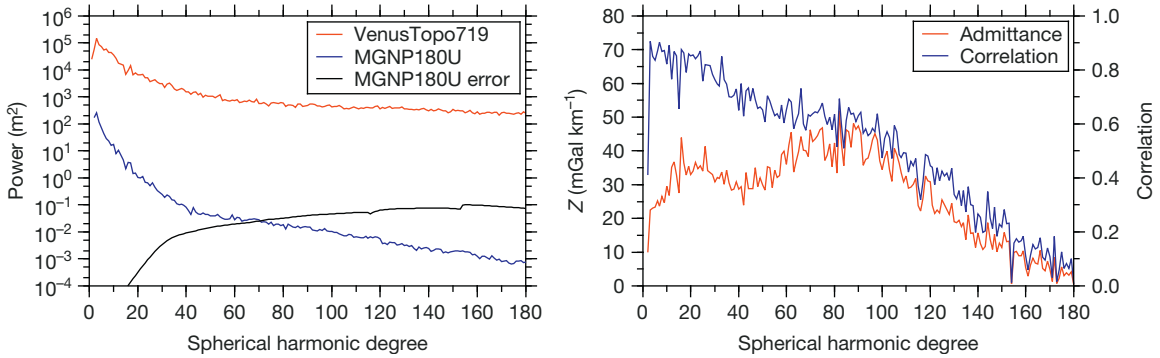

Figure 4 Power and cross power spectra of the gravity and topography of Venus. (Left) Power spectra of the topography (VenusTopo719), geoid (MGNP180U), and geoid error. (Right) Admittance and correlation spectra of the radial gravity and topography. The correlation spectrum is calculated using the spherical harmonic coefficients of the observed free-air gravity and gravity predicted from topography.

are artifacts of solving for the potential coefficients in three separate steps.

The spectral admittance and correlation functions for the radial component of the gravitational field and topography, plotted in the right panel of Figure 4, are seen to differ significantly from those of Earth. The admittance possesses values between ~30 and 50 mGal km^{-1} for spherical harmonic degrees up to 100, whereas for Earth, the admittance linearly increases from ~0 to 70 mGal km^{-1} up to degree 250. The correlation between the gravitational field and topography is also significantly higher for degrees less than 40 than it is for Earth. Nevertheless, beyond about degree 100, the spectral correlation and admittance are seen to decrease linearly with increasing degree, which is a result of the poor determination of the global potential coefficients. It is of note that both the admittance and correlation for degree 2 are significantly smaller than the neighboring values. As these are unaffected by the slow retrograde rotation of the planet, these low values may demand an origin that is distinct from the higher degrees.

Because the Pioneer Venus Orbiter and Magellan spacecraft were in near-polar orbits, the gravity field is better determined for the near-sectoral terms. Sectoral terms correspond to the case $|m|=l$, for which the corresponding spherical harmonic functions do not possess any latitudinal zero crossings. By considering only those coefficients where $l-|m|<20$, Konopliv et al. (1999) had shown that both the admittance and correlation between gravity and topography are considerably greater than when considering all coefficients combined. In particular, the correlation function remains close to 0.7 for degrees up to 140, at which point it decreases substantially. Thus, while high-degree localized spectral analyses may be justified on Venus, the fidelity of the spectral estimates will be a strong function of both position and the spherical harmonic degree and order.

10.05.3.3 Mars

10.05.3.3.1 Topography

Prior to the 1990s, the best Martian topographic models were constructed by a combination of Earth-based radar data, spacecraft radio occultations, and stereo and photoclinometric observations, all of which suffered from either large uncertainties or a limited spatial extent (for a review, see Esposito et al., 1992). The laser altimeter onboard the MGS spacecraft (MOLA, Mars Orbiter Laser Altimeter) has since collected an impressive dataset that has revolutionized studies of the Martian surface (see Smith et al., 2001a, 1999; Zuber et al., 2000b).

MOLA made more than 640 million ranges to the surface over the period of 4 years, after being inserted into orbit in 1997. The spot size of the laser at the surface was ~168 m, and these were spaced every 300 m in the along-track direction of the spacecraft orbit. The intrinsic range resolution of the instrument was 37.5 cm, but range precision decreases with increasing surface slope and could be as poor as 10 m for slopes near 30°. Whereas the along-track orbit errors are less than the size of the laser footprint, radial orbit errors could sometimes be as high as 10 m. Nevertheless, these orbit-induced errors could be minimized by the use of altimetric crossovers. Crossovers occur whenever two altimeter ground tracks intersect, and the difference in the two elevation measurements is largely a reflection of errors in the orbit determination. By parameterizing these uncertainties by a slowly varying function, the crossover residuals can be minimized (Neumann et al., 2001). Such a procedure was capable of reducing the rms crossover residuals from about 8.3 to 1.8 m. Using these methods, it has been possible to measure temporal variations in CO_2 snow depth that can reach 2 m in the polar regions (Smith et al., 2001b).

The topography of Mars (as determined from the 2600-degree spherical harmonic model MarsTopo2600; see in the succeeding text) referenced to the geoid (calculated to second-order accuracy) is displayed in Figure 5. Two of the most remarkable features are the dichotomy in elevation between the Northern and southern hemispheres and the regionally high elevations of the Tharsis volcanic province that is centered near the equator at 100°W longitude. These two features give rise to a 3.3 km offset of the center of figure from the center of mass that is directed toward 64°S and 99°W, of which the longitudinal offset is directed toward the Tharsis province. In addition to these long-wavelength features, there is also an ~20 km difference between the polar and equatorial radii that is a result of the planet's rotational flattening.

Other major topographic features include the giant Hellas (40°S, 65°W), Argyre (50°S, 40°W), and Isidis (15°N, 85°E)

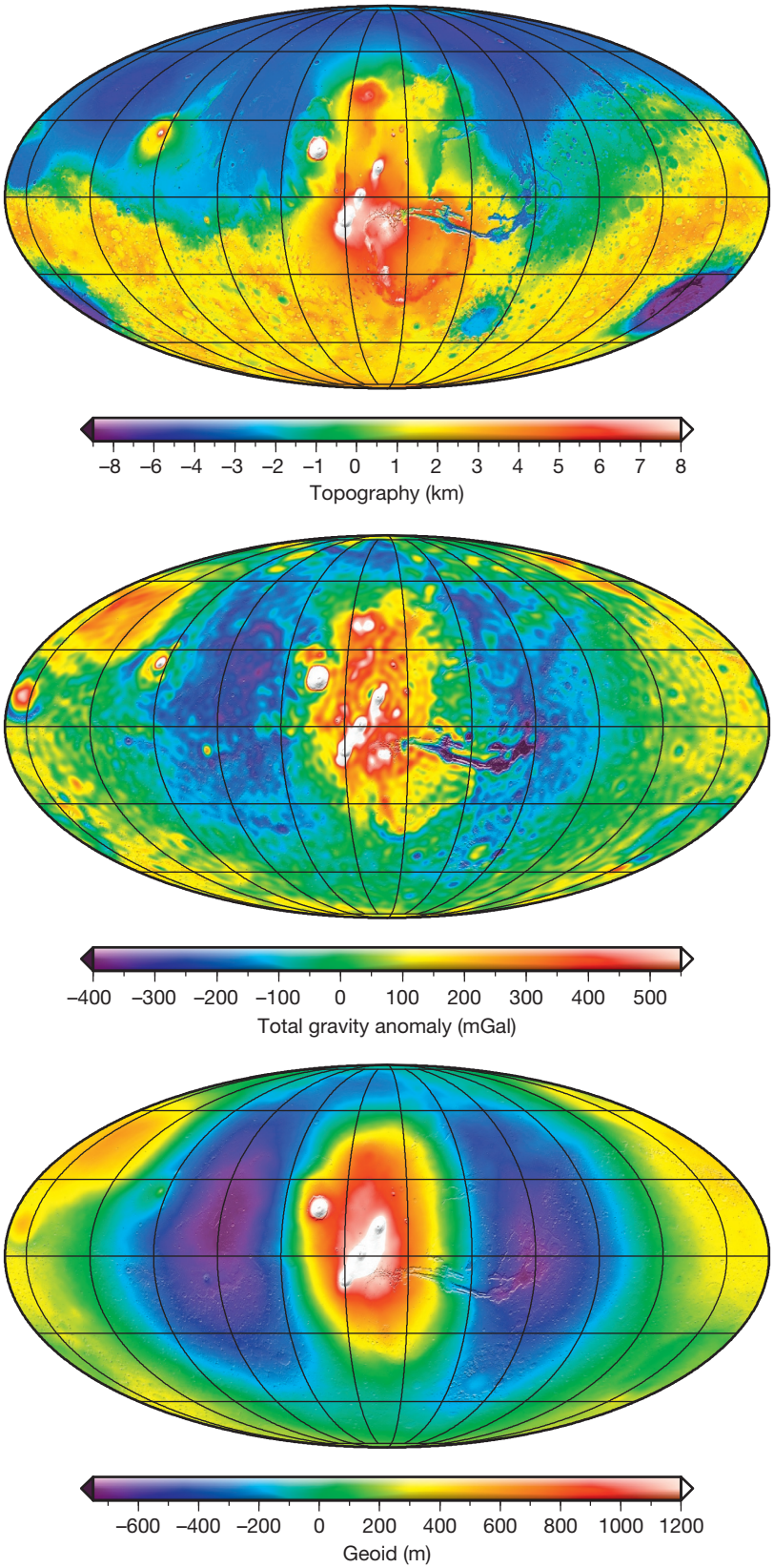

Figure 5 (Top) Global topography of Mars derived from the spherical harmonic shape model MarsTopo2600, referenced to the geoid. (Middle) Total free-air gravitational anomaly on the rotating reference ellipsoid of Ardalan et al. (2010), obtained after truncating the spherical harmonic coefficients of JGMRO_110C beyond degree 85. (Bottom) Second-order approximation to the geoid height with respect to the reference ellipsoid. All images are in a Mollweide projection with a central meridian of 100°W longitude and are overlain by a gradient image derived from the topography model.

impact basins; the Elysium volcanic province (25°N, 145°E); the rift valley Valles Marineris; and the prominent volcanoes that are superposed on the Tharsis province. The highest elevation corresponds to the volcano Olympus Mons, which rises almost 22 km above the MOLA reference geoid.

10.05.3.3.2 Gravity

The gravitational field of Mars has been improved by the successive acquisition of radio tracking data from the Mariner 9, Viking 1 and 2, MGS, Mars Odyssey, and Mars Reconnaissance Orbiter (MRO) missions. A major improvement in the gravity solutions came with the acquisition of data from the MGS mission (see Konopliv et al., 2006; Lemoine et al., 2001; Yuan et al., 2001). This spacecraft was in a near-polar orbit, and during the early portion of the mission when the orbit was highly elliptical, tracking data from altitudes as low as 170 km were acquired at latitudes between 60° and 85°N. Through the technique of aerobraking, the spacecraft was put into a near-circular mapping orbit with periapse and apoapse altitudes of 370 and 435 km, respectively. Mars Odyssey acquired some tracking data from altitudes as low as ~200 km (primarily over the southern hemisphere), with the rest from a near-circular 390 × 455 km mapping orbit. The last major advance was the collection of tracking data from the MRO spacecraft. For this mission, tracking data were acquired from an elliptical orbit with periapse altitudes as low as 255 km over the south pole and apoapse altitudes of 320 km over the north pole. Data were also collected for a brief period with altitudes as low as 220 km over the northern hemisphere.

The most recent and highest resolution gravity solution of Mars is the JPL 110 degree and order model JGMRO_110C (Konopliv et al., 2011). This model employs MGS, Mars Odyssey, and MRO tracking data in combination with surface tracking data from the Pathfinder lander, the latter of which were used to improve knowledge of the orientation of Mars. In the absence of a priori constraints, inversions for the global spherical harmonic coefficients give rise to an unrealistic power spectrum beyond degree 85. In order to obtain a higher-resolution model with realistic power, a Kaula constraint was applied beyond this degree. This solution also obtained the seasonal even zonal J_2 and the better determined odd zonal J_3 signals that result from CO_2 mass exchange between the two polar ice caps and the k_2 Love number from time-variable signals associated with tides raises by the Sun.

An image of the total gravitational anomaly of the model JGMRO_110C is plotted in Figure 5, where the spherical harmonic coefficients have been truncated beyond degree 85. For this map, the normal gravity field predicted for the Mars rotating reference ellipsoid of Ardalan et al. (2010) was removed. Clearly visible are the large positive anomalies associated with the volcanoes in the Tharsis plateau and a negative gravity moat that surrounds this province (Phillips et al., 2001). Large positive anomalies are also evident for some of the largest impact basins, such as Isidis, Argyre, and the buried Utopia basins (45°N, 110°E) that lie in the northern plains. A negative gravitational anomaly is clearly associated with the Valles Marineris rift valley, and negative anomalies surrounding some mountains and volcanoes seem to indicate a flexural origin. The spatial resolution of this field varies laterally, with an effective resolution near spherical harmonic degree 86 for northern latitudes and 110 near the south pole. Formal uncertainties in the radial gravity are at most 10 mGal (A. Konopliv, personal communication).

The Martian geoid, as obtained from the model JGMRO_110C and plotted with respect to the reference ellipsoid of Ardalan et al. (2010), is shown in Figure 5. The geoid undulations of Mars are seen to possess the largest amplitudes among the terrestrial planets, with a dynamic range of over 2.5 km. The signal is largely symmetrical about the Tharsis province, where a central geoid high is surrounded by an annular low. Other geoid highs are associated with the Isidis and Utopia impact basins, as well as the Elysium volcanic rise. Uncertainties in the geoid are generally no more than 2 m (A. Konopliv, personal communication).

10.05.3.3.3 Spectral analysis

The power spectra of the Martian topography (from the author's spherical harmonic model MarsTopo2600, calculated from the gridded datasets available at the PDS (planetary data system) website) and geoid (JGMRO_110C), are plotted in Figure 6. In comparison with the topographic power spectrum, the Martian geoid is seen to have greater amplitudes by about two orders of magnitude than both Earth and Venus. Furthermore, the first 5 degrees of the Martian geoid is considerably greater than would be expected based upon an

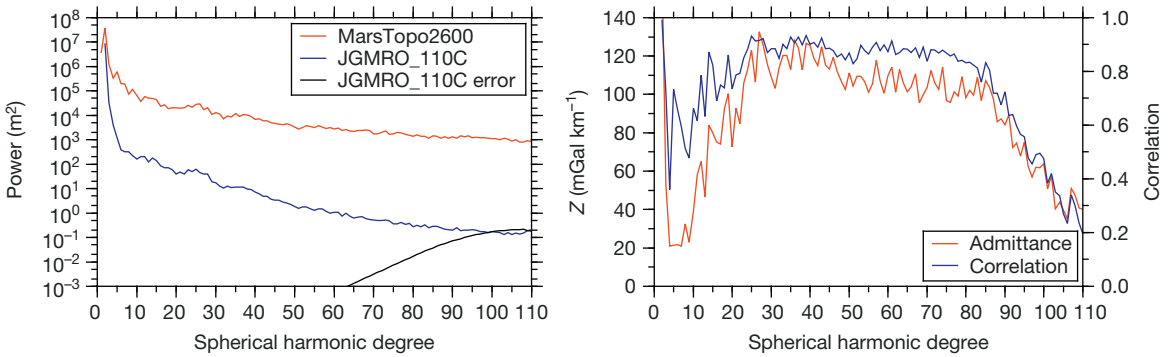

Figure 6 Power and cross power spectra of the gravity and topography of Mars. (Left) Power spectra of the topography (MarsTopo2600), geoid (JGMRO_110C), and geoid error. (Right) Admittance and correlation spectra of the radial gravity and topography. The correlation spectrum is calculated using the spherical harmonic coefficients of the observed free-air gravity and gravity predicted from topography.

extrapolation of the higher-degree terms. This low-degree signal is likely a consequence of the lithospheric load and deflection associated with the Tharsis province (see Phillips et al., 2001; Zuber and Smith, 1997). The error spectrum of the geoid is seen to be larger than the signal for degrees greater than ~100.

The admittance and correlation of the radial gravitational field and topography are shown in the right panel of Figure 6. The admittance function gradually increases with increasing degree, attaining a relatively constant value beyond degree 30. Beyond degree 85, both the admittance and correlation decrease as a result of the poor resolution of the gravity field. While the shape of the admittance function is somewhat similar to that of Earth, it is important to note that the amplitudes are considerably larger at high degrees (~100 mGal km^{-1} in comparison with ~35 mGal km^{-1}). Indeed, these large values are comparable to what would be expected for uncompensated surface topography. One apparent anomaly with the admittance spectrum is the relatively high value of 53 mGal km^{-1} for the degree-three term.

With few exceptions, the correlation between the gravity and gravity predicted from topography is also seen to be very high, with values between about 0.8 and 0.9. Similar to the Venusian gravity model, the near-sectoral terms of the Martian gravity solutions are relatively better determined because of the near-polar orbits of the MGS and MRO spacecraft. When only these near-sectoral terms are used ($l - |m| < 10$), the correlation between the gravity and topography is considerably larger than that shown in Figure 6 for degrees greater than 85 (Konopliv et al., 2011).

10.05.3.4 Mercury

10.05.3.4.1 Topography

Prior to the MErcury Surface, Space ENvironment, GEochemistry, and Ranging mission, MESSENGER (Solomon et al., 2001), the shape of Mercury was only poorly constrained by Earth-based radar ranging to equatorial latitudes (Anderson et al., 1996a; Clark et al., 1988; Harmon et al., 1986) and by a few local elevations models made from Mariner 10 stereo imagery (André et al., 2005). MESSENGER has since acquired a wealth of topographic data by means of satellite laser altimetry (Smith et al., 2010c; Zuber et al., 2008, 2012), stereophotogrammetry (Preusker et al., 2011), optical limb measurements (Oberst et al., 2011), and spacecraft radio occultations (Perry et al., 2011). The spacecraft continues to acquire data in an extended mission.

MESSENGER was launched in 2004, performed three flybys of Mercury in 2008–09, and was placed into a near-polar orbit in 2011. The orbit of the spacecraft during the mapping phase was highly elliptical, with altitudes varying from about 200 km at latitudes near 60°N to about 15 200 km over the southern hemisphere. Because of this, the laser altimeter could range southward only to 15°S. The laser spot size on the surface varied with altitude, from about 15 to 100 m, and the laser shots were separated by about 400 m along track. The near-polar orbit led to dense altimetric coverage near the north pole, decreasing coverage toward the equator. Supplementing these measurements, ~180 radio occultation point measurements of the planet's shape were made when the spacecraft passed behind the planet, with about half of these being located in the southern hemisphere. The processing of stereo imagery has led to the construction of a global elevation model, and a future challenge is to combine the stereo-derived shape models with the laser altimetry and radio occultation data.

The global shape of Mercury derived from stereo imaging (R. Gaskell, personal communication) is shown in Figure 7. As expected from images of the surface, the planet has been shaped largely by impact processes. Several large impact basins, such as the 1500 km diameter Caloris basin (31°N, 160°E), are visible as are numerous smaller craters. The largest basins are not as topographically distinct as those on Mars and the Moon, suggesting that post-basin modification processes have operated after their formation. One clear example of this is the topographic bulge in the northern portion of the Caloris impact basin that is higher than most of its topographic rim (Zuber et al., 2012). Smooth plains are also present, particular at latitudes poleward of about 60°N, that are likely to represent volcanic flows (Zuber et al., 2012). In terms of the planet's long-wavelength shape, the highest elevations are found approximately near 0° and 180° longitude, which corresponds to the axis of the planet's minimum principal moment of inertia (e.g., Davies and Batson, 1975).

10.05.3.4.2 Gravity

The gravity field of Mercury has been constrained by radio tracking of the Mariner 10 and MESSENGER spacecraft. Tracking data from Mariner 10 were acquired only during two flybys, and these allowed for an estimation of the degree-2 gravity coefficients J_2 and C_{22} (Anderson et al., 1987). Radio tracking of the MESSENGER spacecraft has since given rise to a dramatic improvement in our understanding of Mercury's gravity field, with global solutions being developed to spherical harmonic degree and order 20 (Genova et al., 2013; Smith et al., 2012). Nevertheless, as a result of the highly eccentric orbit of the spacecraft, the global models are poorly constrained over the southern hemisphere. Whereas errors in the surface gravity field are less than 20 mGals at latitudes poleward of 30°N, errors are more than 60 mGals at latitudes southward of about 30°S (Genova et al., 2013). Gravity models with higher spatial resolution over the northern hemisphere should be possible by using localized inversion approaches (cf. Han et al., 2009) or with a spatially varying constraint as was done for Venus (Konopliv et al., 1999).

The total gravitational anomaly of the model GGMES_20v04 is plotted in Figure 7, where several positive gravitational anomalies are visible with values approaching 180 mGal. Some of these anomalies are associated with clear topographic signatures, such as the Caloris impact basin and a domical rise in the northern lowlands (Smith et al., 2012), whereas others appear to have little correlation with topography. The volcanic northern lowlands (north of about 60°N) are associated with a regional negative gravitational anomaly, as are the low elevations associated with the large Rachmaninoff impact basin (28°N, 56°E). Large regions of high-standing topography do not possess any significant gravitational anomaly, indicating that they are likely to be isostatically compensated.

The height of the geoid of Mercury, measured with respect to the mean planetary radius, has a dynamic range of about 400 m. As seen in Figure 7, the planet has prominent signals

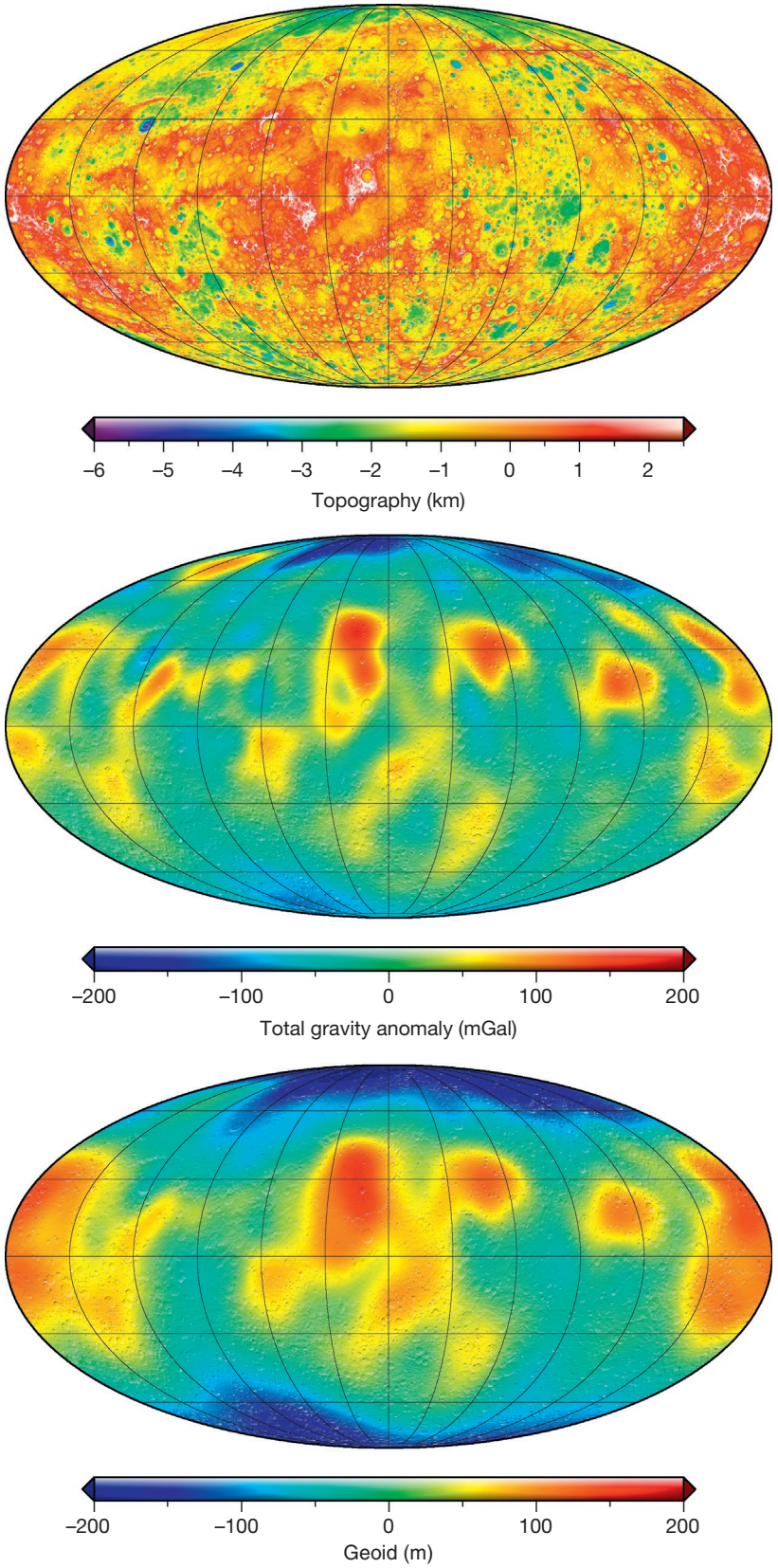

Figure 7 (Top) Global topography of Mercury (R. Gaskell, personal communication), referenced to the geoid. (Middle) Total free-air gravitational anomaly from the spherical harmonic model GGMES_20v04. (Bottom) Second-order approximation to the geoid. All images are in a Mollweide projection with a central meridian of 180°E longitude and are overlain by a gradient image derived from the topographic model.

that arise from the J_2 and C_{22} gravity coefficients. This corresponds to positive geoid anomalies located near 0° and 180° longitude and negative anomalies near both poles, reminiscent of that of the Moon. The C_{22} coefficient is proportional to the difference in the intermediate and minimum principal moments of inertia (e.g., Lambeck, 1988) and is responsible for Mercury having been captured in its present 3/2 spin–orbit resonance (cf. Correia and Laskar, 2009).

10.05.3.4.3 Spectral analysis

A spherical harmonic model of the shape of Mercury was constructed from the MESSENGER laser altimeter and radio occultation data (GTMES_24v01; Smith et al., 2012). The power spectra of this model, the geoid from the model GGMES_20v04, and the geoid error are plotted in **Figure 8**, and the relative amplitudes of the topography and geoid spectra are seen to be comparable to those of Mars. As the error spectrum of the geoid does not intersect that of the geoid, it should be possible to construct higher-resolution models over the northern hemisphere.

The correlation and admittance spectra of the gravitational field and topography are shown in the right panel of **Figure 8**. In this plot, the correlation spectrum was calculated using the observed free-air gravity and the gravity predicted from the surface topography. With the exception of degree 4, the admittance possesses values of a few tens of mGal km^{-1}. This is much less than the value predicted for uncompensated surface topography, indicating that much of the topography at these wavelengths is probably compensated. The correlation possesses values between about 0.4 and 0.8, which is somewhat similar to Mars and the Moon over the same wavelength range. The less than unit correlation is likely a consequence of the presence of mascon basins, such as Caloris, where the gravity and topography are locally anticorrelated, as well as the presence of gravitational anomalies from the mantle and deep crust that do not correlate with surface topography.

10.05.3.5 The Moon

10.05.3.5.1 Topography

The topography of the Moon has been measured by several means, including satellite altimetry, stereophotogrammetry, and radar interferometry (see Wieczorek et al., 2006, for an historical review). However, because of the Moon's synchronous rotation, most early studies were restricted either to the nearside hemisphere or along the equatorial ground tracks of the Apollo command and service modules. The Clementine mission, launched in 1994, was the first to measure absolute elevations of the lunar surface on a near-global scale (Smith et al., 1997; Zuber et al., 1994). 72 548 valid altimetric ranges were acquired along north–south profiles equatorward of ~80°, and in combination with elevation models of the polar regions based on stereophotogrammetry, a global shape model was created (U.S. Geological Survey, 2002). The next major advance came from laser altimetric ranging from three orbiting spacecraft: Kaguya (Araki et al., 2009) and Chang'e 1 (Ping et al., 2009), both launched in 2007, and LRO launched in 2009 (Smith et al., 2010a,b). In addition to including laser altimeters, the acquisition of stereo imagery from these missions has led to the construction of both regional and global terrane models (e.g., Haruyama et al., 2008; Scholten et al., 2012).

The most successful of the recent lunar altimeters is the Lunar Orbiter Laser Altimeter (LOLA) (Smith et al., 2010a,b) onboard the LRO mission. LOLA is a multibeam laser altimeter that operates by spitting a single laser pulse into five output pulses. A five-spot cross pattern is formed on the surface by constructive interference in the far field, which is then detected by five individual receivers, each with a range accuracy of about 10 cm. The spot size of each laser on the surface is 5 m, and the distance between spots is 25 m. The orbital motion of the spacecraft, combined with the 28 Hz repetition frequency, ensures that each five-spot pattern is repeated every 50 m. Bidirectional surface slopes can be calculated for each laser shot or for a variety of longer baselines (Rosenburg et al., 2011). At the present time, more than 6 billion valid ranges have been made to the Moon, and an additional 2 billion are expected over the lifetime of the laser. Since the orbit of the Lunar Reconnaissance Orbiter is polar, the altimetric coverage near the poles is extremely dense. Nevertheless, some kilometer-scale data gaps exist at equatorial latitudes. Stereo imagery can be used to create elevation models with resolutions approaching about 10 m (Haruyama et al., 2008) to 75 m (Scholten et al., 2012), and a future challenge is to combine the altimetric and stereo-based elevation models.

It should be noted that there are two reference frames that are in common use for the Moon (Archinal et al., 2011a,b).

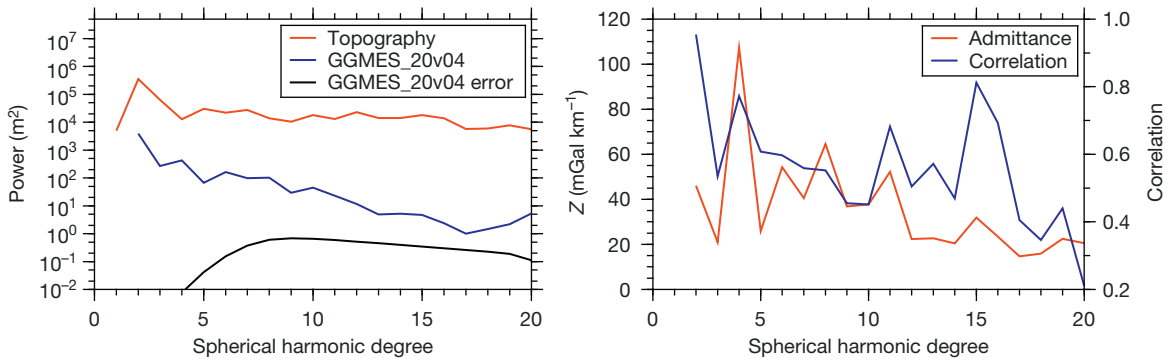

Figure 8 Power and cross power spectra of the gravity and topography of Mercury. (Left) Power spectra of the topography (GTMES_24v01), geoid (GGMES_20v04), and geoid error. (Right) Admittance and correlation spectra of the radial gravity and topography. The correlation spectrum is calculated using the spherical harmonic coefficients of the observed free-air gravity and gravity predicted from topography.

One corresponds to the principal axes defined by the moments of inertia, which is used in the construction of gravitational models. The other is defined by the mean position of Earth and the Moon's rotation axis and is used for many topographic models. The two coordinate frames are mostly offset by a bias with maximum differences up to 873 m, which turns out to be significant when analyzing the high-resolution GRAIL gravity data (Williams et al., 2013). The LOLA topography model (using principal-axis coordinates) is presented in Figure 9 where it is referenced to the GRAIL geoid.

The most dramatic feature of the Moon's topography is the giant South Pole–Aitken impact basin on the farside southern hemisphere. This impact basin possesses a total relief of more than 10 km, and with a diameter of over 2000 km, it is the largest recognized impact structure in the solar system. Other impact basins and craters of various sizes are seen to have shaped the relief of the lunar surface, and the extensive mare basaltic lava flows on the nearside hemisphere, which are relatively younger, are seen to be comparatively smooth. Also of note is that the Moon possesses a 1.9 km displacement of its center of figure from its center of mass in the direction of 8°N and 157°W (e.g., Smith et al., 1997). The total dynamic range in lunar elevation is just under 20 km.

10.05.3.5.2 Gravity

The gravitational field of the Moon has been determined by the radio tracking of orbiting spacecraft and by intersatellite ranging between co-orbiting spacecraft. Radio tracking data from the Lunar Orbiter, Apollo, Clementine, and Lunar Prospector missions led to the development of a degree-150 spherical harmonic model (Konopliv et al., 2001). However, even though the nearside field was moderately well resolved by the 30 km altitude Lunar Prospector data, little was known about the farside hemisphere as it is not possible to track a satellite when it is occulted by the Moon. The first direct tracking data over the farside hemisphere came from the Kaguya mission that was launched in 2007. In addition to the main orbiter (with an altitude of about 100 km), this mission had a relay satellite for performing four-way radio tracking of the main satellite over the farside hemisphere and a subsatellite for very long baseline interferometry (Araki et al., 2009; Goossens et al., 2011; Matsumoto et al., 2010). Data from the Kaguya mission provided a gravitational model that was valid globally to about spherical harmonic degree 70.

The last major advance came with the launch of the GRAIL mission in 2011 (Zuber et al., 2013a,b). This mission was very similar to the terrestrial mission GRACE, in that intersatellite ranges between two co-orbiting spacecraft were used to construct a global gravity model. During the 3 months of the primary mission, the two spacecraft had a mean altitude near 50 km, allowing for the construction of models up to spherical harmonic degree 660 (Konopliv et al., 2013b; Lemoine et al., 2013). During the 3 months extended mission, the altitudes of the two spacecraft were reduced to about 25 km, allowing for the construction of models up to spherical harmonic degree 900. Since the satellite orbits were somewhat elliptical, the minimum elevations over the lunar surface range from only a few kilometers to about 30 km. Though the final models are valid globally to about spherical harmonic degree 750, it is possible to perform localized analyses to higher resolutions where the spacecraft elevations were low.

The total gravitational anomaly and geoid of the GRAIL extended mission model GRGM900B (truncated at degree 550) are plotted in Figure 9. The major features of this map include the large positive gravitational anomalies associated with the nearside impact basins, colloquially referred to as 'mascons' (e.g., Muller and Sjogren, 1968), and the negative gravity moats that surround these basins. The majority of the gravity signal is a result of the surface relief of the Moon, but important signals that are uncorrelated with topography are observed in the lunar mare and elsewhere.

In contrast to Earth, which possesses maximum geoid undulations of ± 100 m, the dynamic range of the lunar geoid is more than 1.1 km. When considering phenomena such as basalt flow directions, it is thus necessary to use elevations that are referenced to the geoid. A long-wavelength J_2 and C_{22} signal is evident in Figure 9, with maxima at the sub- and anti-Earth points, and this signal may represent a fossil tidal deformation that was frozen into the lithosphere early in the orbital evolution of the Moon (e.g., Garrick-Bethell et al., 2006; Jeffreys, 1976; Lambeck and Pullan, 1980).

Finally, it is noted that the orientation of the Moon depends upon its three principal moments of inertia, which are related to the degree-2 gravity coefficients (e.g., Lambeck, 1988). For a synchronously rotating satellite with zero orbital inclination and eccentricity, the minimum energy configuration is achieved when the maximum moment of inertia lies along the rotation axis and when the minimum moment coincides with the Earth–Moon direction (see also Peale, 1969; Ward, 1975). A 180° rotation of the Moon about its rotation axis, as might occur following a large impact event (Wieczorek and Le Feuvre, 2009), would thus be equally stable as its current configuration.

10.05.3.5.3 Spectral analysis

The power spectra of the LOLA principal-axis referenced topography (from the author's model LOLA2600p) and the GRAIL GRGM900B geoid are plotted in the left panel of Figure 10. In comparison with Earth, the power spectrum of the lunar geoid is seen to be about two orders of magnitude more important when compared to the topography spectrum. The lunar geoid and error spectra intersect near degree 750, which is the effective global resolution of the model. Nevertheless, since the GRAIL spacecraft possessed altitudes varying from a few to 30 km during the extended mission, the spatial resolution of the model is in some places better or worse than this spherical harmonic degree. The small upturn in the geoid spectrum near degree 850 is a result of higher-degree aliases that are not resolved by the degree-900 model, indicating that it will be possible to construct even higher-resolution models.

The correlation and admittance spectra for the gravity and topography are plotted in the right pane of Figure 10. In this plot, the correlation spectrum was calculated using the observed free-air gravity and the gravity predicted from the surface topography. The correlation and admittance spectra show low values at the lowest degrees (less than about 0.5 and 100 mGal km^{-1}, respectively). Indeed, these spectra possess negative values for some degrees, indicating that gravity

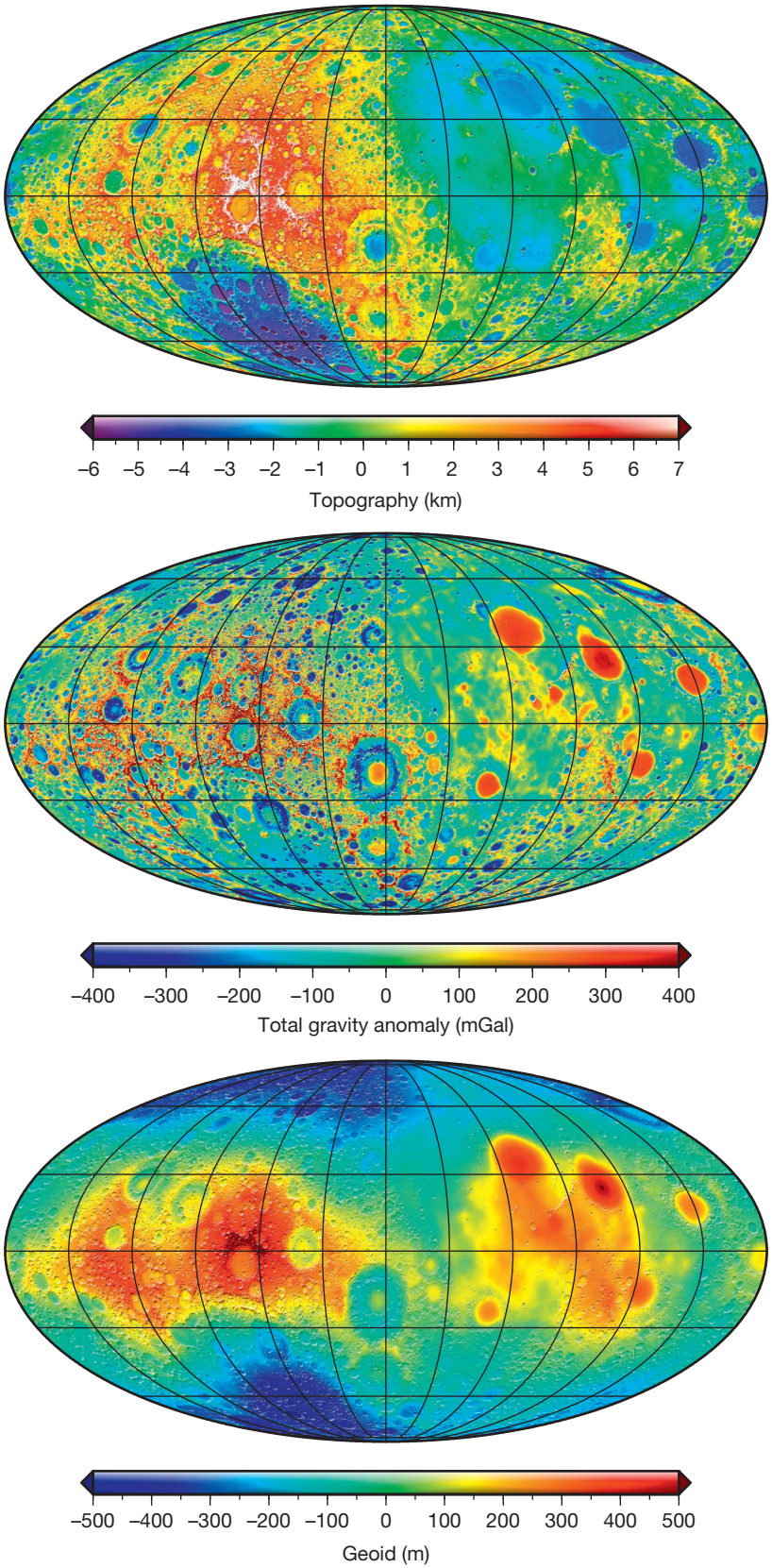

Figure 9 (Top) Global topography of the Moon from the spherical harmonic model LOLA2600p, referenced to the GRGM900B geoid. (Middle) Total gravity obtained from the model GRGM900B evaluated at mean planetary radius after truncating the coefficients beyond degree 550. (Bottom) Second-order approximation to the geoid. All images are in a Mollweide projection with a central meridian of 90°W longitude and are overlain by a gradient image derived from the topographic model. The near- and farside hemispheres are on the right and left halves of these images, respectively.

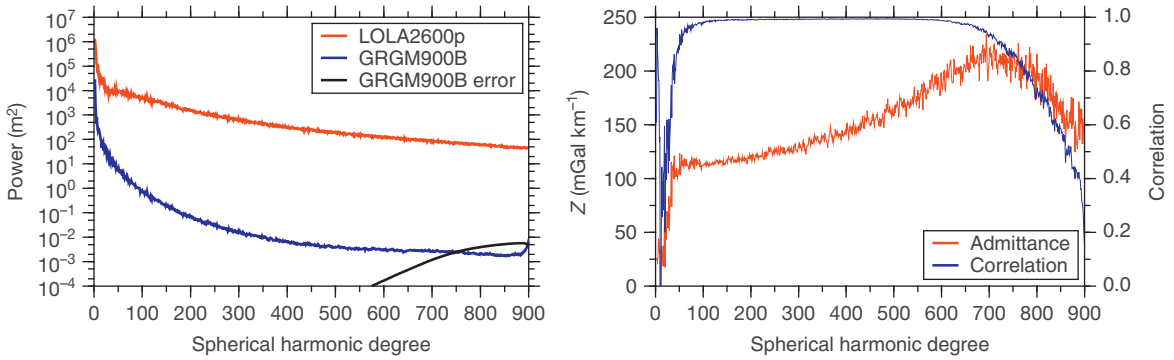

Figure 10 Power and cross power spectra of the gravity and topography of the Moon. (Left) Power spectra of the topography (LOLA2600p), geoid (GRGM900B), and geoid error. (Right) Admittance and correlation spectra of the radial gravity and topography. The correlation spectrum is calculated using the spherical harmonic coefficients of the observed free-air gravity and gravity predicted from topography.

and topography are anticorrelated at these wavelengths. These small values for the lowest degrees are simply a result of the presence of mascon impact basins, which are positive gravitational anomalies that possess low elevations. Beyond about degree 100, the correlation approaches 0.99, and the admittance slowly increases from values near 100 to about 200 mGal km^{-1}. The value of the admittance at these degrees is consistent with uncompensated topography (Wieczorek et al., 2013), and the slow increase in the admittance function is a result of the nonlinear relation between gravity and topography (see Section 10.05.4). The correlation starts to decrease near degree 550, and this could be a result of a reduced global fidelity of the gravity model at these degrees or to short-wavelength geologic signals where the gravity and topography signals are not perfectly correlated.

10.05.4 Methods for Calculating Gravity from Topography

Geophysical investigations that employ gravitational and topographic data often attempt to fit the observations with those predicted from a model that contains several parameters. For example, lithospheric flexure calculations depend upon several unknowns, including the effective elastic thickness of the lithosphere, crustal thickness, and the density of the crust and mantle. By comparing predicted gravitational anomalies induced by the deflection of density interfaces with the observed values, the parameters of such a model can be constrained. Whereas several methods exist for calculating the gravitational field related to relief along a density interface, as is described in the succeeding text, this is oftentimes most easily performed in the spherical harmonic domain.

The calculation of the gravitational potential can be considerably simplified by use of the two well-known identities:

$$\frac{1}{|\mathbf{r}-\mathbf{r}'|}=\frac{1}{r}\sum_{l=0}^{\infty}\left(\frac{r'}{r}\right)^{l}P_l(\cos\gamma)\quad \text{for}\, r\geq r' \qquad [30]$$

and

$$P_l(\cos\gamma)=\frac{1}{2l+1}\sum_{m=-l}^{l}Y_{lm}(\theta,\phi)Y_{lm}(\theta',\phi') \qquad [31]$$

where P_l is an unnormalized Legendre polynomial and γ is the angle subtended between $\mathbf{r}$ and $\mathbf{r}'$. (Equation [31] is commonly referred to as the Legendre addition theorem.) By inserting these equations into the expression for the gravitational potential (eqn [17]), it is simple to show that the spherical harmonic coefficients of eqn [19] (the *Stokes coefficients*) are equal to

$$C_{lm}=\frac{1}{MR_0^l(2l+1)}\int_V \rho(\mathbf{r}')r'^l Y_{lm}(\theta',\phi')\mathrm{d}V' \qquad [32]$$

It is important to note that this formulation of the gravitational potential can only be used when the observation point is greater than the maximum radius of the body.

Next, consider the case where there is relief $h(\theta, \phi)$ referenced to a spherical interface of radius D and where the density ρ between h and D depends only on latitude and longitude (when h is negative, ρ is considered negative as well). For this situation, it is possible to obtain exact expressions for the corresponding potential coefficients that are similar to those developed by Parker (1972) in the Cartesian domain. Integrating eqn [32] over r' and expanding powers of the relief in a Taylor series, the potential coefficients of eqn [19], referenced to a radius D, are (see Wieczorek and Phillips, 1998)

$$C_{lm}=\frac{4\pi D^3}{M(2l+1)}\sum_{n=1}^{l+3}\frac{(\rho h^n)_{lm}}{D^n n!}\frac{\prod_{j=1}^{n}(l+4-j)}{(l+3)} \qquad [33]$$

The spherical harmonic coefficients of the density multiplied by the relief to the nth power have the explicit expression (cf. eqn [8])

$$(\rho h^n)_{lm}=\frac{1}{4\pi}\int_\Omega[\rho(\theta,\phi)h^n(\theta,\phi)]Y_{lm}(\theta,\phi)\mathrm{d}\Omega \qquad [34]$$

and when the density is constant, eqn [33] reduces to eqn [9] of Wieczorek and Phillips (1998). As a result of the inequality in the identity of eqn [30], this expression for the potential is valid only when the radius r is greater than the maximum elevation of $D+h$. Extensions, special cases, and alternative forms of this equation have been derived independently several times in the literature (e.g., Balmino, 1994; Chambat and Valette, 2005; Chao and Rubincam, 1989; Martinec et al., 1989; Rapp, 1989). It is worth emphasizing that the relief h in eqn [33] must be calculated with respect to a spherical interface and not the ellipsoid or geoid: using a different reference surface would give inaccurate results.

For the case where the density ρ is constant, the potential coefficients can be obtained simply by calculating the spherical harmonic coefficients of the relief to the nth power. While the sum of eqn [33] is finite and hence exact, the number of terms grows linearly with spherical harmonic degree. Nevertheless, as each succeeding term is smaller than the previous, in practice, this sum can be truncated beyond a maximum value n_{max} for which the truncated terms are smaller than the resolution of the gravity model.

For certain applications, it is sufficient to use the first-order term of eqn [33]:

$$C_{lm} = \frac{4\pi D^2 (\rho h)_{lm}}{M(2l+1)} \qquad [35]$$

This expression is commonly referred to as the 'mass-sheet' approximation, as the calculated gravitational anomaly would be exact if it arose from a spherical interface with a surface density of ρh. (The higher-order terms are referred to as the 'finite-amplitude' or 'terrain' correction.) Using this expression, the radial gravity (see eqn [25]) is seen to approach asymptotically with increasing l the Bouguer slab approximation of $2\pi\rho Gh$.

The effect of truncating the sum of eqn [33] beyond n_{max} is illustrated in Figure 11 for the specific case of determining the Bouguer correction of Earth, Venus, Mars, Mercury, and the Moon. The term Bouguer correction here refers to the contribution of the gravitational potential that results from the mass between the mean planetary radius and the surface. The true value of the Bouguer correction was approximated using $n_{max} = 20$, and the maximum difference of the total gravity in the space domain that results from truncating at lower values of n was calculated on the planet's reference ellipsoid. For these calculations, the full resolution of the planetary topography was used in calculating the potential coefficients, but the resulting gravity field was expanded in the space domain only up to the spherical harmonic degree indicated in the figure. To mitigate against aliases that could arise when raising a function to the nth power, all calculations were performed on a grid that could resolve spherical harmonics up to degree 5000.

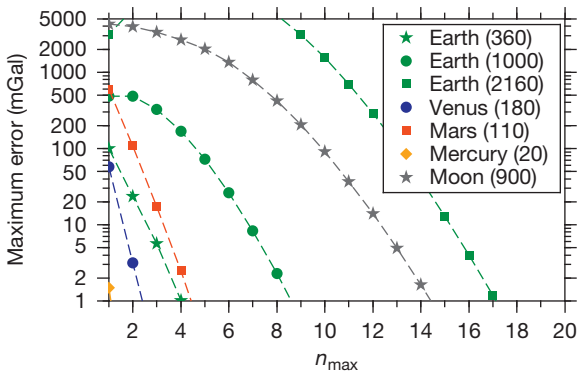

Figure 11 Maximum error associated with the Bouguer correction as a function of the order n_{max}. The Bouguer correction error is here defined as the error in the total gravitational attraction resulting from surface relief with respect to the mean planetary radius, evaluated on the reference ellipsoid. The true value was approximated by $n_{max} = 20$, and the crustal density was assumed to be 2900 kg m^{-3}. The values in parentheses correspond to the maximum spherical harmonic degree used in calculating the gravity field.

Figure 11 shows that the value of n_{max} required to achieve 1 mGal accuracy is highly dependent upon the maximum spherical harmonic degree of the desired gravitational field. To obtain accuracies of a few milligals for Mercury, Venus, and Mars, whose gravity fields are only resolved up to a maximum spherical harmonic degree of 180, only the first four terms of eqn [33] are required. However, when calculating high-resolution gravity fields for the Moon and Earth (with degrees up to 900 and 2160), it is necessary to utilize terms up to 14 and 17, respectively (see also Balmino et al., 2012). If it were necessary to calculate fields up to only spherical harmonic degree 360 for Earth (for use with the gravity model EGM96), then the first four terms would be sufficient.

Finally, it is noted that alternative means exist for calculating the theoretical gravitational field of a body and that these may be preferable to the aforementioned approach for certain applications. One method developed by Belleguic et al. (2005) is quasi-analytic and allows for the calculation of the potential and gravity at any point in a body (this is in contrast to the aforementioned approach that is applicable only to radii greater than the maximum radius). This method starts by mapping irregularly shaped density interfaces to spherical ones and then determines the radial derivatives of the potential and gravitational field on this surface. Using exact values for the potential and gravity field on an interface exterior to the planet (as obtained from a method similar to eqn [33]), these fields are then propagated downward using a first-order Taylor series approximation. This technique is useful for lithospheric flexure calculations as the net lithospheric load is a function of the potential at the major density interfaces.

A second method for calculating the gravitational field is based upon approximating the shape of a celestial body by a polyhedron. Exact expressions for the potential of a homogeneous polyhedron have been derived by Werner and Scheeres (1997), and expressions for the corresponding spherical harmonic coefficients are given in Werner (1997) (see also Tsoulis et al., 2009). The benefit of using this approach is that the resolution of the model (i.e., the spacing between vertices) can be varied according to the resolution of the gravitational field. An application of this method for determining the interior density of an asteroid is given by Scheeres et al. (2000). Alternatively, one could transform eqn [17] into a surface integral by use of Gauss' law and perform the integral numerically for a given shape model (e.g., Cheng et al., 2002).

10.05.5 Crustal Thickness Modeling

It is well known that the modeling of potential fields is nonunique. As an example, eqns [19] and [35] show that any external gravitational field can be interpreted as a surface density ρh placed at an arbitrary radius D. Nevertheless, by using simplifying assumptions based on geologic expectations, it becomes possible to invert uniquely for parameters related to the interior structure of a planet.

Perhaps the simplest example of such an investigation is the construction of a global crustal thickness model. In this case, the nonuniqueness associated with potential modeling is removed by assuming that the observed gravitational field arises only from relief along the surface and crust–mantle

interface and that the densities of the crust and mantle are known. It is further required either to assume a mean crustal thickness or to anchor the inverted crustal thickness to a given value at a specific locale. If lateral density variations in either layer could be constrained by other means, these could be incorporated into the model.

The first step is to calculate the Bouguer correction, which is the contribution to the potential of surface relief referenced to the mean planetary radius. Subtracting this from the observed gravitational field yields the Bouguer anomaly, and this is then ascribed to being caused by relief along the crust–mantle interface at an average radius D. To the first order, this relief could be determined in the spectral domain by downward continuing the Bouguer anomaly coefficients C_{lm}^{BA} to radius D and then setting these equal to those predicted from the mass-sheet approximation of eqn [35]. However, two additional factors generally need to be taken into account in such an analysis. First, downward continuing the Bouguer anomaly amplifies short-wavelength noise that is often present in the observed gravitational field. Second, the first-order mass-sheet approximation may not be sufficiently accurate if the undulations along the crust–mantle interface are large.

By minimizing the difference in the spectral domain between the observed and predicted Bouguer anomalies, the shape of the crust–mantle interface can be computed via the following equation (see Wieczorek and Phillips, 1998):

$$h_{lm} = w_l \left[\frac{C_{lm}^{BA} M (2l+1)}{4\pi \Delta \rho D^2} \left(\frac{R}{D} \right)^l - D \sum_{n=2}^{l+3} \frac{(h^n)_{lm}}{D^n n!} \frac{\prod_{j=1}^{n} (l+4-j)}{(l+3)} \right] \quad [36]$$

The density jump across the crust and mantle is given by $\Delta\rho$, R is the reference radius of the Bouguer anomaly coefficients, and w_l is a filter that stabilizes the downward continuation procedure. The explicit form of the filter can be determined by using an additional constraint that minimizes the mantle relief.

While there is no simple analytic solution to eqn [36], the relief h can be determined using an iterative approach: First, the coefficients h_{lm} are approximated by ignoring the higher-order terms on the right-hand side; then, using this estimate, the higher-order terms are calculated, and a new estimate of h_{lm} is obtained (see also Wieczorek et al., 2013). The second step is iterated until the relief converges to a stable solution. It is important to note that these models do not assume the crust to be isostatically compensated; such a hypothesis could be tested for a given model. Example crustal thickness models that were obtained using this procedure are discussed in the succeeding text, along with the major modeling assumptions that are specific to each body.

Crustal thickness models for Venus and Mars are presented in Figure 12. For the Venusian model, a mean crustal thickness of 35 km was assumed, the potential and topography coefficients were truncated beyond degree 60, and densities of 2900 and 3330 kg m^{-3} were used for the crust and mantle, respectively. The inclusion of finite-amplitude corrections for Venus affects the obtained crustal thicknesses by only a few kilometers. (For alternative models, see Orth and Solomatov, 2012; James et al., 2013.) The model for Mars is an updated version from Neumann et al. (2004) that uses the JGM95J01 gravity model. An average crustal density of 2900 kg m^{-3} was assumed for this model, and the low density of the polar caps, the higher than average densities of the Tharsis volcanoes, and the gravitational attraction resulting from the core flattening were explicitly taken into account. A mean crustal thickness of 45 km was assumed, and in downward continuing the Bouguer anomaly, a filter was constructed such that the power spectrum of the Moho relief resembled that of the surface relief.

A crustal thickness model for Mercury is presented in Figure 13. For this model, densities of 2900 and 3200 kg m^{-3} were used for the crust and mantle, respectively, and the filter w_l was chosen to possess a value of 0.5 at degree 40. Under the assumption that the minimum crustal thickness on Mercury is 5 km, the average crustal thickness is found to be 23 km. Since the spatial resolution of the gravity field is poor in the southern hemisphere, the inverted crustal structure there should be treated with caution. The crustal thickness model for the Moon in this figure is an updated version from Wieczorek et al. (2013) that uses gravity data derived from the GRAIL extended mission. Lateral variations in crustal density, which were estimated from remote sensing data, were used in calculating the gravity field for this model. A crustal porosity of 12% was assumed, a mantle density of 3220 kg m^{-3} was used, and the filter w_l was chosen to have a value of 0.5 at 80°. With an average crustal thickness of 34 km, this model possesses minimum crustal thicknesses that are less than 1 km and fits the 30 km seismic constraint (Lognonné et al., 2003) at the Apollo 12 and 14 landing sites. Neglecting the finite-amplitude terms in eqn [36] would give rise to errors as large as 20 km for the Moon (Neumann et al., 1996).

10.05.6 Admittance Modeling

In the crustal thickness modeling of the preceding section, the nonuniqueness associated with potential modeling was removed by making certain assumptions about the mean crustal thickness and the density of the crust and mantle. These and other parameters can be estimated if one instead assumes that surface topography is supported by a specific mechanism, such as lithospheric flexure or Airy compensation. Using such a model, the relationship between gravity and topography can be determined, and by comparing to the observed values, model parameters can be estimated. As is described in the following two subsections, two methods are in common use: One is based upon modeling the GTR in the space domain, whereas the other models the admittance and correlation functions in the spectral domain.

10.05.6.1 Spatial Domain

One method that has proven to be fruitful for estimating the mean crustal thickness of a planet is modeling of the GTR in the space domain. This technique was initially developed by Ockendon and Turcotte (1977) and Haxby and Turcotte (1978) for Earth, where it was shown that the isostatic geoid anomaly was approximately equal to the vertical dipole moment of density variations within the lithosphere. For the specific cases of Airy and Pratt isostasy, the ratio between the geoid and topography was found to be proportional to

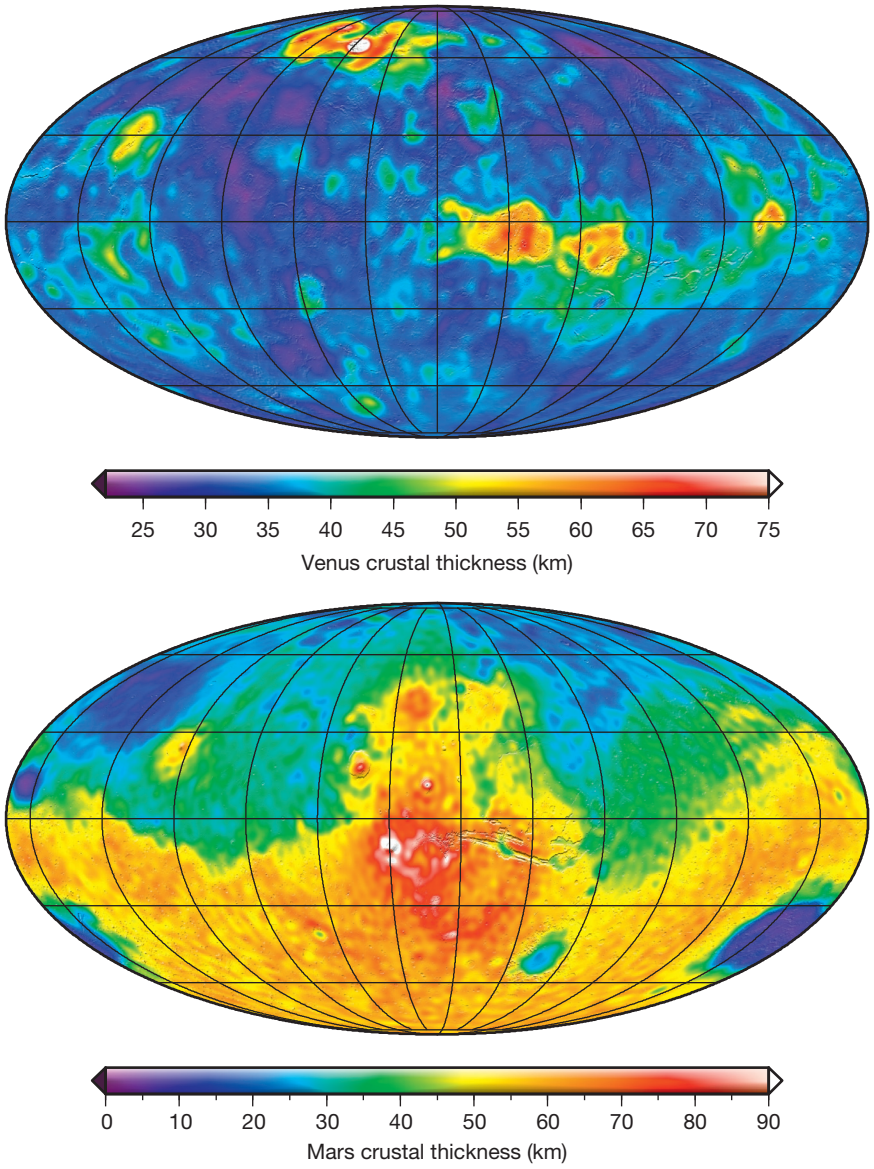

Figure 12 Crustal thickness models for Venus and Mars. Both images are in a Mollweide projection and are overlain by a gradient image derived from the surface topography. The central meridian is 60°E for Venus and 100°W for Mars.

the crustal thickness. Their method was derived using a Cartesian geometry and is strictly valid in the long-wavelength limit.

An alternative approach has been developed in spherical coordinates by Wieczorek and Phillips (1997) where it has been shown that the GTR, N/h, can be approximated by the expression

$$\frac{N}{h} = R \sum_{l=l_{\min}}^{l_{\max}} W_l Q_l \qquad [37]$$

where $l_{\min}$ and $l_{\max}$ correspond to the minimum and maximum spherical harmonic degrees that are considered, R is the mean planetary radius, Q_l is the linear transfer function between the potential and topographic coefficients, and W_l is a weighting function that is proportional to the topographic power of degree l:

$$W_l = S_{hh}(l) \Big/ \sum_{i=l_{\min}}^{l_{\max}} S_{hh}(i) \qquad [38]$$

The underlying assumption of this model is that the GTR is independent of position for a given compensation model, and this has been validated empirically for the highlands of the Moon and Mars for the case of Airy isostasy (Wieczorek and Phillips, 1997; Wieczorek and Zuber, 2004).

As the power spectra of planetary topography are 'red' (i.e., they possess more power at long wavelengths than short wavelengths), eqn [38] shows that the largest contribution to the GTR will come inevitably from the lowest degrees. As an example, approximately 80% of the GTR for the Moon is determined by degrees less than 30. Since the topography of the ancient highland crust of a planet is likely to be isostatically

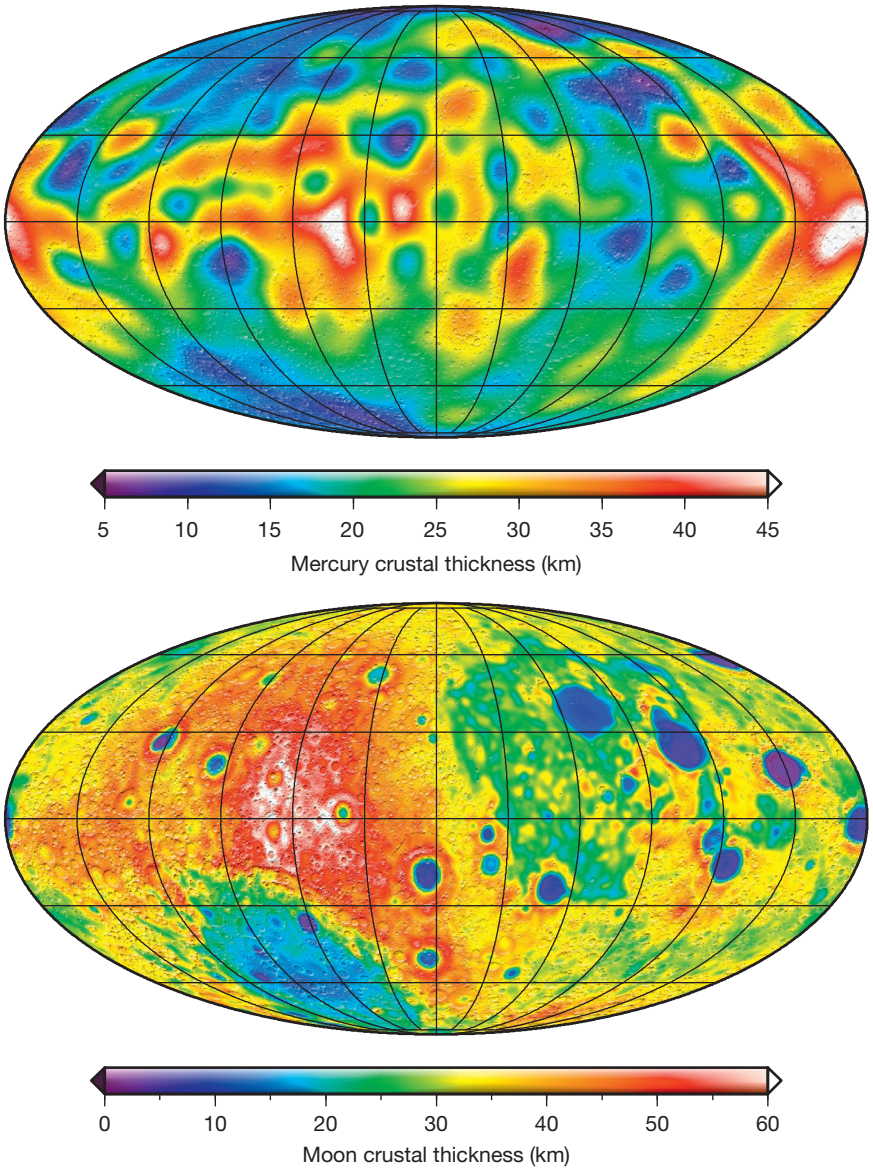

Figure 13 Crustal thickness models for Mercury and the Moon. Both images are in a Mollweide projection and are overlain by a gradient image derived from the surface topography. The central meridian is 180°E for Mercury and 90°W for the Moon.

compensated at these wavelengths, it is common to employ a model based on the condition of Airy isostasy for these regions. Assuming that the density of the crust is constant and using the condition of equal mass in crust–mantle columns, it is straightforward to show using eqn [35] that the transfer function between the potential and topographic coefficients is

$$Q_l = \frac{C_{lm}}{h_{lm}} = \frac{4\pi\rho_c R^2}{M(2l+1)}\left[1 - \left(\frac{R-T_c}{R}\right)^l\right] \qquad [39]$$

where ρ_c is the density of the crust and T_c is its mean thickness.

In practice, the GTR is determined by fitting the observations to a straight line within a region that is believed to be consistent with the employed model. By utilizing a plot of the predicted GTR versus T_c (obtained from eqns [37] to [39]), the crustal thickness can then be estimated for a given value of ρ_c. Nevertheless, as the GTR is influenced strongly by the longest wavelength components of the gravity and topography, several aspects need to be considered carefully when performing such an analysis.

It is first necessary to ensure that the entire signal of the geoid and topography are governed by the same compensation model. This can never be entirely satisfied, but certain anomalous long-wavelength features can sometimes be identified and removed. For instance, most planets and satellites possess significant rotational and/or tidal contributions to their degree-2 shape, and these signatures can be minimized by setting these coefficients to zero. For Mars, in addition to the degree-2 rotational signature, the longest wavelength components have been affected by the load and flexural response associated with the Tharsis province (see Phillips et al., 2001; Wieczorek and Zuber, 2004; Zuber and Smith, 1997).

Furthermore, as the degree-1 potential terms are zero when the gravitational field is referenced to the body's center of mass, any degree-1 topography that exists may need to be treated separately. Finally, as the GTR is determined largely by the longest wavelength components of the geoid and topography, it is necessary that the region of interest be sufficiently large when regressing the geoid and topography data.

10.05.6.2 Spectral Domain

Two major shortcomings associated with modeling the GTR are that only a single wavelength-independent parameter is used and the observed value could be biased by long-wavelength features that are unrelated to the assumed compensation model (such as lateral density anomalies in the mantle). An alternative modeling approach that largely bypasses these concerns is to model the relationship between the gravity and topography for a certain region in the spectral domain. As wavelength-dependent admittance and correlation functions are obtained, it is in principle possible to invert for several model parameters. The major shortcoming of this approach is that low spectral resolutions of planetary datasets can be particularly limiting when performing localized spectral analyses, as described in the following section. In this section, the basic concepts involved with global spectral analyses are described.

Let us presume that the potential and topography coefficients are related via an equation of the form

$$C_{lm} = Q_{lm} h_{lm} + I_{lm} \qquad [40]$$

where Q_{lm} is a linear nonisotropic transfer function and I_{lm} is that portion of the potential not described by the model. For simplicity, it will be assumed that I_{lm} is zero (though this assumption will be relaxed later) and that the topography is noise-free. Even though the aforementioned relationship is inherently nonisotropic, it is often useful to work with the power and cross power spectra of the gravitational field and topography (S_{hh}, S_{gg}, and S_{hg}), which only depend upon spherical harmonic degree l. The goal is to fit these three functions to those obtained from an appropriate model. In order to remove the model dependence of certain nuisance parameters, it is convenient to work with ratios of these three cross power spectra. Although several such ratios involving powers of these are possible, only two will be independent, and it is traditional to use the admittance and correlation spectra as defined previously by eqns [28] and [46]. If a model describing a planet's gravity and topography is to be considered successful, then it must satisfy both of these functions. If one or both of these functions cannot be fit for a given degree, then this is a clear indication that either the model assumptions are inappropriate for the region being investigated or the input datasets are not sufficiently accurate.

If one treats the lithosphere of a planet as a thin elastic spherical shell overlying a fluid interior (see Kraus, 1967), then a simple relationship exists in the spectral domain between the load on the lithosphere and its deflection (see Banerdt, 1986; Beuthe, 2008; Turcotte et al., 1981; Willemann and Turcotte, 1981). If loading at only a single interface is considered (either at or below the surface), then the transfer function in eqn [40] is isotropic (i.e., independent of m). For this situation, expressions for the admittance and correlation functions can be written schematically as

$$Z(l) = f(\rho_c, \rho_m, v, E, T_e, T_c, z, g, R) \qquad [41]$$

$$\gamma(l) = 1 \quad \text{or} \quad -1 \qquad [42]$$

where f denotes a functional dependence on the enclosed parameters. In particular, the admittance function depends explicitly on the crustal and mantle density, Poisson's ratio v, Young's modulus E, the elastic thickness T_e, the crustal thickness, the depth of the load z, the magnitude of the gravitational acceleration g, and the radius of the planet. For an isotropic transfer function Q_l, it is trivial to show that the degree correlation function (in the absence of noise) is equal to either $+1$ or -1, according to the sign of Q_l. This model has been amended by McGovern et al. (2002), Belleguic et al. (2005), and Grott and Wieczorek (2012) to include in-phase loads applied to and below the surface when the two are related linearly by a degree-independent constant. Such models would include an additional parameter $\mathcal{L}$, which is a function of the relative magnitudes of the surface and subsurface loads. Geologic situations where surface and subsurface loads might be perfectly correlated include isolated volcanoes and impact basins.

An alternative loading model that includes loads applied to and below the surface was developed by Forsyth (1985) in the Cartesian domain (see also Banks et al., 2001). In contrast to models that take the applied loads to be perfectly in phase, it was assumed that the phase differences of the applied surface and subsurface loads were random. Such an assumption might be expected to be reasonable for continental cratons where several geologic processes have operated over extended periods of time (such as erosion, sedimentation, and magmatism). In contrast to eqn [42], this model possesses a wavelength-dependent correlation function.

A general model that allows for an arbitrary phase relationship between the surface and subsurface loads has been developed by the author in spherical coordinates and can be schematically described by the following equations:

$$Z(l) = f(\rho_c, \rho_m, v, E, T_e, T_c, z, \mathcal{L}, \alpha_l, g, R) \qquad [43]$$

$$\gamma(l) = f'(\rho_c, \rho_m, v, E, T_e, T_c, z, \mathcal{L}, \alpha_l, g, R) \qquad [44]$$

where both f and f' represent generic functional dependencies. The phase relationship of the two loads is described by an additional parameter α that can possess values between 1 and -1 for correlated and anticorrelated loads, respectively. The expectation of α is given by the expression

$$\alpha_l = \frac{\sum_{m=-l}^{l} \langle \cos \Delta_{lm} \rangle}{(2l+1)} \qquad [45]$$

where Δ_{lm} denotes the phase difference between the two loads and $\langle \cdots \rangle$ is the expectation operator. For random phases, α is zero, and the model degenerates to that of Forsyth (1985). When the loads are perfectly in or out of phase by 0° or 180°, $\alpha = \pm 1$ and the model is analogous to that of McGovern et al. (2002) and Belleguic et al. (2005). A similar model was developed contemporaneously by Kirby and Swain (2009) in Cartesian geometry using a somewhat different approach and then later by Audet (2013) in spherical harmonics.

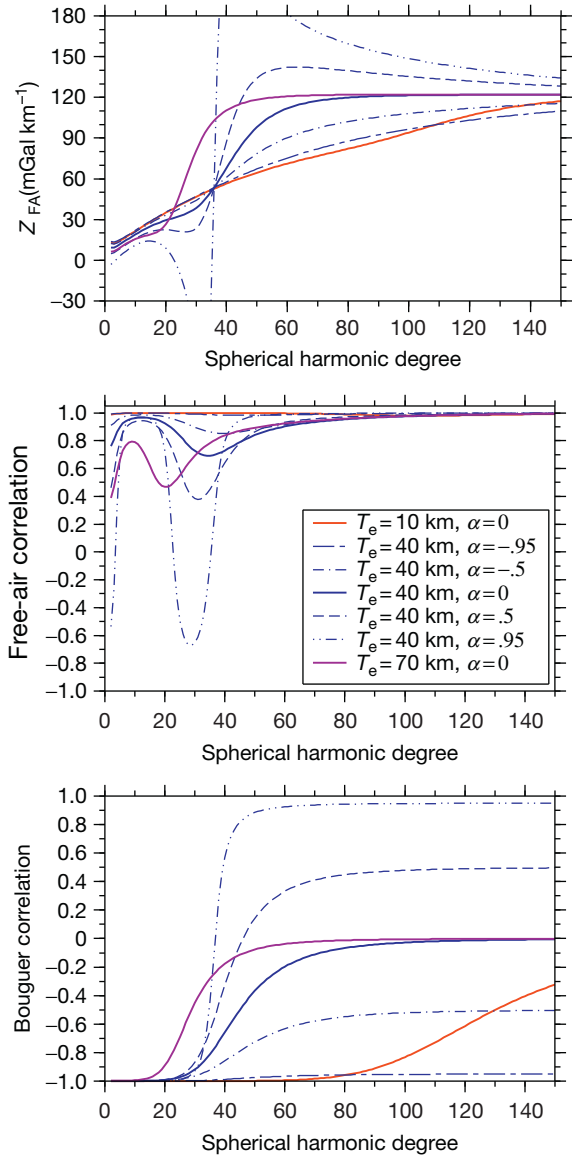

Figure 14 (Top) Free-air admittance, (middle) free-air correlation, and (bottom) Bouguer correlation, for a flexure model with equal magnitudes of applied surface and subsurface loads. Model parameters correspond to the planet Mars, with $T_c = z = 50$ km, $\rho_c = 2900$ kg m^{-3}, $\rho_m = 3500$ kg m^{-3}, and $E = 10^{11}$ Pa. The solid lines correspond to the case where the applied surface and subsurface loads have random phases (i.e., $\alpha = 0$), and the dashed lines correspond to the case where these loads are partially correlated.

Examples of the predicted free-air admittance and correlation functions are shown in Figure 14 for several values of the elastic thickness and phase parameter α. These models were generated using parameters typical for the planet Mars, and the magnitudes of the applied surface and subsurface loads were chosen to be equal. As is seen, these curves are strong functions of both the elastic thickness and α, and by considering both the admittance and correlation, it may be possible to separate the effects of the two. The free-air correlation function possesses low values over a restrictive range of wavelengths that is diagnostic of the elastic thickness. Furthermore, the free-air correlation function is seen to approach unity at high degrees ($l \gtrsim 100$). In practice, if a decline of the free-air correlation is observed with increasing degree, this is usually a good indicator of a loss of fidelity with the employed gravitational model. The predicted Bouguer correlation function is also shown for the same model parameters, and this shows a behavior similar to that predicted by the model of Forsyth (1985). It is noted that the Bouguer correlation asymptotically approaches the value of α with increasing degree. Whereas the Bouguer correlation is useful for interpretive purposes, its use is not advocated here because the Bouguer gravitational anomaly depends critically upon the value chosen for the crustal density, and this is in general not known a priori.

The preceding discussion assumed explicitly that the unmodeled gravitational signal I_{lm} in eqn [40] was identically zero. As mentioned in **Section 10.05.2.2**, if I_{lm} and the topography are uncorrelated, the expectation of the admittance will not be affected by the presence of such a signal. However, the expectation of the gravitational power spectrum will be biased upward by an additive constant S_{II}, and this will tend to bias the correlation function downward. In particular, the observed correlation function in the presence of noise is equal to

$$\gamma^{obs}(l) = \frac{\gamma(l)}{\sqrt{1 + S_{II}(l)/S_{gg}(l)}} \qquad [46]$$

where γ is the noise-free value.

Fortunately, any theoretical loading model can be easily modified to incorporate an unmodeled signal I_{lm} that is uncorrelated with the topography. It would be a simple matter to include S_{II} as an inversion parameter in a generic loading model such as eqn [44], though it is noted that this has not yet been attempted in the literature. While I_{lm} is commonly assumed to be gravitational measurement noise, this need not be the case. As described by McKenzie (2003), massive erosion or sedimentation of a lithosphere possessing surface and subsurface loads could give rise to a final state where the surface is perfectly flat but where gravitational anomalies are present. If this final state were taken as the initial condition of a *subsequent* loading event, then the initial gravitational signature (which is unrelated to the second loading model) would be expected to be uncorrelated with the subsequently generated topography.

Finally, it is important to reemphasize that if a given model of lithospheric loading is an accurate description of reality, it must fit both the admittance and coherence functions. If this cannot be done, then either the model or data must be inaccurate. Unfortunately, the vast majority of published investigations that use Forsyth-like loading models employ only the admittance or coherence function. The values of inverted parameters from such studies, while perhaps correct, need confirmation by analysis of the other function. Notable exceptions include the papers by Forsyth and coworkers (Bechtel et al., 1990, 1987; Ebinger et al., 1989; Forsyth, 1985; Pérez-Gussinyé et al., 2004; Phillips, 1994; Zuber et al., 1989). Similarly, many published investigations that employ a loading model with only surface or subsurface loads also ignore the correlation function, even though such models explicitly require this to be ± 1 when I_{lm} is zero.

10.05.7 Localized Spectral Analysis

The spherical harmonic functions represent a global basis, and the power spectrum as defined by eqn [9] is necessarily representative of the global properties of the function. In geophysics, however, it is reasonable to suspect that the spectral properties of the gravity and topography will vary as a function of position. For example, the elastic thickness may differ among geologic provinces as a result of their unique histories. Alternatively, it might arise that the data are known only locally and that one would like to estimate the power spectrum based exclusively upon these data. In this section, two methods are discussed that address these issues: One uses orthogonal windowing functions to form a multitaper spectral estimate, and the other uses spherical wavelets.

10.05.7.1 Multitaper Spectral Analysis

One way of obtaining localized estimates of a function's power spectrum is to first multiply the data by a localizing window (commonly referred to as a data taper) and then expand this windowed function in spherical harmonics (for a detailed discussion in the Cartesian domain, see Percival and Walden, 1993). However, as a result of the windowing procedure, the resultant power spectrum will differ from the true value. For the case where the input field is stationary and the spherical harmonic coefficients are governed by a zero-mean stochastic process, it can be shown that the expectation of the windowed power spectrum is related to the global spectrum by the following relation (Wieczorek and Simons, 2005, 2007):

$$\langle S_{\Phi\Gamma}(l)\rangle = \sum_{j=0}^{L} S_{hh}(j) \sum_{i=|l-j|}^{l+j} S_{fg}(i)\left(C^{l0}_{i0j0}\right)^2 \qquad [47]$$

Here, h represents an arbitrary window bandlimited to degree L, Φ, and Γ are the windowed fields hf and hg, respectively, and the last symbol in parentheses is a Clebsch–Gordan coefficient (these are related to the Wigner $3-j$ symbols and are proportional to the integral of three Legendre functions; see Varshalovich et al., 1988). The expectation of the windowed power spectrum $S_{\Phi\Gamma}$ is seen to be related to the global spectrum by a smoothing operation reminiscent of a convolution.

For a localized spectral analysis, the question arises naturally as to what form the localizing window should take. In order to spatially localize the data, it is clear that the amplitude of the window (or its power) should be near zero outside the region of interest. Furthermore, as a result of the convolution-like relationship between the global and windowed spectra, the bandwidth L of the window should be as small as possible in order to limit this spectral smoothing. Slepian and coworkers (see Slepian, 1983) posed and solved this problem in Cartesian geometry by finding those windows whose power was concentrated optimally in a specified region. Using this same criterion, Wieczorek and Simons (2005) and Simons et al. (2006) solved for those bandlimited windows on the sphere that are concentrated optimally within a spherical cap. The case of arbitrary regions was treated by Simons et al. (2006), and the case where data are absent at the poles (the polar gap problem) was treated by Simons and Dahlen (2006).

This optimization problem reduces to a simple eigenvalue equation whose solution yields a family of $(L+1)^2$ orthogonal data tapers; the quality of the concentration is given by the corresponding eigenvalue, λ, which is the fractional power of the function within the region of interest. As an example, for a concentration region specified by a spherical cap with an angular radius of 30°, as shown in **Figure 15**, 34 windows exist with a bandwidth $L=29$ that concentrate more than 99% of their power within the region of interest.

Though it is common to use a single localization window when performing a localized spectral analysis, the use of multiple tapers, as pioneered by Thomson (1982) in the Cartesian domain, can be highly advantageous. The multitaper estimate is defined as the weighted sum of spectra obtained from using K well-localized orthogonal tapers:

$$S^{(mt)}_{\Phi\Phi}(l) = \sum_{k=1}^{K} a_k S^{(k)}_{\Phi\Phi}(l) \qquad [48]$$

The values of the weights are usually assigned to be either $1/K$ or proportional to $1/\lambda_k$, but these can be chosen to also minimize the variance of the estimate (Wieczorek and Simons, 2007). The benefits of using a multitaper estimate are several fold. First, the cumulative energy of orthogonal tapers will be nearly constant across the region of interest, whereas the energy of any single window will nonuniformly cover the concentration region. Because of this, a multitaper average will be more representative of the data than that of a single taper. Second, while it is generally not possible to obtain the expectation of the localized spectrum since there is usually only a single field available for analysis, the spectral estimates obtained from orthogonal tapers are nearly uncorrelated, and their average can be considered as an approximation of the expectation. Finally, by using multiple tapers, it is possible to make an estimate of the uncertainty associated with a given spectral estimate; this is expected to decrease as approximately $1/\sqrt{K}$ (Wieczorek and Simons, 2005, 2007).

In performing a localized spectral analysis, there are several factors that need to be considered. First, it is noted that if the fields f and g of eqn [47] are known to a maximum spherical harmonic degree of L_{fg}, then only the first $L_{fg}-L$ windowed spectral estimates are reliable. Second, those localized spectral estimates with degrees less than L are heavily biased and possess relatively large uncertainties, making these of little use for geophysical analysis. Third, while a multitaper spectral analysis is generally preferable to using a single taper, the aforementioned two concerns present serious limitations when working with the relatively low-resolution gravity fields of Mercury, Venus, and Mars. Depending on the size of the concentration region, it may be infeasible to use the larger bandwidths that are required for obtaining several well-concentrated tapers.

Finally, when comparing model results to observations, it is emphasized that the two must be windowed in the same manner (e.g., Pérez-Gussinyé et al., 2004). If the analysis is performed by generating forward models of the gravity field using the known topography, then it is necessary to localize these functions in the same manner as the data. Alternatively, if no explicit expression exists for Q_{lm} (as in the model of Forsyth (1985) and that presented in **Section 10.05.6.2**, both of which are statistical in nature), then it is necessary to window the

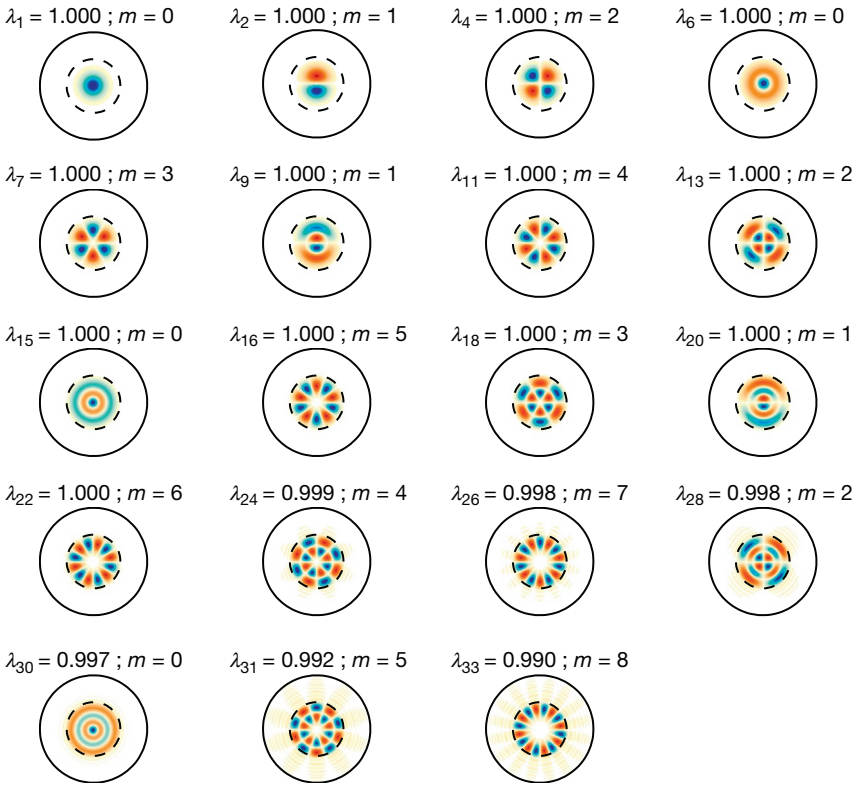

Figure 15 Spatial rendition of those functions that are near-perfectly concentrated within a spherical cap of angular radius 30° with a spherical harmonic bandwidth $L = 29$. The dotted circle corresponds to the localization region, and the blue and red colors correspond to negative and positive values, respectively. For these parameters, the total number of functions with $\lambda > 0.99$ is equal to 34. Each nonzonal function has a twin that is rotated by 90°/m. Image reprinted from Wieczorek MA and Simons FJ (2007) Minimum-variance multitaper spectral estimation on the sphere. *Journal of Fourier Analysis and Applications* 13: 665–692, http://dx.doi.org/10.1007/s00041-006-6904-1 with permission from Springer Science and Business Media.

predicted (cross) power spectra using eqn [47] before calculating the theoretical admittance and correlation functions.

10.05.7.2 Wavelet Analysis

An alternative approach of performing a localized spectral analysis is to use spherical wavelets. A wavelet analysis differs from a multitaper analysis in that (1) the function is multiplied by a wavelet of a given size and integrated over all space, as opposed to being multiplied and then expanded in spherical harmonics, and (2) the wavelet scalogram (the analog of the power spectrum) is a function of the wavelet scale (i.e., size) and not spherical harmonic degree. Whereas the multitaper spectral analysis approach is best when the function is known to be locally stationary within the analysis region, wavelet analyses are better suited to truly nonstationary processes.

The wavelet transform for real functions is defined as the inner product of a function f with a wavelet ψ of scale s centered at position $\hat{\mathbf{r}}$ and with angular orientation γ about this axis:

$$\tilde{f}(s, \hat{\mathbf{r}}, \gamma) = \int_{\Omega} f(\theta', \phi') \psi_{s,\hat{\mathbf{r}},\gamma}(\theta', \phi') \mathrm{d}\Omega' \qquad [49]$$

The wavelet transform can be defined either to be continuous in scale s or to be composed of discreet scales. By expressing both f and ψ in spherical harmonics,

$$\tilde{f}(s, \hat{\mathbf{r}}, \gamma) = 4\pi \sum_{l=0}^{L} \sum_{m=-l}^{l} f_{lm} \psi_{lm}(s, \hat{\mathbf{r}}, \gamma) \qquad [50]$$

where L is the smaller of the spherical harmonic bandwidth of f and ψ (the product is zero beyond the bandwidth of either function). If the wavelets are zonal functions, the wavelet transform is

$$\tilde{f}(s, \hat{\mathbf{r}}) = 4\pi \sum_{l=0}^{L} \sum_{m=-l}^{l} f_{lm} \Psi_l(s) \sqrt{\frac{1}{2l+1}} Y_{lm}(\theta, \phi) \qquad [51]$$

where Ψ_l are the spherical harmonic coefficients of the zonal wavelet centered at the north pole. For zonal wavelets, the wavelet transform is equivalent to the spatial convolution of f and ψ. The wavelet transform can be calculated rapidly everywhere using fast Fourier transform techniques and Wigner rotation matrices (Wandelt and Gòrski, 2001).

The wavelet cross scalogram of two real functions f and g is defined as

$$P_{fg}(s, \hat{\mathbf{r}}, \gamma) = \tilde{f}(s, \hat{\mathbf{r}}, \gamma) \tilde{g}(s, \hat{\mathbf{r}}, \gamma) \qquad [52]$$

If it is assumed that the two functions f and g are stochastic stationary processes, it can be shown that the expectation of this expression is related to the power spectrum of the wavelet and the cross power spectrum of f and g by

$$\langle P_{fg}(s)\rangle = (4\pi)^2 \sum_{l=0}^{L} \frac{S_{fg}(l) S_{\Psi_s \Psi_s}(l)}{2l+1} \quad [53]$$

where $S_{\Psi_s \Psi_s}$ is the power spectrum of the wavelet of scale s. This fundamental relation is analogous to eqn [47] as used in localized spectral analyses and quantifies how the power spectrum of the data is modified by the window spectrum when forming the wavelet cross scalogram.

In general, wavelets should have a zero mean, they should be localized in space in order to study nonstationary processes, and they should be localized in the spectral domain in order to best extract the frequency content of the signal (cf. eqn [53]). A multitude of wavelet families have been constructed, including those that are zonal (Chambodut et al., 2005; Fengler et al., 2007; Freeden and Windheuser, 1997; Guilloux et al., 2009; Holschneider et al., 2003; Holschneider and Iglewska-Nowak, 2007; Li, 1999; Michel and Wolf, 2008; Panet et al., 2011; Schmidt et al., 2007; Wiaux et al., 2007) and directional (Audet, 2011, 2013; McEwen et al., 2007). Once the family of wavelets has been constructed for each scale s, it is straightforward to construct the wavelet transform. Nevertheless, the best manner to construct a family of wavelets on the sphere is not trivial. The biggest problems consist of how to discretize the wavelets as a function of scale, how to most optimally represent the data by the smallest number of wavelet coefficients as possible, and how to minimize correlations between the wavelet coefficients (e.g., Freeden and Windheuser, 1997; Narcowich and Ward, 1996). A perhaps more daunting problem is deciphering the spherical wavelet literature itself: many of these papers are highly mathematical, the notation is highly variable among authors, and the papers span a wide range of disciplines and journals.

10.05.8 Summary of Major Results

10.05.8.1 Earth

The gravity and topography of Earth have been used extensively to decipher the rheological properties of the crust and upper mantle. The literature is voluminous, and the reader is referred to several reviews in volume 8 of this series, Watts (2001), and the references in the papers cited in the succeeding text. Here, only a few subjects will be touched upon that bear relevance to investigations of Venus, Mars, Mercury, and the Moon. These include modeling of the elastic thickness of the oceanic and continental lithosphere, inelastic flexural modeling, and the modeling of dynamic topography and geoid signatures associated with mantle convection.

Flexural modeling of the oceanic lithosphere is relatively simple in that loading is primarily a result of the construction of isolated shield volcanoes. Elastic thickness estimates have been obtained by modeling the topographic and gravity signatures of these features, and it is widely accepted that the elastic thickness is dependent primarily upon the age of the plate at the time of loading, with T_e being less than about 45 km (for a review, see Watts, 2001). In particular, a plot of the elastic thickness versus age of the lithosphere at the time of loading resembles the time dependence of the depth to an isotherm (~300–600 °C) predicted from a plate cooling model (see Watts and Zhong, 2000). This suggests that the flexural signature has been 'frozen' into the lithosphere as it cooled and that subsequent long-term viscoelastic relaxation has been relatively unimportant. Nevertheless, a description of the initial short-term subsidence of the lithosphere (i.e., the first few 10 s of ka) requires the use of a viscoelastic model, and given the relatively restricted age range of oceanic lithosphere (<200 Ma), it is difficult to discern if viscoelastic relaxation would be important at longer timescales. It is important to note that most flexural modeling of features on the other terrestrial planets has been for loads that were emplaced on the lithosphere over a billion years ago.

Investigations of the continental elastic thickness have been more contentious. Part of the difficulty arises because the importance of subsurface loading, and the phase relationship of the surface and subsurface loads, is not known a priori (see **Section 10.05.6.2**). A loading model was developed by Forsyth (1985) that took into account both surface loading and subsurface loading under the assumption that the two were uncorrelated, and application of this method has yielded elastic thicknesses in the broad range from about 5 to 150 km (Bechtel et al., 1990, 1987; Ebinger et al., 1989; Forsyth, 1985; Kirby and Swain, 2009; Pérez-Gussinyé et al., 2004, 2009; Zuber et al., 1989). There is some controversy as to whether the values greater than ~25 km are reliable (compare McKenzie, 2003 with Watts and Burov, 2003), but this debate will not be settled definitively until investigators fit both the admittance and correlation functions simultaneously while taking into account partially correlated loads and unmodeled gravitational signals (see **Section 10.05.6.2**). Furthermore, some studies that have inverted for the elastic thickness using multitaper spectral analysis and wavelet techniques have done so using a methodology that is not entirely correct. In particular, as both windowing and wavelet approaches return a modified form of the power spectrum (cf. eqns [47] and [53]), it is necessary to compare these modified spectra with suitably modified theoretical spectra, which is not always done. Regardless, these methods have convincingly shown that the elastic thickness of some continental regions is not always isostropic (e.g., Kirby and Swain, 2006; Simons et al., 2003, 2000), which is an assumption common to most studies.

The majority of investigations that model lithospheric flexure assume that the lithosphere is perfectly elastic, but elastic stresses are often predicted to be in excess of the strength of geologic materials. A simple modification to the elastic flexure equation that takes this into account is to replace the elastic bending moment–curvature relationship with one that is based upon an elastic–perfectly plastic (EP) model of the lithosphere's yield strength (e.g., Burov and Diament, 1995; Mueller and Phillips, 1995). In particular, the strength of the upper crust is limited by brittle failure, and stresses in the lower crust and mantle are limited by their ductile strength for a specified strain rate. Predicted flexural profiles are time-invariant and can sometimes differ significantly from those of the perfectly elastic model. As the ductile strength is temperature-dependent, these results are sensitive to the assumed lithospheric temperature gradient.

A more realistic model of lithospheric deformation uses a time-dependent elastoviscoplastic (EVP) formulation (e.g., Albert and Phillips, 2000; Albert et al., 2000; Brown and

Phillips, 2000). The main advantage of these models is that the strain rates are calculated explicitly, as opposed to assumed as in the EP models. Though the best-fit EP and EVP flexural profiles can be quite similar, it is not clear a priori how one should estimate the characteristic strain rate that is required for the EP model without running a full EVP simulation (Albert et al., 2000). The EVP models show that significant decoupling of stresses may occur between the crust and mantle if the lower crust is sufficiently weak (e.g., Brown and Phillips, 2000). When this occurs, the effective elastic thickness decreases; the exact value is highly dependent upon the crustal thickness, load magnitude, and assumed rheology of the crust and mantle. In contrast, when the lower crust is strong, the maximum achievable effective elastic thicknesses are consistent with the depth of an ~700 °C isotherm obtained from a lithospheric cooling model. Flexural modeling of a volcano growing on a cooling lithosphere shows that the effective elastic thickness is 'frozen' into the lithosphere shortly after volcanic construction is complete (Albert and Phillips, 2000).

Finally, in addition to near-surface crustal thickness and density variations, significant gravity and topography signatures can be generated by dynamic processes in the mantle, such as beneath hot spots and subduction zones. Though there are few, if any, convincing examples of plate subduction on the other terrestrial planets, hot spots similar to Earth are believed to exist on both Venus and Mars. Dynamic modeling of plumes shows that the major variable controlling the surface gravity and topography signatures is the depth dependence of the mantle viscosity. In the absence of a shallow low-viscosity asthenosphere, convective stresses generated at depth are coupled efficiently to the surface, generating large signals and large corresponding effective depths of compensation. However, the inclusion of a shallow low-viscosity zone can reduce these signatures significantly, giving rise to shallower apparent depths of compensation (e.g., Ceuleneer et al., 1988; Robinson and Parsons, 1988). Joint inversions utilizing mantle density anomalies from seismic tomography and estimates for the dynamic topography signal imply the existence of a low-viscosity zone somewhere in the upper mantle and a gradual increase in viscosity with depth by an order of magnitude in the lower mantle (e.g., Panasyuk and Hager, 2000).

10.05.8.2 Venus

Our knowledge of Venus has dramatically improved since the acquisition of gravity, topography, and SAR imagery by the Magellan mission between 1990 and 1994. The size and bulk density of Venus were known beforehand to be similar to that of Earth, but this planet was found to differ dramatically in that it lacks any clear sign of plate tectonics. A major unanswered question is how this planet loses its internal heat and whether or not this process is episodic or uniform in time. Geophysical analyses have been used to constrain the crustal and elastic thickness, and the latter has been used to place constraints on the temperature gradient within the lithosphere. Reviews concerning the geophysics of this planet can be found in Phillips et al. (1997), Grimm and Hess (1997), Schubert et al. (1997), and Nimmo and McKenzie (1998).

The crustal plateaus of Venus have generally low-amplitude gravitational and topographic signatures within their interiors and low GTRs. With the exception of Ishtar Terra, these regions are potential candidates for being isostatically compensated. Assuming that the surface topography is compensated at a single interface, Grimm (1994) obtained best-fit apparent depths of compensation between 20 and 50 km for Alpha, Tellus, Ovda, and Thetis Regiones. These values are plausibly interpreted as representing the depth of the crust–mantle interface. Analyses of GTRs by Kucinskas and Turcotte (1994), Moore and Schubert (1997), and James et al. (2013) obtained zero-elevation crustal thicknesses between about 40 and 80 km for Alpha, Ovda, Tellus, and Thetis Regiones. If any portion of the geoid and topography were to result from Pratt or thermal compensation, the obtained crustal thicknesses would represent an upper bound. A spectral admittance study by Phillips et al. (1997) obtained a slightly thinner crustal thickness of 38 ± 9 km for the region of Atla Regio (see also Phillips, 1994).

In contrast to the majority of the highland plateaus, large apparent depths of compensation and GTRs have been found for the volcanic rises (Kucinskas and Turcotte, 1994; Moore and Schubert, 1995, 1997; Smrekar, 1994) and Ishtar Terra (Grimm and Phillips, 1991; Hansen and Phillips, 1995; Moore and Schubert, 1997). These values are not consistent with compensation occurring solely by crustal thickening, but require some form of dynamic support from the mantle via stresses induced by ascending mantle plumes (e.g., Vezolainen et al., 2004) or substantial thinning of a thick (~300–600 km) thermal lithosphere (Kucinskas and Turcotte, 1994; Moore and Schubert, 1995, 1997; Orth and Solomatov, 2011). If a low-viscosity asthenosphere were present at shallow mantle depths, as is the case of Earth, the predicted GTRs and apparent depths of compensation resulting from dynamic support would be considerably smaller than measured as a result of the decoupling of stress between the lithosphere and mantle (e.g., Kiefer and Hager, 1991; Kiefer et al., 1986). This seems to imply that in contrast to Earth, Venus lacks a low-viscosity zone (Huang et al., 2013; Pauer et al., 2006), which is most likely a result of a volatile-poor mantle. Modeling by Pauer et al. (2006) suggests that the viscosity of the Venusian mantle could increase by a factor of about 10–80 from the upper to lower mantle, similar to that of Earth. A strong coupling of stress between the lithosphere and convecting mantle is the likely cause of the high spectral correlation between gravity and topography for the lowest spherical harmonic degrees of Venus (contrast **Figures 2** and **4**).

An additional constraint concerning the thickness of the Venusian crust is related to its compositional buoyancy. If the crust were basaltic in composition, this material would undergo a phase transition at high pressure to the more dense mineral assemblage of eclogite (e.g., Grimm and Hess, 1997). This material could potentially delaminate from the base of the crust as a result of its high density, and the depth of this phase transition might thus constrain the maximum achievable crustal thickness. For a MORB composition, the eclogite phase transition is predicted to occur at depths of ~70–120 km (see Ghent et al., 2004) for linear temperature gradients of 5 and 15 K km^{-1}, respectively.

The crustal thickness model presented in **Figure 12** has thicknesses near 70 km only in the highland plateaus of Ishtar Terra and Ovda and Thetis Regiones, suggesting that crustal delamination could have occurred in these regions. The

highland crust is almost exactly twice as thick as the lowland crust, which could potentially arise by the obduction of one plate over another. In contrast to Mercury, Mars, and the Moon, no large impact basins are found on this planet as a result of the relatively young age of its surface (~240 Ma; Le Feuvre and Wieczorek, 2011). This crustal thickness model assumed an average thickness of 35 km and did not consider density anomalies beneath the crust–mantle interface. An alternative model was developed by Orth and Solomatov (2012) who assumed that variations in lithospheric thickness were isostatically compensated and that the remaining signal was a result of isostatic variations in crustal thickness. James et al. (2013), in contrast, constructed a global crustal thickness model by assuming that the observed surface topography and gravitational potential were a result of isostatically compensated crust and dynamic relief arising from mantle density anomalies below an elastic lid.

Elastic thickness estimates have been obtained for a variety of features based exclusively on topographic profiles that are indicative of flexure. The benefit of using topography alone is that small features can be investigated that are not resolved in the current gravity model. Elastic thicknesses of 11–25 km have been obtained by modeling the Freyja Montes foredeep (Sandwell and Schubert, 1992; Solomon and Head, 1990) and ~10–60 km for potential flexural bulges outboard of coronae (Sandwell and Schubert, 1992). Additional features modeled by Johnson and Sandwell (1994) yield elastic thicknesses of 10–40 km, and potential subduction-related sites possess a range of 6–45 km (Schubert and Sandwell, 1995). Predicted stresses are largest where the plate curvature is greatest, and faulting is generally visible in the Magellan SAR imagery at these locations. Modeling by Barnett et al. (2002) yielded best-fit elastic thicknesses that are consistent with the aforementioned studies. Modeling the location of concentric faulting around Nyx Mons (a volcano in Bell Regio) implies a best-fit elastic thickness of ~50 km (Rogers and Zuber, 1998). It is important to note that the assumption of a perfectly elastic rheology may be grossly inappropriate for some features. For instance, the magnitude of the flexure-induced bulge south of Artemis Chasma implies that significant yielding has occurred within the lithosphere, and inelastic modeling by Brown and Grimm (1996) shows that a significant compressive in-plane force is required at this locale.

The elastic thickness has also been estimated for various regions of Venus through a combined analysis of gravity and topography data in the spectral domain. However, the majority of these investigations have fit only the admittance or coherence functions, but not both simultaneously (e.g., Anderson and Smrekar, 2006; Barnett et al., 2000, 2002; Hoogenboom et al., 2005, 2004; Lawrence and Phillips, 2003; McKenzie, 1994; McKenzie and Nimmo, 1997; Simons et al., 1994, 1997; Smrekar, 1994; Smrekar et al., 2003; Smrekar and Stofan, 1999). The robustness of the inverted parameter values, the fidelity of the gravity model, and the appropriateness of the loading model are all difficult to assess in these studies. One exception is that of Phillips (1994) who investigated the lithospheric properties of Atla Regio, which is believed to be an active hot spot based on its geomorphology and previously determined large apparent depths of compensation. Using the loading model of Forsyth (1985), which assumes uncorrelated surface and subsurface loads, it was shown that a single mode of compensation could not explain the entire wavelength range of the admittance and coherence functions. An inversion utilizing only the short wavelengths yielded a crustal thickness of 30 ± 13 km and an elastic thickness of 45 ± 3 km. Whereas surface loading by the volcanic constructs in this area dominates, about 10% of the load is required to be located at shallow depths within the crust. For the long-wavelength range, only the depth of the subsurface load was well constrained with a value near 150 km, and the elastic thickness was constrained only to be less than 140 km.

It is possible to place constraints on the crustal temperature gradient at the time of loading either by using the obtained elastic thicknesses or by forward modeling of inelastic flexure. The basic approach is to match the bending moment implied by the elastic model to that predicted by an inelastic rheology (McNutt, 1984). The obtained temperature gradient estimates lie in the rather broad range of 3–26 K km^{-1} (Brown and Grimm, 1996; Johnson and Sandwell, 1994; Phillips, 1994; Phillips et al., 1997; Sandwell and Schubert, 1992), but the majority of these lie on the low end, between ~4 and 10 K km^{-1}. This is considerably lower than the expected Earth-scaled temperature gradient of ~15 K km^{-1} (e.g., Phillips, 1994), especially when considering that some of these estimates were obtained where an underlying mantle plume might be expected. Though such calculations are critically dependent on the validity of the inelastic strength model, the assumed strain rate, and the depth dependence of temperature, these results seem to imply that the background heat flow of Venus is much less than would be expected by analogy to Earth. Such an interpretation is consistent with a model in which the Venusian lithosphere formed catastrophically ~500–1000 Mya and has since been cooling conductively (cf. Moresi and Solomatov, 1998; Parmetier and Hess, 1992; Turcotte, 1995). However, such a model is not required, or even preferred, by the cratering history of the Venusian plains (Hauck et al., 1998).

10.05.8.3 Mars

Following the acquisition of high-resolution gravity and topography data from the MGS and Mars Odyssey missions, a number of studies have been published bearing on the crustal and lithospheric structure of Mars. These investigations have placed constraints on the thickness of the Martian crust, the elastic thickness, and the crustal density and also imply the existence of dynamic support of topography and buried mass anomalies. Reviews concerning the gravity, topography, and crust of Mars can be found in Esposito et al. (1992), Banerdt et al. (1992), Zuber (2001), Wieczorek and Zuber (2004), Nimmo and Tanaka (2005), and Grott et al. (2013).

The average thickness of the Martian crust has been constrained by the analysis of GTRs over the ancient southern highlands. After removing the long-wavelength flexural and load signatures associated with the Tharsis province, a zero-elevation thickness of 57 ± 24 km was obtained under the assumption of Airy isostasy (Wieczorek and Zuber, 2004). This range of values is consistent with estimates based upon the viscous relaxation of topography (Nimmo and Stevenson, 2001; Zuber et al., 2000b) and geochemical mass-balance arguments, both of which require the crust to be less than ~100 km thick (see Wieczorek and Zuber, 2004). Crustal

thickness modeling further requires the mean thickness of the crust to be greater than about 25 km (Pauer and Breuer, 2008).

A global model of the crustal thickness of Mars has been constructed by Neumann et al. (2004) by assuming a mean thickness of 45 km (see **Figure 12**). If the assumption of a constant density crust is correct, the crust of the southern highlands is predicted to be thicker by about 30 km than the northern lowlands. However, if the northern lowland crust is denser than the southern highlands, as implied by the results of Belleguic et al. (2005), then the actual crustal thickness difference could be significantly less. The Tharsis province is seen to possess a relatively thick crust, indicative of prolonged volcanic construction, whereas the crust beneath the major impact basins is thinned and in some places nearly absent.

Localized spectral admittance and correlation spectra have been modeled in spherical coordinates for various regions using the techniques of Simons et al. (1997) and Wieczorek and Simons (2005). In the investigations of McGovern et al. (2002, 2004), Belleguic et al. (2005), Wieczorek (2008), Grott and Wieczorek (2012), and Beuthe et al. (2012), a thin elastic spherical shell loading model was employed that depended upon the shell's elastic thickness, the load density, the crustal density, and the ratio of the magnitudes of subsurface and surface loads, which were assumed to be in or out of phase by 0° or 180°. When the load density differs from that of the crust, the methodology of Belleguic et al. (2005) is more accurate, and their results are here emphasized.

Of all the parameters considered by Belleguic et al. (2005) when modeling the major Martian volcanoes, the load density is in general the best constrained. For the Tharsis Montes and Elysium rise, values of $\sim 3200 \pm 100\ \mathrm{kg\ m^{-3}}$ were obtained. After accounting for a few-percent porosity, this range is consistent with density estimates of the Martian meteorites, which are thought to be derived from these regions based on their young ages. Elastic thickness estimates are somewhat variable but were found to lie between about 50 and 100 km when only surface loads were considered. However, when both surface and subsurface loads were modeled, only upper and lower bounds could be specified for most regions. The crustal density was constrained only beneath the Elysium rise (which is located in the northern lowlands) and was found to be identical to the density of the superposed load. Combined modeling of GTRs and crustal thickness suggest a maximum density of about $3020\ \mathrm{kg\ m^{-3}}$ for the southern highlands, which is consistent with the value of $3000\ \mathrm{kg\ m^{-3}}$ suggested by Neumann et al. (2004) based on rock compositions at the Mars Pathfinder site. If the crustal density beneath the Elysium rise is representative of the northern lowlands, then this implies a hemispheric dichotomy in crustal composition. This result is consistent with geochemical maps obtained from the Mars Odyssey gamma-ray spectrometer that show the northern lowlands possess a higher iron concentration than the southern highlands (Taylor et al., 2006). The low elevations of the northern plains could thus be a partial result of Pratt compensation. Finally, the inclusion of less dense subsurface loads (either compositional or thermal in origin) improved the misfit between the modeled and observed admittance functions.

In the localized admittance study of Beuthe et al. (2012), two-stage loading models were employed to investigate how the elastic thickness and load density varied with time. This loading model could fit the data and models with single-stage top and bottom loading, calling into question the necessity of subsurface loading. Using similar localized admittance techniques, density and elastic thickness have been estimated at other regions on the planet. For the isolated low-relief volcano Tyrrhena Patera, Grott and Wieczorek (2012) obtained a density between 2960 and $3500\ \mathrm{kg\ m^{-3}}$, which is consistent with the Tharsis and Elysium volcanoes, and an elastic thickness that is less than 28 km. Zuber et al. (2007) and Wieczorek (2008) investigated the ice-rich south polar layered deposits and found densities close to $1250\ \mathrm{kg\ m^{-3}}$.

Elastic thickness estimates for other locales have been determined using a variety of techniques, but these generally contain a larger number of assumptions. Modeling of the geologically inferred flexural moat of the northern polar cap suggests an elastic thickness between 60 and 120 km (Johnson et al., 2000). Faults surrounding the Isidis impact basin imply elastic thicknesses between 100 and 180 km at the time of loading (Ritzer and Hauck, 2009). If the topography of the dichotomy boundary is flexural in origin, with loading in the northern plains, then elastic thicknesses of ~31–36 km are implied (Watters, 2003). Cartesian admittances were analyzed in several other studies (Hoogenboom and Smrekar, 2006; McKenzie et al., 2002; Milbury et al., 2009; Nimmo, 2002), but the validity of the loading model was not quantified by calculating theoretical correlation functions. A summary of how elastic thickness constrains Martian heat flow can be found in Grott et al. (2013).

One distinctive feature of Mars is the large geoid and topography signals associated with the Tharsis province (e.g., Phillips et al., 2001). Two possible end-member explanations for this observation are either that it is a result of voluminous extrusive lavas that are partially supported by the lithosphere or that it is a result of dynamic topography associated with an underlying plume. Viscoelastic modeling of the geoid and topography response to internal buoyant loads implies that a plume is incapable of producing the totality of the observed signals (Roberts and Zhong, 2004; Zhong, 2002). By modeling the contributions of both surface and plume signals with a method that approximates a viscoelastic response, the degree-2 and degree-3 GTRs imply that a plume can account for only ~15% and 25% of the geoid and topography signals, respectively. Using a modified approach that includes all spherical harmonic degrees, Lowry and Zhong (2003) inverted for the relative contributions of surface and internal loads and found that a plume could account only for a maximum of ~25% and 50% of the observed geoid and topography, respectively.

Finally, it is noted that buried mass anomalies can be investigated by examination of the residual gravity field after subtraction of an appropriate reference model. By modeling the gravity field of the Syrtis Major region by surface loading of an elastic shell, an unmodeled localized density anomaly was found beneath this volcanic province. The amplitude of this unmodeled anomaly is consistent with the presence of dense cumulates of an extinct magma chamber (Kiefer, 2004). Using a similar technique, buried mass anomalies have also been inferred along the portions of the dichotomy boundary (Kiefer, 2005).

10.05.8.4 Mercury

Our understanding of Mercury is currently being revolutionized by the analysis of data from the MESSENGER spacecraft.

At the time of this writing, the initial analyses have just been published, and more result will soon follow.

Mercury is somewhat similar to the Moon in that its surface records billions of years of impact cratering. One striking aspect concerning the topographic expression of the largest impact basins is that they are not as topographically distinct as those found on the Moon and Mars. Many of these basins have shallower than expected depths (Mohit et al., 2009), and others have been deformed topographically. One clear example of basin deformation that postdates the impact event is the topographic bulge in the northern portion of the Caloris basin that is higher than most of its topographic rim (Zuber et al., 2012). Together, these observations suggest some form of modification by either mantle convection or crustal viscous relaxation (Mohit et al., 2009).

The Caloris impact basin is clearly associated with a positive gravitational anomaly, similar to the mascon basins on the Moon. Few other basins have corresponding gravitational anomalies, but this could be an artifact of the low resolution of the current gravity model. Crustal thickness modeling shows that the Caloris, Budh, and Sobkou basins are associated with a thinned crust (Smith et al., 2012). However, little is known about the average thickness of the crust, which is important for understanding the bulk silicate composition of the planet. Estimates of the depths of faulting constrain the depth of the brittle–ductile transition, and when combined with an estimate of the melting temperature of the base of the crust, an average crustal thickness less than 140 km is required (Nimmo and Watters, 2004).

The lithospheric thickness of Mercury appears to have varied over time. Many regions of ancient high-standing topography do not possess any significant gravitational anomaly, indicating that they were likely in a state of isostatic compensation when they formed. In contrast, a positive gravitational anomaly is associated with a domical rise in the northern lowlands, and modeling of this feature implies that the lithosphere had an elastic thickness of 70–90 km at the time of its formation (Smith et al., 2012). As a result of Mercury's eccentric orbit and 3/2 spin–orbit resonance, the average temperature of the surface has strong variations in both latitude and longitude, with two hot 'poles' being located at 0° and 180° on the equator. These temperature variations are predicted to give rise to long-wavelength variations in the thickness of the lithosphere, with variations in the mechanical thickness approaching 80 km between ±90°N and the equatorial hot poles (Williams et al., 2011).

10.05.8.5 The Moon

Analyses of the gravitational field of the Moon have been hindered historically by the lack of direct tracking data over the lunar farside hemisphere. This problem was rectified only recently by the collection of four-way tracking data from the Kaguya (2007) mission and intersatellite range-rate measurements from the Gravity Recovery and Interior Laboratory (2011) mission. Together with altimetric data and stereo imagery collected by the LRO and Kaguya missions, it can be said that the gravity and topography of the Moon are known better in a global sense than any other terrestrial object. These data have permitted a wide range of investigations, including the mapping of crustal thickness variations, studies of giant impact basins, and the mapping of subsurface density anomalies. A comprehensive review of results predating the GRAIL, LRO, and Kaguya missions can be found in Wieczorek et al. (2006).

The observed gravity signal at short wavelengths, where lithospheric flexure is unimportant, should be almost entirely a result of relief along the surface (cf. **Figure 14**). Wieczorek et al. (2013) used this observation to estimate the bulk density of the lunar highland crust. The obtained value of 2550 kg m^{-3} was substantially lower than the expected grain density of about 2900 kg m^{-3}, and this implies the existence of about 12% porosity in the upper crust. Although the depth dependence of porosity is not well constrained, it must extend at least several kilometers below the surface and perhaps into the upper mantle. These high porosities are almost certainly a result of fractures generated by billions of years of impact cratering and are consistent with impact-induced porosities associated with small impact craters on Earth (see also Huang and Wieczorek, 2012).

A global crustal thickness model of the Moon can be constructed by assuming values for the density of the crust, the density of the mantle, and the mean crustal thickness (see **Section 10.05.5**). The density of the lunar crust can be estimated from either remote sensing data or analyses of the short-wavelength gravity field, whereas the other two free parameters can be determined iteratively by the use of two additional constraints. In practice, the mantle density and mean crustal thickness are varied in order to match the seismically determined crustal thickness and to ensure that the minimum crustal thickness is equal to a chosen value. The most recent interpretations of the Apollo seismic data imply a crustal thickness of either 30 ± 2.5 km (Lognonné et al., 2003) or 38 ± 8 (Khan and Mosegaard, 2002) in the vicinity of the Apollo 12 and 14 landing sites (see also Chenet et al., 2006). When using the constraint that the minimum crustal thickness should be close to zero, as implied by the possible excavation of mantle materials from some impact basins (Yamamoto et al., 2010), the seismic analyses imply an average crustal thickness of either 34 or 43 km (Wieczorek et al., 2013). These average thicknesses imply that the bulk abundance of alumina in the Moon is similar to that of the bulk silicate Earth.

The most notable feature of the global crustal thickness models is the dramatic thinning of the crust beneath the large impact basins. This is a natural consequence of the large quantity of material that is excavated ballistically during the impact process (e.g., Wieczorek and Phillips, 1999), and it is seen that the depth of excavation reaches several tens of kilometers beneath the largest basins. The crustal thickness is close to zero beneath both the Crisium basin on the nearside hemisphere and the Moscoviense basin on the farside hemisphere (see also Ishihara et al., 2009). When combined with the detections of dunite exposures surrounding these two basins, it is likely that these impacts excavated through the entire crust and into the underlying mantle. Despite the great size of the giant South Pole–Aitken basin on the farside, the crust is predicted to be about 20 km thick in its interior. Either the depth of excavation during this basin-forming event was atypically shallow or an impact-generated melt pool differentiated to form a low density crust (Vaughan et al., 2013). The ~1.9 km offset of the Moon's center of mass from its center of figure,

combined with the lateral variations in crustal density as implied by remote sensing data, implies that the farside crust is thicker than the nearside hemisphere by about 8 km.

The majority of the lunar impact basins are characterized by having low elevations, a large central positive free-air gravitational anomaly, a gravity low surrounding the central high, and a gravity high that outlines the basin's topographic rim. Historically, basins with central gravity highs have been referred to as *mascon* basins. The central positive gravitational anomalies are a combination of both uplift of the underlying crust–mantle interface and flexural support of surface mare basalt flows. Based on estimates of the mare basalt thicknesses, which can reach a few kilometers within the central portions of some impact basins, the crust–mantle interface has been shown to be uplifted above its pre-mare isostatic position (e.g., Hikida and Wieczorek, 2007; Neumann et al., 1996; Wieczorek and Phillips, 1999). This hypothesis is supported by the existence of mascon basins that lack evidence of mare volcanism (Konopliv et al., 1998; Zuber et al., 2013b). The surrounding annulus of negative gravity implies that this region of the lithosphere is subisostatic (Andrews-Hanna, 2013), and hydrocode simulations of the basin formation process show that this region of the lithosphere was pushed below its isostatic level during basin formation (Melosh et al., 2013). Subsequent uplift of this subisostatic lithosphere by viscous flow is responsible for uplifting the central portion of the basin above its isostatic level (Andrews-Hanna, 2013; Melosh et al., 2013).

In contrast to the largest impact basins, intermediate-sized craters have negative gravitational anomalies and generally show some form of compensation. Only about 15% of the craters in the Reindler and Arkani-Hamed (2001) study appear to be completely uncompensated or to possess excess negative gravitational anomalies due to crustal brecciation. For these intermediate-sized craters, there does not appear to be any correlation of compensation state with crater age or location.

A few studies have attempted to place constrains on the elastic thickness of the Moon using both gravity and topography data (e.g., Arkani-Hamed, 1998; Crosby and McKenzie, 2005; Sugano and Heki, 2004). Most analyses have concentrated on the mascon basins, but it is often difficult to quantify the validity of the assumptions employed in the loading models. Recent models of mascon formation invoke a two-stage process (basin formation, followed by isostatic adjustment), and it is not trivial to incorporate these aspects into standard analytic flexure models. Furthermore, the thickness of the mare fill is oftentimes not known, and this is critical for fitting the present-day central gravitational anomaly. An alternative method for estimating the elastic thickness is by comparing the location of tectonic features (such as faults and graben) to that predicted by a specified loading model (e.g., Solomon and Head, 1980). Detailed modeling of the Serenitatis basin (Freed et al., 2001) suggests that its elastic thickness was about 25 km when the concentric rilles formed and probably greater than 70 km when the younger compressional ridges formed.

Modeling of the lunar gravity field shows that there are several features related to subsurface density anomalies. As one example, two positive Bouguer gravitational anomalies are found in the vicinity of the Marius Hills volcanic complex (Kiefer, 2013). These positive anomalies most likely represent basaltic intrusions that are more dense than the surrounding crust. If these are modeled as sills, they need to be several kilometers thick and could potentially represent the magma chamber that is responsible for the numerous volcanic domes found in this region. Another example of subsurface density anomalies is linear gravitational anomalies, many of which are several hundred kilometers in length (Andrews-Hanna et al., 2013). These linear anomalies are most visible when plotting horizontal gradients of the gravity tensor (cf. Petrovskaya and Vershkov, 2006) and are plausibly the expression of ancient magmatic dikes that formed when the lunar lithosphere was in a state of extension.

Finally, one curious large-scale feature of Moon is the amplitude of its degree-2 gravity and topography terms. If the Moon were in hydrostatic equilibrium, the amplitude of the C_{20} and C_{22} terms would be directly relatable to the Earth–Moon separation (cf. eqn [21]). The present-day magnitudes of these coefficients, however, are much greater than would be expected for equilibrium at the present time. This has led to the suggestion that the equilibrium shape of the Moon was frozen into the lithosphere when it was closer to Earth early in its orbital evolution (e.g., Jeffreys, 1976; Lambeck and Pullan, 1980). Alternatively, it is possible that this shape is simply a result of large-scale crustal thickness variations or lateral variations in mantle density.

If the observed shape is interpreted as a relict equilibrium shape, then this can be achieved for an Earth–Moon separation of 22 Earth radii with an orbital eccentricity of 0.49 (the current separation and eccentricity are about 60 Earth radii and 0.0549, respectively). If the Moon was in a 3/2 spin–orbit resonance (like Mercury), then alternative solutions exist for an Earth–Moon separation of about 25 Earth radii with eccentricities as low as 0.17. These interpretations are somewhat problematic as the lunar orbit is predicted to have receded beyond this distance in less than ~100 My after the formation of the Earth–Moon system (e.g., Webb, 1982). Furthermore, Ćuk (2011) pointed out that capture into either the synchronous or 3/2 resonance is difficult for the proposed high eccentricities.

10.05.9 Future Developments and Concluding Remarks

The gravitational fields and topography of the terrestrial planets have become increasingly better characterized since the discovery of lunar 'mascons' by Muller and Sjogren in 1968. Whereas the early datasets were quite sparse, the gradual accumulation of data with each successive space mission has given rise to near-global gravity and topography spherical harmonic models. Some of the gravity models now possess spherical harmonic bandwidths greater than 900, and future missions will certainly lead to continued improvements.

Not only has the resolution of the planetary datasets continued to improve with time, but also so have the analysis techniques. Early investigations were often restricted to analyses of individual 1-D line-of-sight gravitational acceleration profiles. As data coverage became more dense, 2-D regional models were developed that were more often than not

analyzed using Cartesian techniques developed for Earth. Because of the small size of some planetary bodies, the assumption of Cartesian geometry is not always justified, and spherical analysis methods have proven to be superior. The full suite of Cartesian gravity–topography analysis techniques has been developed for the sphere, including multitaper spectral analysis, wavelet analysis, the rapid calculation of gravitational anomalies from finite-amplitude topographic relief, and realistic admittance models that take into account surface and subsurface loading. Though the approximation of Cartesian geometry may not incur large errors for some small-scale investigations, it is just as easy to use a spherical-based method that possesses a comparable computational speed.

Much has been learned about the crustal and lithospheric structures of the terrestrial planets, but there is still much to be done. In particular, in hindsight, it is now clear that many gravity–topography admittance and coherence studies have used analysis techniques whose robustness are sometimes difficult to assess. Shortcomings include incorrect application of the multitaper spectral analysis technique, the neglect of either the admittance or correlation function, and the use of a theoretical admittance model that might be an oversimplification of reality. Few studies, even for Earth, have performed these analyses entirely correctly, and one should assess critically each of the elastic thickness estimates that have been published for regions where subsurface loading is important.

It is also important to note that the concept of an elastic lithosphere, which is often used in gravitational analyses, is in actuality a gross oversimplification of reality. Because of the ease of generating a time-invariant flexural profile from a load emplaced on an elastic plate, one would like to hope that the obtained 'effective elastic thickness' has some physical meaning. Though this might be the case for regions where the magnitude of surface and subsurface loading is small and where in-plane forces are absent, it has been demonstrated that the use of a more realistic rheology can yield flexural profiles that sometimes are quite different. Unfortunately, the most realistic EVP models are computationally expensive and are not currently amenable to a robust inversion procedure using gravity and topography as constraints. A simpler elastic–plastic formulation could be used in such an inversion, but this rheological model utilizes assumptions that still might turn out to be too simplistic. Regardless, it would be appropriate to develop an elastic–plastic loading model similar to the elastic model described in **Section 10.05.7** for the sphere. One benefit of such a model is that it would be possible to invert for the regional heat flow. An additional avenue of future research is to compare the locations of surface faulting with those predicted from elastic, elastic–plastic, and EVP models.

Finally, it is worth mentioning that significant improvements to our knowledge of the gravitational fields and topography of the terrestrial planets can be expected in the future. In particular, even though the land-based topography for Earth is now known to high accuracy, there are still gaps near the polar regions that could be filled by data obtained by the orbiting Geoscience Laser Altimeter System (GLAS) laser altimeter (e.g., Abshire et al., 2005; Schutz et al., 2005; Shuman et al., 2006). Data obtained from the terrestrial mission GOCE, which contains a gravity gradiometer, are leading to improved models of the terrestrial gravity field. An area of active research for Earth, but also for the other planets in a more limited sense, is that of measuring and modeling time-variable gravity signatures that are a result of hydrologic processes and tidal deformation.

With respect to the other planets, the topography and gravity field of Mercury are continuing to be characterized by data collected by the MESSENGER spacecraft (Solomon et al., 2001), and these will be supplemented by data that will be collected by the future BepiColombo mission (Spohn et al., 2001). The JUpiter ICy moons Explorer (JUICE) will collect altimetric and gravity data for the icy satellite Ganymede and to a limited extent Europa and Ganymede. Limited gravitational data will also be collected during the end of the Venus Express mission and during the MAVEN mission to Mars.

Acknowledgments

I am indebted to Greg Neumann and Frederik Simons for their numerous discussions relating to the more subtle details of gravity and topography acquisition and analysis. Francis Nimmo, Bruce Bills, Alex Konopliv, David Sandwell, Erwan Mazarico, and Martin Pauer are kindly thanked for their constructive reviews and discussions that helped improve this manuscript. Most figures were created using the Generic Mapping Tools of Wessel and Smith (1991).

References

Abe S, Mukai T, Hirata N, et al. (2006) Mass and local topography measurements of Itokawa by Hayabusa. *Science* 312: 1344–1349. http://dx.doi.org/10.1126/science.1126272.

Abshire JB, Sun X, Riris H, et al. (2005) Geoscience Laser Altimeter System (GLAS) on the ICESat mission: On-orbit measurement performance. *Geophysical Research Letters* 32: L21S02. http://dx.doi.org/10.1029/2005GL024028.

Albert R and Phillips RJ (2000) Paleoflexure. *Geophysical Research Letters* 27: 2385–2388.

Albert R, Phillips RJ, Dombard A, and Brown C (2000) A test of the validity of yield strength envelopes with an elastoviscoplastic finite element model. *Geophysical Journal International* 140: 399–409.

Amante C and Eakins BW (2009) ETOPO1 1 arc-minute global relief model: Procedures, data sources and analysis. NOAA Technical Memorandum NESDIS NGDC-24, 19 pp.

Anderson FS and Smrekar SE (2006) Global mapping of crustal and lithospheric thickness on Venus. *Journal of Geophysical Research* 111: E08006. http://dx.doi.org/10.1029/2004JE002395.

Anderson JD, Colombo G, Esposito PB, Lau EL, and Trager GB (1987) The mass, gravity field, and ephemeris of Mercury. *Icarus* 71: 337–349.

Anderson JD, Jacobson RA, Lau EL, Moore WB, and Schubert G (2001a) Io's gravity field and interior structure. *Journal of Geophysical Research* 106: 32963–32969.

Anderson JD, Jacobson RA, McElrath TP, Moore WB, and Schubert G (2001b) Shape, mean radius, gravity field, and interior structure of Callisto. *Icarus* 153: 157–161.

Anderson JD, Jurgens RF, Lau EL, Slade MA III, and Schubert G (1996a) Shape and orientation of Mercury from radar ranging data. *Icarus* 124: 690–697.

Anderson JD, Lau EL, Sjogren WL, Schubert G, and Moore WB (1996b) Gravitational constraints on the internal structure of Ganymede. *Nature* 384: 541–543.

Anderson JD and Schubert G (2010) Rhea's gravitational field and interior structure inferred from archival data files of the 2005 Cassini flyby. *Physics of the Earth and Planetary Interiors* 178: 176–182. http://dx.doi.org/10.1016/j.pepi.2009.09.003.

Anderson JD, Schubert G, Jacobson RA, Lau EL, Moore WB, and Sjogren WL (1998) Europa's differentiated internal structure: Inferences from four Galileo encounters. *Science* 281: 2019–2022.

André SL, Watters TR, and Robinson MS (2005) The long wavelength topography of Beethoven and Tolstoj basins, Mercury. *Geophysical Research Letters* 32: L21202. http://dx.doi.org/10.1029/2005GL023627.

Andrews-Hanna JC (2013) The origin of the non-mare mascon gravity anomalies in lunar basins. *Icarus* 222: 159–168. http://dx.doi.org/10.1016/j.icarus.2012.10.031.

Andrews-Hanna JC, Asmar SW, Head JW, et al. (2013) Ancient igneous intrusions and early expansion of the Moon revealed by GRAIL gravity gradiometry. *Science* 339: 675–678. http://dx.doi.org/10.1126/science.1231753.

Araki H, Tazawa S, Nodo H, et al. (2009) Lunar global shape and polar topography derived from Kaguya-LALT laser altimetry. *Science* 323: 897–900. http://dx.doi.org/10.1126/science.1164146.

Archinal BA, A'Hearn MF, Bowell E, et al. (2011a) Report of the IAU working group on cartographic coordinates and rotational elements: 2009. *Celestial Mechanics and Dynamical Astronomy* 109: 101–135. http://dx.doi.org/10.1007/s10569-010-9320-4.

Archinal BA, A'Hearn MF, Bowell E, et al. (2011b) Erratum to: Reports of the IAU working group on cartographic coordinates and rotational elements: 2006 & 2009. *Celestial Mechanics and Dynamical Astronomy* 110: 401–403. http://dx.doi.org/10.1007/s10569-011-9362-2.

Ardalan AA, Karimi R, and Grafarend EW (2010) A new reference equipotential surface, and reference ellipsoid for the planet Mars. *Earth, Moon, and Planets* 106: 1–13.

Arkani-Hamed J (1998) The lunar mascons revisited. *Journal of Geophysical Research* 103: 3709–3739.

Audet P (2011) Directional wavelet analysis on the sphere: Application to gravity and topography of the terrestrial planets. *Journal of Geophysical Research* 116: E01003. http://dx.doi.org/10.1029/2010JE003710.

Audet P (2013) Toward mapping the effective elastic thickness of planetary lithospheres from a spherical wavelet analysis of gravity and topography. *Physics of the Earth and Planetary Interiors* 226: 48–82. http://dx.doi.org/10.1016/j.pepi.2013.09.011.

Balmino G (1993) The spectra of the topography of the Earth, Venus, and Mars. *Geophysical Research Letters* 20: 1063–1066.

Balmino G (1994) Gravitational potential harmonics from the shape of an homogeneous body. *Celestial Mechanics and Dynamical Astronomy* 60: 331–364.

Balmino G, Vales N, Bonvalot S, and Briais A (2012) Spherical harmonic modelling to ultra-high degree of Bouguer and isostatic anomalies. *Journal of Geodesy* 86: 499–520. http://dx.doi.org/10.1007/s00190-011-0533-4.

Banerdt WB (1986) Support of long-wavelength loads on Venus and implications for internal structure. *Journal of Geophysical Research* 91: 403–419.

Banerdt WB, Golombek M, and Tanaka K (1992) Stress and tectonics on Mars. In: Jakosky B, Snyder C, Matthews M, and Kieffer H (eds.) *Mars*, pp. 249–297. Tucson, AZ: University of Arizona Press.

Banks RJ, Francis SC, and Hipkin RG (2001) Effects of loads in the upper crust on estimates of the elastic thickness of the lithosphere. *Geophysical Journal International* 145: 291–299.

Barnett DN, Nimmo F, and McKenzie D (2000) Elastic thickness estimates for Venus using line of sight accelerations from Magellan cycle 5. *Icarus* 146: 404–419.

Barnett DN, Nimmo F, and McKenzie D (2002) Flexure of Venusian lithosphere measured from residual topography and gravity. *Journal of Geophysical Research* 107: E2. http://dx.doi.org/10.1029/2000JE001398.

Bechtel TD, Forsyth DW, Sharpton VL, and Grieve RAF (1990) Variations in effective elastic thickness of the North-American lithosphere. *Nature* 343: 636–638.

Bechtel TD, Forsyth DW, and Swain CJ (1987) Mechanisms of isostatic compensation in the vicinity of the East African Rift, Kenya. *Geophysical Journal of the Royal Astronomical Society* 90: 445–465.

Belleguic V, Lognonné P, and Wieczorek M (2005) Constraints on the Martian lithosphere from gravity and topography data. *Journal of Geophysical Research* 110: E11005. http://dx.doi.org/10.1029/2005JE002437.

Beuthe M (2008) Thin elastic shells with variable thickness for lithospheric flexure of one-plate planets. *Geophysical Journal International* 171: 817–841. http://dx.doi.org/10.1111/j.1365-246X.2007.03671.x.

Beuthe M, Maistre SL, Rosenblatt P, Pätzold M, and Dehant V (2012) Density and lithospheric thickness of the Tharsis Province from MEX MaRS and MRO gravity data. *Journal of Geophysical Research* 117: E04002. http://dx.doi.org/10.1029/2011JE003976.

Bills BG and Lemoine FG (1995) Gravitational and topographic isotropy of the Earth, Moon, Mars, and Venus. *Journal of Geophysical Research* 100: 26275–26295.

Blakely RJ (1995) *Potential Theory in Gravity and Magnetic Applications*. New York: Cambridge University Press.

Brown CD and Grimm RE (1996) Lithospheric rheology and flexure at Artemis Chasma, Venus. *Journal of Geophysical Research* 101: 12697–12708.

Brown CD and Phillips RJ (2000) Crust–mantle decoupling by flexure of continental lithosphere. *Journal of Geophysical Research* 105: 13221–13237.

Burov EB and Diament M (1995) The effective elastic thickness (T_e) of continental lithosphere: What does it really mean? *Journal of Geophysical Research* 100: 3905–3927.

Ceuleneer G, Rabinowicz M, Monnereau M, Cazenave A, and Rosemberg C (1988) Viscosity and thickness of the sub-lithospheric low-viscosity zone: Constraints from geoid and depth over oceanic swells. *Earth and Planetary Science Letters* 89: 84–102.

Chambat F and Valette B (2005) Earth gravity up to second order in topography and density. *Physics of the Earth and Planetary Interiors* 151: 89–106.

Chambodut A, Panet I, Mandea M, Diament M, Holschneider M, and Jamet O (2005) Wavelet frames: An alternative to spherical harmonic representation of potential fields. *Geophysical Journal International* 163: 875–899. http://dx.doi.org/10.1111/j.1365-246X.2005.02754.x.

Chao BF and Rubincam DP (1989) The gravitational field of Phobos. *Geophysical Research Letters* 16: 859–862.

Chenet H, Lognonné P, Wieczorek M, and Mizutani H (2006) Lateral variations of lunar crustal thickness from the Apollo seismic data set. *Earth and Planetary Science Letters* 243: 1–14.

Cheng AF, Barnouin-Jha O, Prockter L, et al. (2002) Small-scale topography of 433 Eros from laser altimetry and imaging. *Icarus* 155: 51–74.

Clark PE, Jurgens RF, and Leake MA (1988) Goldstone radar observations of Mercury. In: Vilas F, Chapman CR, and Matthews MS (eds.) *Mercury*, pp. 77–100. Tucson, AZ: University of Arizona Press.

Correia ACM and Laskar J (2009) Mercury's capture into the 3/2 spin–orbit resonance including the effect of core–mantle friction. *Icarus* 201: 1–11. http://dx.doi.org/10.1016/j.icarus.2008.12.034.

Crosby A and McKenzie D (2005) Measurements of the elastic thickness under ancient lunar terrain. *Icarus* 173: 100–107.

Ćuk M (2011) Lunar shape does not record a past eccentric orbit. *Icarus* 211: 97–100. http://dx.doi.org/10.1016/j.icarus.2010.08.027.

Dahlen FA and Tromp J (1998) *Theoretical Global Seismology*. Princeton, NJ: Princeton University Press.

Davies ME and Batson RM (1975) Surface coordinates and cartography of Mercury. *Journal of Geophysical Research* 80: 2417–2430.

Dermott SF (1979) Shapes and gravitational moments of satellites and asteroids. *Icarus* 37: 575–586.

Dermott SF and Thomas PC (1988) The shape and internal structure of Mimas. *Icarus* 73: 25–65. http://dx.doi.org/10.1016/0019-1035(88)90084-X.

Dorman LM and Lewis BT (1970) Experimental isostasy: 1. Theory of the determination of the Earth's isostatic response to a concentrated load. *Journal of Geophysical Research* 75: 3357–3365.

Drinkwater M, Floberghagen R, Haagmans R, Muzi D, and Popescu A (2003) GOCE: ESA's first Earth Explorer Core mission. *Space Science Reviews* 108: 419–432. http://dx.doi.org/10.1023/A:1026104216284.

Driscoll JR and Healy DM (1994) Computing Fourier transforms and convolutions on the 2-sphere. *Advances in Applied Mathematics* 15: 202–250. http://dx.doi.org/10.1006/aama.1994.1008.

Ebinger C, Bechtel T, Forsyth D, and Bowin C (1989) Effective elastic plate thickness beneath the east African and Afar plateaus and dynamic compensation of the uplifts. *Journal of Geophysical Research* 94: 2883–2901.

Esposito P, Benerdt W, Lindal G, Sjogren W, and Slade M (1992) Gravity and topography. In: Jakosky B, Snyder C, Matthews M, and Kieffer H (eds.) *Mars*, pp. 209–248. Tucson, AZ: University of Arizona Press.

Fedi M and Florio G (2002) A stable downward continuation by using the ISVD method. *Geophysical Journal International* 151: 146–156.

Fengler MJ, Freeden W, Kohlhas A, Michel V, and Peters T (2007) Wavelet modeling of regional and temporal variations of the Earth's gravitational potential observed by GRACE. *Journal of Geodesy* 81: 5–15. http://dx.doi.org/10.1007/s00190-006-0040-1.

Floberghagen R, Fehringer M, Lamarre D, et al. (2011) Mission design, operation and exploitation of the gravity field and steady-state ocean circulation explorer mission. *Journal of Geodesy* 85: 749–758. http://dx.doi.org/10.1007/s00190-011-0498-3.

Ford P and Pettengill G (1992) Venus topography and kilometer-scale slopes. *Journal of Geophysical Research* 97: 13103–13114.

Förste C, Bruinsma SL, Flechtner F, et al. (2012) A new release of EIGEN-6C. In: *AGU Fall Meeting, San Francisco, 3–7 December, G31B–0923*.

Forsyth DW (1985) Subsurface loading and estimates of the flexural rigidity of continental lithosphere. *Journal of Geophysical Research* 90: 12623–12632.

Freed AM, Melosh HJ, and Solomon SC (2001) Tectonics of mascon loading: Resolution of the strike-slip faulting paradox. *Journal of Geophysical Research* 106: 20603–20620.

Freeden W and Windheuser U (1997) Combined spherical harmonic and wavelet expansion—A future concept in Earth's gravitational determination. *Applied and Computational Harmonic Analysis* 4: 1–37.

Fukushima T (2011) Numerical computation of spherical harmonics of arbitrary degree and order by extending exponent of floating point numbers. *Journal of Geodesy* 86: 271–285. http://dx.doi.org/10.1007/s00190-011-0519-2.

Garmier R and Barriot JP (2001) Ellipsoidal harmonic expansions of the gravitational potential: Theory and application. *Celestial Mechanics and Dynamical Astronomy* 79: 235–275.
Garrick-Bethell I, Wisdom J, and Zuber MT (2006) Evidence for a past high-eccentricity lunar orbit. *Science* 313: 652–655. http://dx.doi.org/10.1126/science.1128237.
Gaskell RW, Barnouin-Jha OS, Scheeres DJ, et al. (2008) Characterizing and navigating small bodies with imaging data. *Meteoritics and Planetary Science* 43: 1049–1061. http://dx.doi.org/10.1111/j.1945-5100.2008.tb00692.x.
Genova A, Iess L, and Marabucci M (2013) Mercury's gravity field from the first six months of MESSENGER data. *Planetary and Space Science* 81: 55–64. http://dx.doi.org/10.1016/j.pss.2013.02.006.
Ghent ED, Dipple GM, and Russell JK (2004) Thermodynamic models for eclogite mantle lithosphere. *Journal of Geophysical Research* 218: 451–462.
Giese B, Denk T, Neukum G, et al. (2008) The topography of Iapetus' leading side. *Icarus* 193: 359–371. http://dx.doi.org/10.1016/j.icarus.2007.06.005.
Giese B, Oberst J, Roatsch T, Neukum G, Head JW, and Pappalardo R (1998) The local topography of Uruk Sulcus and Galileo Regio obtained from stereo images. *Icarus* 135: 303–316.
Goossens S, Matsumoto K, Liu Q, et al. (2011) Lunar gravity field determination using selene same-beam differential VLBI tracking data. *Journal of Goedesy* 85: 205–228. http://dx.doi.org/10.1007/s00190-010-0430-2.
Grimm RE (1994) The deep structure of Venusian plateau highlands. *Icarus* 112: 89–103.
Grimm RE and Hess PC (1997) The crust of Venus. In: Bougher SW, Hunten DM, and Phillips RJ (eds.) *Venus II*, pp. 1205–1244. Tucson, AZ: University of Arizona Press.
Grimm RE and Phillips RJ (1991) Gravity anomalies, compensation mechanisms, and the geodynamics of Western Ishtar Terra, Venus. *Journal of Geophysical Research* 96: 8309–8324.
Grott M, Baratoux D, Hauber E, et al. (2013) Long-term evolution of the Martian crust–mantle system. *Space Science Reviews* 174: 49–111. http://dx.doi.org/10.1007/s11214-012-9948-3.
Grott M and Wieczorek MA (2012) Density and lithospheric structure at Tyrrhena Patera, Mars, from gravity and topography data. *Icarus* 221: 43–52. http://dx.doi.org/10.1016/j.icarus.2012.07.008.
Guilloux F, Faÿ G, and Cardoso JF (2009) Practical wavelet design on the sphere. *Applied and Computational Harmonic Analysis* 26: 143–160. http://dx.doi.org/10.1016/j.acha.2008.03.003.
Haines GV (1985) Spherical cap harmonic analysis. *Journal of Geophysical Research* 90: 2583–2591.
Han SC, Mazarico E, and Lemoine FG (2009) Improved nearside gravity field of the Moon by localizing the power law constraint. *Geophysical Research Letters* 36: L11203. http://dx.doi.org/10.1029/2009GL038556.
Hansen VL and Phillips RJ (1995) Formation of Ishtar Terra, Venus: Surface and gravity constraints. *Geology* 23: 292–296.
Harmon JK, Campbell DB, Bindschadler DL, Head JW, and Shapiro II (1986) Radar altimetry of Mercury: A preliminary analysis. *Journal of Geophysical Research* 91: 385–401.
Haruyama J, Matsunaga T, Ohtake M, et al. (2008) Global lunar-surface mapping experiment using the lunar imager/spectrometer on selene. *Earth Planets Space* 60: 243–255.
Hastings DA and Dunbar PK (1999) Global Land One-kilometer Base Elevation (GLOBE) Digital Elevation Model, Documentation, Volume 1.0. Key to Geophysical Records Documentation (KGRD) 34. Boulder, CO: National Oceanic and Atmospheric Administration, National Geophysical Data Center.
Hauck SA II, Phillips RJ, and Price MH (1998) Venus: Crater distribution and plains resurfacing models. *Journal of Geophysical Research* 103: 13635–13642.
Haxby WF and Turcotte DL (1978) On isostatic geoid anomalies. *Journal of Geophysical Research* 83: 5473–5478.
Heiskanen WA and Moritz H (1967) *Physical Geodesy*. San Francisco, CA: Freeman.
Hikida H and Wieczorek MA (2007) Crustal thickness of the Moon: New constraints from gravity inversions using polyhedral shape models. *Icarus* 192: 150–166. http://dx.doi.org/10.1016/j.icarus.2007.06.015.
Hirt C (2012) Efficient and accurate high-degree spherical harmonic synthesis of gravity field functionals at the Earth's surface using the gradient approach. *Journal of Geodesy* 86: 729–744. http://dx.doi.org/10.1007/s00190-012-0550-y.
Hirt C, Featherstone WE, and Göttl F (2012) Topographic/isostatic evaluation of new-generation GOCE gravity field models. *Journal of Geophysical Research* 117: B05407. http://dx.doi.org/10.1029/2011JB008878.
Hofmann-Wellenhof B and Moritz H (2006) *Physical Geodesy*, 2nd edn. Wien, Austria: Springer Wien-New York.
Holmes SA and Featherstone WE (2002) A unified approach to the Clenshaw summation and the recursive computation of very high degree and order normalised associated Legendre functions. *Journal of Geodesy* 76: 279–299.
Holschneider M, Chambodut A, and Mandea M (2003) From global to regional analysis of the magnetic field on the sphere using wavelet frames. *Physics of the Earth and Planetary Interiors* 135: 107–124. http://dx.doi.org/10.1016/S0031-9201(02)00210-8.
Holschneider M and Iglewska-Nowak I (2007) Poisson wavelets on the sphere. *Journal of Fourier Analysis and Applications* 13: 405–419. http://dx.doi.org/10.1007/s00041-006-6909-9.
Hoogenboom T, Houseman TG, and Martin P (2005) Elastic thickness estimates for coronae associated with chasmata on Venus. *Journal of Geophysical Research* 110: E09003. http://dx.doi.org/10.1029/2004JE002394.
Hoogenboom T and Smrekar SE (2006) Elastic thickness estimates for the northern lowlands of Mars. *Earth and Planetary Science Letters* 248: 830–839. http://dx.doi.org/10.1016/j.epsl.2006.06.035.
Hoogenboom T, Smrekar SE, Anderson FS, and Houseman G (2004) Admittance survey of type 1 coronae on Venus. *Journal of Geophysical Research* 109: E03002. http://dx.doi.org/10.1029/2003JE002171.
Huang J, Yang A, and Zhong S (2013) Constraints of the topography, gravity and volcanism on Venusian mantle dynamics and generation of plate tectonics. *Earth and Planetary Science Letters* 362: 207–214. http://dx.doi.org/10.1016/j.epsl.2012.11.051.
Huang Q and Wieczorek MA (2012) Density and porosity of the lunar crust from gravity and topography. *Journal of Geophysical Research* 117: E05003. http://dx.doi.org/10.1029/2012JE004062.
Hwang C and Chen SK (1997) Fully normalized spherical cap harmonics: Application to the analysis of sea-level data from TOPEX/POSEIDON and ERS-1. *Geophysical Journal International* 129: 450–460.
Hwang C and Parsons B (1996) An optimal procedure for determining gravity from multi-satellite altimetry. *Geophysical Journal International* 125: 705–719.
Iess L, Rappaport NJ, Jacobson RA, et al. (2010) Gravity field, shape, and moment of inertia of Titan. *Science* 327: 1367–1369. http://dx.doi.org/10.1126/science.1182583.
Ishihara Y, Goossens S, Matsumoto K, et al. (2009) Crustal thickness of the Moon: Implications for farside basin structures. *Geophysical Research Letters* 36: L19202. http://dx.doi.org/10.1029/2009GL039708.
Jacobson R (2010) The orbits and masses of the martian satellites and the libration of phobos. *Astronomical Journal* 139: 668679. http://dx.doi.org/10.1088/0004-6256/139/2/668.
James PB, Zuber MT, and Phillips RJ (2013) Crustal thickness and support of topography on Venus. *Journal of Geophysical Research: Planets* 118: 859–875. http://dx.doi.org/10.1029/2012JE004237.
Jaumann R, Williams DA, Buczkowski DL, et al. (2012) Vesta's shape and morphology. *Science* 336: 687–690. http://dx.doi.org/10.1126/science.1219122.
Jeffreys H (1976) *The Earth: Its Origin History and Physical Constitution*, 6th edn. New York: Cambridge University Press.
Jekeli C (1988) The exact transformation between ellipsoidal and spherical harmonic expansions. *Manuscripta Geodaetica* 14: 106113.
Jekeli C, Lee JK, and Kwon JH (2007) On the computation and approximation of ultra-high-degree spherical harmonic series. *Journal of Geodesy* 81: 603–615. http://dx.doi.org/10.1007/s00190-006-0123-z.
Johnson C, Solomon S, Head JW III, Phillips RJ, Smith D, and Zuber M (2000) Lithospheric loading by the northern polar cap on Mars. *Icarus* 144: 313–328.
Johnson CL and Sandwell DT (1994) Lithospheric flexure on Venus. *Geophysical Journal International* 119: 627–647.
Kaula WM (1967) Theory of statistical analysis of data distributed over a sphere. *Reviews of Geophysics* 5: 83–107.
Kaula WM (2000) *Theory of Satellite Geodesy: Applications of Satellites to Geodesy*. Mineola, NY: Dover.
Khan A and Mosegaard K (2002) An enquiry into the lunar interior—A non-linear inversion of the Apollo lunar seismic data. *Journal of Geophysical Research* 107: 5036. http://dx.doi.org/10.1029/2001JE001658.
Kiefer W (2004) Gravity evidence for an extinct magma chamber beneath Syrtis Major, Mars: A look at the magmatic plumbing system. *Earth and Planetary Science Letters* 222: 349–361.
Kiefer W (2005) Buried mass anomalies along the hemispheric dichotomy in eastern Mars: Implications for the origin and evolution of the dichotomy. *Geophysical Research Letters* 32: L22201. http://dx.doi.org/10.1029/2005GL024260.
Kiefer WS (2013) Gravity constraints on the subsurface structure of the Marius Hills: The magmatic plumbing of the largest lunar volcanic dome complex. *Journal of Geophysical Research: Planets* 118: 733–745. http://dx.doi.org/10.1029/2012JE004111.

Kiefer WS and Hager BF (1991) A mantle plume model for the equatorial highlands of Venus. *Journal of Geophysical Research* 96: 20947–20966.

Kiefer WS, Richards MA, and Hager BH (1986) A dynamic model of Venus's gravity field. *Geophysical Research Letters* 13: 14–17.

Kirby JF and Swain CJ (2006) Mapping the mechanical anisotropy of the lithosphere using a 2D wavelet coherence, and its application to Australia. *Physics of the Earth and Planetary Interiors* 158: 122–138. http://dx.doi.org/10.1016/j.pepi.2006.03.022.

Kirby JF and Swain CJ (2009) A reassessment of spectral T_e estimation in continental interiors: The case of North America. *Journal of Geophysical Research* 114: B08401. http://dx.doi.org/10.1029/2009JB006356.

Konopliv AS, Asmar SW, Folkner WM, et al. (2011) Mars high resolution gravity fields from MRO, Mars seasonal gravity, and other dynamical parameters. *Icarus* 211: 401–428. http://dx.doi.org/10.1016/j.icarus.2010.10.004.

Konopliv AS, Asmar SW, Park RS, et al. (2013a) The vesta gravity field, spin pole and rotation period, landmark positions, and ephemeris from the dawn tracking and optical data. *Icarus* http://dx.doi.org/10.1016/j.icarus.2013.09.005, in press.

Konopliv AS, Asmar SW, and Yuan DN (2001) Recent gravity models as a result of the Lunar Prospector mission. *Icarus* 150: 1–18.

Konopliv AS, Banerdt WB, and Sjogren WL (1999) Venus gravity: 180th degree and order model. *Icarus* 139: 3–18.

Konopliv AS, Binder AB, Hood LL, Kucinskas AB, Sjogren WL, and Williams JG (1998) Improved gravity field of the Moon from Lunar Prospector. *Science* 281: 1476–1480.

Konopliv AS, Park RS, Yuan DN, et al. (2013b) The JPL lunar gravity field to spherical harmonic degree 660 from the GRAIL primary mission. *Journal of Geophysical Research: Planets* 1415–1434. http://dx.doi.org/10.1002/jgre.20097.

Konopliv AS, Yoder CF, Standish EM, Yuan DN, and Sjogren WL (2006) A global solution for the Mars static and seasonal gravity, Mars orientation, Phobos and Deimos masses, and Mars ephemeris. *Icarus* 182: 23–50.

Kraus H (1967) *Thin Elastic Shells: An Introduction to the Theoretical Foundations and the Analysis of Their Static and Dynamic Behavior*. New York: John Wiley.

Kucinskas AB and Turcotte DT (1994) Isostatic compensation of equatorial highlands on Venus. *Icarus* 112: 104–116.

Lambeck K (1988) *Geophysical Geodesy*. New York: Oxford University Press.

Lambeck K and Pullan S (1980) The lunar fossil bulge hypothesis revisited. *Physics of the Earth and Planetary Interiors* 22: 29–35.

Lawrence KP and Phillips RJ (2003) Gravity/topography admittance inversion on Venus using niching genetic algorithms. *Geophysical Research Letters* 30: 1994. http://dx.doi.org/10.1029/2003GL017515.

Le Feuvre M and Wieczorek MA (2011) Nonuniform cratering of the Moon and a revised crater chronology of the inner Solar System. *Icarus* 214: 1–20. http://dx.doi.org/10.1016/j.icarus.2011.03.010.

Lemoine F, Kenyon S, Factor JK, et al. (1998) *The Development of the Joint NASA GSFC and the National Imagery and Mapping Agency (NIMA) Geopotential Model EGM96*. Greenbelt, MD: NASA Goddard Space Flight Cent.

Lemoine FG, Goossens S, Sabaka TJ, et al. (2013) High-degree gravity models from GRAIL primary mission data. *Journal of Geophysical Research: Planets* 118: 1676–1698. http://dx.doi.org/10.1002/jgre.20118.

Lemoine FG, Smith DE, Rowlands DD, et al. (2001) An improved solution of the gravity field of Mars (GMM-2B) from Mars Global Surveyor. *Journal of Geophysical Research* 106: 23359–23376.

Li TH (1999) Multiscale representation and analysis of spherical data by spherical wavelets. *SIAM Journal on Scientific Computing* 21: 924–953.

Lognonné P, Gagnepain-Beyneix J, and Chenet H (2003) A new seismic model for the Moon: Implications for structure, thermal evolution and formation of the Moon. *Earth and Planetary Science Letters* 211: 27–44.

Lorenz RD, Stiles BW, Aharonson O, et al. (2013) A global topographic map of Titan. *Icarus* 225: 367–377. http://dx.doi.org/10.1016/j.icarus.2013.04.002.

Lowry AR and Zhong S (2003) Surface versus internal loading of the Tharsis rise, Mars. *Journal of Geophysical Research* E9: 5099. http://dx.doi.org/10.1029/2003JE002111.

Marks KM and Smith WHF (2006) An evaluation of publicly available global bathymetry grids. *Marine Geophysical Research* 27: 19–34.

Martinec Z, Pěč K, and Burša M (1989) The Phobos gravitational field modeled on the basis of its topography. *Earth, Moon, and Planets* 45: 219–235.

Matsumoto K, Goossens S, Ishihara Y, et al. (2010) An improved lunar gravity field model from SELENE and historical tracking data: Revealing the farside gravity features. *Journal of Geophysical Research* 115: E06007. http://dx.doi.org/10.1029/2009JE003499.

McEwen JD, Hobson MP, Lasenby AN, and Mortlock DJ (2007) Fast directional continuous spherical wavelet transform algorithms. *IEEE Transactions on Signal Processing* 55: 520–529.

McGovern PJ, Solomon SC, Smith DE, et al. (2002) Localized gravity/topography admittance and correlation spectra on Mars: Implications for regional and global evolution. *Journal of Geophysical Research* 107: 5136. http://dx.doi.org/10.1029/2002JE001854.

McGovern PJ, Solomon SC, Smith DE, et al. (2004) Correction to "Localized gravity/topography admittance and correlation spectra on Mars: Implications for regional and global evolution" *Journal of Geophysical Research* 109. http://dx.doi.org/10.1029/2004JE002286.

McKenzie D (1994) The relationship between topography and gravity on Earth and Venus. *Icarus* 112: 55–88.

McKenzie D (2003) Estimating T_e in the presence of internal loads. *Journal of Geophysical Research* 108: 2348. http://dx.doi.org/10.1029/2002JB001766.

McKenzie D and Nimmo F (1997) Elastic thickness estimates for Venus from line of sight accelerations. *Icarus* 130: 198–216.

McKenzie DP, Barnett DN, and Yuan DN (2002) The relationship between Martian gravity and topography. *Earth and Planetary Science Letters* 195: 1–16.

McNutt MK (1984) Lithospheric flexure and thermal anomalies. *Journal of Geophysical Research* 89: 11180–11194.

Melosh HJ, Freed AM, Johnson BC, et al. (2013) The origin of lunar mascon basins. *Science* 1552–1555. http://dx.doi.org/10.1126/science.1235768.

Michel V and Wolf K (2008) Numerical aspects of a spline-based multiresolution recovery of the harmonic mass density out of gravity functionals. *Geophysical Journal International* 173: 1–16. http://dx.doi.org/10.1111/j.1365-246X.2007.03700.x.

Milbury CAE, Smrekar SE, Raymond CA, and Schubert G (2009) Lithospheric structure in the eastern region of Mars' dichotomy boundary. *Planetary and Space Science* 55: 280–288. http://dx.doi.org/10.1016/j.pss.2006.03.009.

Mohit PS, Johnson CL, Barnouin-Jha O, Zuber MT, and Solomon SC (2009) Shallow basins on Mercury: Evidence of relaxation? *Earth and Planetary Science Letters* 285: 355–363. http://dx.doi.org/10.1016/j.epsl.2009.04.023.

Mohr PJ, Taylor BN, and Newell DB (2012) CODATA recommended values of the fundamental physical constants, 2010. *Reviews of Modern Physics* 84: 1527–1605. http://dx.doi.org/10.1103/RevModPhys.84.1527.

Moore WB and Schubert G (1995) Lithospheric thickness and mantle/lithosphere density contrast beneath Beta Regio, Venus. *Geophysical Research Letters* 22: 429–432.

Moore WB and Schubert G (1997) Venusian crustal and lithospheric properties from nonlinear regressions of highland geoid and topography. *Icarus* 128: 415–428.

Moresi L and Solomatov V (1998) Mantle convection with a brittle lithosphere: Thoughts on the global tectonic styles of the Earth and Venus. *Geophysical Journal International* 133: 669–682.

Mueller S and Phillips RJ (1995) On the reliability of lithospheric constraints derived from models of outer-rise flexure. *Geophysical Journal International* 123: 887–902.

Muller PM and Sjogren WL (1968) Masons: Lunar mass concentrations. *Science* 161: 680–684.

Murray CD and Dermott SF (2008) *Solar System Dynamics*. Cambridge, UK: Cambridge University Press.

Narcowich FJ and Ward JD (1996) Nonstationary wavelets on the m-sphere for scattered data. *Applied and Computational Harmonic Analysis* 3: 324–336.

National Imagery and Mapping Agency (2000) *Department of Defense World Geodetic System 1984: Its Definition and Relationship with Local Geodetic Systems*. NIMA TR8350.2, National Imagery and Mapping Agency.

Neumann GA, Rowlands DD, Lemoine FG, Smith DE, and Zuber MT (2001) Crossover analysis of Mars Orbiter Laser Altimeter data. *Journal of Geophysical Research* 106: 23753–23768.

Neumann GA, Zuber MT, Smith DE, and Lemoine FG (1996) The lunar crust: Global structure and signature of major basins. *Journal of Geophysical Research* 101: 16841–16843.

Neumann GA, Zuber MT, Wieczorek MA, McGovern PJ, Lemoine FG, and Smith DE (2004) Crustal structure of Mars from gravity and topography. *Journal of Geophysical Research* 109. http://dx.doi.org/10.1029/2004JE002262.

Nimmo F (2002) Admittance estimates of mean crustal thickness and density at the Martian hemispheric dichotomy. *Journal of Geophysical Research* 107: 5117. http://dx.doi.org/10.1029/2000JE001488.

Nimmo F, Giese B, and Pappalardo RT (2003a) Estimates of Europa's ice shell thickness from elastically-supported topography. *Geophysical Research Letters* 30: 1233. http://dx.doi.org/10.1029/2002GL016660.

Nimmo F and McKenzie D (1998) Volcanism and tectonics on Venus. *Annual Review of Earth and Planetary Sciences* 26: 23–51.

Nimmo F, Pappalardo RT, and Giese B (2003b) On the origins of band topography, Europa. *Icarus* 166: 21–32. http://dx.doi.org/10.1016/j.icarus.2003.08.002.

Nimmo F and Stevenson DJ (2001) Estimates of Martian crustal thickness from viscous relaxation of topography. *Journal of Geophysical Research* 106: 5085–5098.

Nimmo F and Tanaka K (2005) Earth crustal evolution of Mars. *Annual Review of Earth and Planetary Sciences* 33: 133–161. http://dx.doi.org/10.1146/annurev.earth.33.092203.122637.

Nimmo F, Thomas PC, Pappalardo RT, and Moore WB (2007) The global shape of Europa: Constraints on lateral shell thickness variations. *Icarus* 191: 183–192. http://dx.doi.org/10.1016/j.icarus.2007.04.021.

Nimmo F and Watters TR (2004) Depth of faulting on mercury: Implications for heat flux and crustal and effective elastic thickness. *Geophysical Research Letters* 31: L02701. http://dx.doi.org/10.1029/2003GL018847.

Oberst J, Elgner S, Turner FS, et al. (2011) Radius and limb topography of Mercury obtained from images acquired during the MESSENGER flybys. *Planetary and Space Science* 59: 1918–1924. http://dx.doi.org/10.1016/j.pss.2011.07.003.

Ockendon JR and Turcotte DL (1977) On the gravitational potential and field anomalies due to thin mass layers. *Geophysical Journal of the Royal Astronomical Society* 48: 479–492.

Orth CP and Solomatov VS (2011) The isostatic stagnant lid approximation and global variations in the Venusian lithospheric thickness. *Geochemistry, Geophysics, Geosystems* 12: Q07018. http://dx.doi.org/10.1029/2011GC003582.

Orth CP and Solomatov VS (2012) Constraints on the Venusian crustal thickness variations in the isostatic stagnant lid approximation. *Geochemistry, Geophysics, Geosystems* 13: Q11012. http://dx.doi.org/10.1029/2012GC004377.

Pail R, Bruinsma S, Migliaccio F, et al. (2011) First GOCE gravity field models derived by three different approaches. *Journal of Geodesy* 85: 819–843. http://dx.doi.org/10.1007/s00190-011-0467-x.

Palguta J, Anderson JD, Schubert G, and Moore WB (2006) Mass anomalies on Ganymede. *Icarus* 180: 428–441. http://dx.doi.org/10.1016/j.icarus.2005.08.020.

Panasyuk SV and Hager BH (2000) Inversion for mantle viscosity profiles constrained by dynamic topography and the geoid, and their estimated errors. *Geophysical Journal International* 143: 821–836.

Panet I, Kuroishi Y, and Holschneider M (2011) Wavelet modelling of the gravity field by domain decomposition methods: An example over Japan. *Geophysical Journal International* 184: 203–219. http://dx.doi.org/10.1111/j.1365-246X.2010.04840.x.

Parker RL (1972) The rapid calculation of potential anomalies. *Geophysical Journal of the Royal Astronomical Society* 31: 447–455.

Parmetier EM and Hess PC (1992) Chemical differentiation of a convecting planetary interior: Consequences for a one plate planet such as Venus. *Geophysical Research Letters* 19: 2015–2018.

Pauer M and Breuer D (2008) Constraints on the maximum crustal density from gravity topography modeling: Applications to the southern highlands of mars. *Earth and Planetary Science Letters* 276: 253–261. http://dx.doi.org/10.1016/j.epsl.2008.09.014.

Pauer M, Fleming K, and Čadek O (2006) Modeling the dynamic component of the geoid and topography of Venus. *Journal of Geophysical Research* 111: 11012. http://dx.doi.org/10.1029/2005JE002511.

Pavlis NK, Holmes SA, Kenyon SC, and Factor JK (2012) The development and evaluation of the Earth Gravitational Model 2008 (EGM2008). *Journal of Geophysical Research* 117: B04406. http://dx.doi.org/10.1029/2011JB008916.

Peale SJ (1969) Generalized Cassini's laws. *Astronomical Journal* 74: 483–489. http://dx.doi.org/10.1086/110825.

Percival DB and Walden AT (1993) *Spectral Analysis for Physical Applications, Multitaper and Conventional Univariate Techniques*. New York: Cambridge University Press.

Pérez-Gussinyé M, Lowry A, Watts AB, and Velicogna I (2004) On the recovery of effective elastic thickness using spectral methods: Examples from synthetic data and from the Fennoscandian Shield. *Journal of Geophysical Research* 109: B10409. http://dx.doi.org/10.1029/2003JB002788.

Pérez-Gussinyé M, Swain CJ, Kirby JF, and Lowry AR (2009) Spatial variations of the effective elastic thickness, T_e, using multitaper spectral estimation and wavelet methods: Examples from synthetic data and application to South America. *Geochemistry, Geophysics, Geosystems* 10. http://dx.doi.org/10.1029/2008GC002229.

Perry ME, Kahan DS, Barnouin OS, et al. (2011) Measurement of the radius of Mercury by radio occultation during the MESSENGER flybys. *Planetary and Space Science* 59: 1925–1931. http://dx.doi.org/10.1016/j.pss.2011.07.022.

Petrovskaya MS and Vershkov AN (2006) Non-singular expressions for the gravity gradients in the local north-oriented and orbital reference frames. *Journal of Geodesy* 80: 117–127. http://dx.doi.org/10.1007/s00190-006-0031-2.

Phillips RJ (1994) Estimating lithospheric properties at Atla Regio. *Icarus* 112: 147–170.

Phillips RJ, Johnson CL, Mackwell SJ, Morgan P, Sandwell DT, and Zuber MT (1997) Lithospheric mechanics and dynamics of Venus. In: Bougher SW, Hunten DM, and Phillips RJ (eds.) *Venus II*, pp. 1163–1204. Tucson, AZ: University of Arizona Press.

Phillips RJ and Lambeck K (1980) Gravity fields of the terrestrial planets: Long wavelength anomalies and tectonics. *Reviews of Geophysics* 18: 27–76.

Phillips RJ, Zuber MT, Solomon SC, et al. (2001) Ancient geodynamics and global-scale hydrology on Mars. *Science* 291: 2587–2591.

Phipps Morgan J and Blackman DK (1993) Inversion of combined gravity and bathymetry data for crustal structure: A prescription for downward continuation. *Earth and Planetary Science Letters* 119: 167–179.

Ping J, Huang Q, Yan J, Cao J, Tang G, and Shu R (2009) Lunar topographic model CLTM-s01 from Chang'E-1 laser altimeter. *Science China Physics, Mechanics & Astronomy* 52: 1105–1114. http://dx.doi.org/10.1007/s11433-009-0144-8.

Press WH, Teukolsky SA, Vetterling WT, and Flannery BP (1992) *Numerical Recipes in FORTRAN: The Art of Scientific Computing*, 2nd edn. New York: Cambridge University Press.

Preusker F, Oberst J, Head JW, et al. (2011) Stereo topographic models of Mercury after three MESSENGER flybys. *Planetary and Space Science* 59: 1910–1917. http://dx.doi.org/10.1016/j.pss.2011.07.005.

Rabus PB, Eineder M, Roth A, and Bamler R (2003) The shuttle radar topography mission—A new class of digital elevation models acquired by spaceborne radar. *Photogrammetric Engineering & Remote Sensing* 57: 241–262.

Rambaux N and Bois E (2004) Theory of the Mercury's spin–orbit motion and analysis of its main librations. *Astronomy and Astrophysics* 413: 381–393. http://dx.doi.org/10.1051/0004-6361:20031446.

Rapp RH (1989) The decay of the spectrum of the gravitational potential and the topography of the Earth. *Geophysical Journal International* 99: 449–455.

Rappaport NJ, Konopliv AS, and Kucinskas AB (1999) An improved 360 degree and order model of Venus topography. *Icarus* 139: 19–31.

Reigber C, Jochmann H, Wünsch J, et al. (2004) Earth gravity field and seasonable variability from CHAMP. In: Reigber C, Lühr H, Schwintzer P, and Wickert J (eds.) *Earth Observations with CHAMP*, pp. 25–30. Berlin: Springer.

Reindler L and Arkani-Hamed J (2001) The compensation state of intermediate size lunar craters. *Icarus* 153: 71–88.

Ritzer JA and Hauck SA II (2009) Lithospheric structure and tectonics at Isidis Planitia, Mars. *Icarus* 201: 528–539. http://dx.doi.org/10.1016/j.icarus.2009.01.025.

Roberts J and Zhong S (2004) Plume-induced topography and geoid anomalies and their implications for the Tharsis rise on Mars. *Journal of Geophysical Research* 109: E03009. http://dx.doi.org/10.1029/2003JE002226.

Robinson EM and Parsons B (1988) Effect of a shallow low-viscosity zone on the formation of midplate swells. *Journal of Geophysical Research* 93: 3144–3156.

Rodríguez E, Morris CS, Belz JE, et al. (2005). An assessment of the SRTM topographic products. Technical Report. Jet Propulsion Laboratory.

Rogers PG and Zuber MT (1998) Tectonic evolution of Bell Regio, Venus: Regional stress, lithospheric flexure, and edifice stresses. *Journal of Geophysical Research* 103: 16841–16853.

Rosenblatt P, Pinet P, and Touvenot E (1994) Comparative hypsometric analysis of Earth and Venus. *Geophysical Research Letters* 21: 465–468.

Rosenburg MA, Aharonson O, Head JW, et al. (2011) Global surface slopes and roughness of the moon from the lunar orbiter laser altimeter. *Journal of Geophysical Research* 116: E02001. http://dx.doi.org/10.1029/2010JE003716.

Rummel R (2005) Gravity and topography of Moon and planets. *Earth, Moon, and Planets* 94: 103–111. http://dx.doi.org/10.1007/s11038-005-3245-z.

Rummel R, Yi W, and Stummer G (2011) GOCE gravitational gradiometry. *Journal of Geodesy* 85: 777–790. http://dx.doi.org/10.1007/s00190-011-0500-0.

Sandwell DT and Schubert G (1992) Flexural ridges, trenches, and outer rises around coronae on Venus. *Journal of Geophysical Research* 97: 16069–16083.

Sandwell DT and Smith WHF (1997) Marine gravity anomaly from Geosat and ERS 1 satellite altimetry. *Journal of Geophysical Research* 102: 10039–10054.

Saunders RS, Pettengill GH, Arvidson RE, Sjogren WL, Johnson WTK, and Pieri L (1990) The Magellan Venus radar mapping mission. *Journal of Geophysical Research* 95: 8339–8355. http://dx.doi.org/10.1029/JB095iB06p08339.

Scheeres DJ, Khushalani B, and Werner RA (2000) Estimating asteroid density distributions from shape and gravity information. *Planetary and Space Science* 48: 965–971.

Schmidt M, Fengler M, Mayer-Gürr T, et al. (2007) Regional gravity modeling in terms of spherical base functions. *Journal of Geodesy* 81: 17–38. http://dx.doi.org/10.1007/s00190-006-0101-5.

Scholten F, Oberst J, Matz KD, et al. (2012) GId100: The near-global lunar 100 m raster DTM from LROC WAC stereo image data. *Journal of Geophysical Research* 117: E00H17. http://dx.doi.org/10.1029/2011JE003926.

Schubert G and Sandwell DT (1995) A global survey of possible subduction sites on Venus. *Icarus* 117: 173–196.

Schubert G, Solomatov VS, Tackley PJ, and Turcotte DL (1997) Mantle convection and the thermal evolution of Venus. In: Bougher SW, Hunten DM, and Phillips RJ (eds.) *Venus II*, pp. 1245–1287. Tucson, AZ: University of Arizona Press.

Schutz BE, Zwally HJ, Shuman CA, Hancock D, and DiMarzio JP (2005) Overview of the ICESat mission. *Geophysical Research Letters* 32: L21S01. http://dx.doi.org/10.1029/2005GL024009.

Shuman C, Zwally HJ, Schutz BE, et al. (2006) ICESat Antarctic elevation data: Preliminary precision and accuracy assessment. *Geophysical Research Letters* 33: L07501. http://dx.doi.org/10.1029/2005GL025227.

Simons FJ and Dahlen FA (2006) Spherical Slepian functions and the polar gap in geodesy. *Geophysical Journal International* 166: 1039–1061. http://dx.doi.org/10.1111/j.1365-246X.2006.03065.x.

Simons FJ, Dahlen FA, and Wieczorek MA (2006) Spatiospectral concentration on a sphere. *SIAM Review* 48: 504–536. http://dx.doi.org/10.1137/S0036144504445765.

Simons FJ, van der Hilst RD, and Zuber MT (2003) Spatio-spectral localization of isostatic coherence anisotropy in Australia and its relation to seismic anisotropy: Implications for lithospheric deformation. *Journal of Geophysical Research* 108: 2250. http://dx.doi.org/10.1029/2001JB000704.

Simons FJ, Zuber MT, and Korenaga J (2000) Isostatic response of the Australian lithosphere: Estimation of effective elastic thickness and anisotropy using multitaper spectral analysis. *Journal of Geophysical Research* 105: 19163–19184.

Simons M, Hager BH, and Solomon SC (1994) Global variations in the geoid/topography admittance of Venus. *Science* 264: 798–803.

Simons M, Solomon SC, and Hager BH (1997) Localization of gravity and topography: Constraints on the tectonics and mantle dynamics of Venus. *Geophysical Journal International* 131: 24–44.

Sjogren WL, Banerdt WB, Chodas PW, et al. (1997) The Venus gravity field and other geodetic parameters. In: Bougher SW, Hunten DM, and Phillips RJ (eds.) *Venus II*, pp. 1125–1161. Tucson, AZ: University of Arizona Press.

Slepian D (1983) Some comments on Fourier-analysis, uncertainty and modeling. *SIAM Review* 25: 379–393.

Smith DE, Zuber MT, Frey HV, et al. (2001a) Mars Orbiter Laser Altimeter: Experiment summary after the first year of global mapping of Mars. *Journal of Geophysical Research* 106: 23689–23722.

Smith DE, Zuber MT, Jackson GB, et al. (2010a) The Lunar Orbiter Laser Altimeter investigation on the Lunar Reconnaissance Orbiter mission. *Space Science Reviews* 150: 209–241. http://dx.doi.org/10.1007/s11214-009-9512-y.

Smith DE, Zuber MT, and Neumann GA (2001b) Seasonal variations of snow depth on Mars. *Science* 294: 2141–2146.

Smith DE, Zuber MT, Neumann GA, and Lemoine FG (1997) Topography of the Moon from Clementine lidar. *Journal of Geophysical Research* 102: 1591–1611.

Smith DE, Zuber MT, Neumann GA, et al. (2010b) Initial observations from 81 the Lunar Orbiter Laser Altimeter (LOLA). *Geophysical Research Letters* 37: L18204. http://dx.doi.org/10.1029/2010GL043751.

Smith DE, Zuber MT, Phillips RJ, et al. (2012) Gravity field and internal structure of Mercury from MESSENGER. *Science* 336: 214–217. http://dx.doi.org/10.1126/science.1218809.

Smith DE, Zuber MT, Phillips RJ, et al. (2010c) The equatorial shape and gravity field of Mercury from MESSENGER flybys 1 and 2. *Icarus* 209: 88–100. http://dx.doi.org/10.1016/j.icarus.2010.04.007.

Smith DE, Zuber MT, Solomon SC, et al. (1999) The global topography of Mars and implications for surface evolution. *Science* 284: 1495–1503.

Smith WHF and Sandwell DT (1997) Global sea floor topography from satellite altimetry and ship depth soundings. *Science* 277: 1956–1962.

Smith WHF and Sandwell DW (1994) Bathymetric prediction from dense satellite altimetry and sparse shipboard bathymetry. *Journal of Geophysical Research* 99: 21803–21824.

Smrekar SE (1994) Evidence for active hotspots on Venus from analysis of Magellan gravity data. *Icarus* 112: 2–26.

Smrekar SE, Comstock R, and Anderson FS (2003) A gravity survey of type 2 coronae on Venus. *Journal of Geophysical Research* 108: 5090. http://dx.doi.org/10.1029/2002JE001935.

Smrekar SE and Stofan ER (1999) Origin of corona-dominated topographic rises on Venus. *Icarus* 139: 100–115.

Sneeuw N (1994) Global spherical harmonic-analysis by least-squares and numerical quadrature methods in historical perspective. *Geophysical Journal International* 118: 707–716.

Solomon SC and Head JW (1980) Lunar mascon basins: Lava filling, tectonics, and evolution of the lithosphere. *Reviews of Geophysics and Space Physics* 18: 107–141.

Solomon SC and Head JW (1990) Lithospheric flexure beneath the Frejya Montes foredeep, Venus: Constraints on lithospheric thermal gradient and heat flow. *Geophysical Research Letters* 17: 1393–1396.

Solomon SC, McNutt RL, Gold RE, et al. (2001) The MESSENGER mission to Mercury: Scientific objectives and implementation. *Planetary and Space Science* 49: 1445–1465. http://dx.doi.org/10.1016/S0032-0633(01)00085-X.

Spohn T, Sohl F, Wieczerkowski K, and Conzelmann V (2001) The interior structure of Mercury: What we know, what we expect from BepiColombo. *Planetary and Space Science* 49: 1561–1570. http://dx.doi.org/10.1016/S0032-0633(01)00093-9.

Sugano T and Heki K (2004) Isostasy of the Moon from high-resolution gravity and topography data: Implication for its thermal history. *Geophysical Research Letters* 31: L24703. http://dx.doi.org/10.1029/2004GL022059.

Tapley B, Ries J, Bettadpur S, et al. (2005) GGM02—An improved Earth gravity field model from GRACE. *Journal of Geodesy* 79. http://dx.doi.org/10.1007/s00190-005-0480-z.

Tapley BD, Bettadpur S, Ries JC, Thompson PF, and Watkins M (2004) GRACE measurements of mass variability in the Earth system. *Science* 305: 503–505.

Taylor GJ, Boynton W, Brückner J, et al. (2006) Bulk composition and early differentiation of Mars. *Journal of Geophysical Research* 111: 3. http://dx.doi.org/10.1029/2005JE002645.

Thébault E, Schott JJ, and Mandea M (2006) Revised spherical cap harmonic analysis (R-SCHA): Validation and properties. *Journal of Geophysical Research* 111. http://dx.doi.org/10.1029/2005JB003836.

Thébault E, Schott JJ, Mandea M, and Hoffbeck JP (2004) A new proposal for spherical cap harmonic modelling. *Geophysical Journal International* 159: 83–103.

Thomas PC (2010) Sizes, shapes, and derived properties of the Saturnian satellites after the Cassini nominal mission. *Icarus* 208: 395–401. http://dx.doi.org/10.1016/j.icarus.2010.01.025.

Thomas PC, Burns JA, Helfenstein P, et al. (2007) Shapes of the Saturnian icy satellites and their significance. *Icarus* 190: 573–584.

Thomas PC, Davies ME, Colvin TR, et al. (1998) The shape of Io from Galileo limb measurements. *Icarus* 135: 175–180. http://dx.doi.org/10.1006/icar.1998.5987.

Thomson DJ (1982) Spectrum estimation and harmonic analysis. *Proceedings of the IEEE* 70: 1055–1096.

Tsoulis D, Jamet O, Verdun J, and Gonindard N (2009) Recursive algorithms for the computation of the potential harmonic coefficients of a constant density polyhedron. *Journal of Geodesy* 83: 925–942. http://dx.doi.org/10.1007/s00190-009-0310-9.

Turcotte DL (1995) How does Venus lose heat? *Journal of Geophysical Research* 100: 16931–16940.

Turcotte DL, Willemann RJ, Haxby WF, and Norberry J (1981) Role of membrane stresses in the support of planetary topography. *Journal of Geophysical Research* 86: 3951–3959. http://dx.doi.org/10.1029/JB086iB05p03951.

U. S. Geological Survey (2002) Color-coded topography and shaded relief map of the lunar near side and far side hemispheres I-2769.

Varshalovich DA, Moskalev AN, and Khersonskii VK (1988) *Quantum Theory of Angular Momentum*. Singapore: World Scientific.

Vaughan WM, Head JW, Wilson L, and Hess PC (2013) Geology and petrology of enormous volumes of impact melt on the Moon: A case study of the Orientale basin impact melt sea. *Icarus* 223: 749–765. http://dx.doi.org/10.1016/j.icarus.2013.01.017.

Vezolainen AV, Solomatov VS, Basilevsky AT, and Head JW (2004) Uplift of Beta Regio: Three-dimensional models. *Journal of Geophysical Research* 109: E08007. http://dx.doi.org/10.1029/2004JE002259.

Vondrak R, Keller J, Chin G, and Garvin J (2010) Lunar reconnaissance orbiter (LRO): Observations for lunar exploration and science. *Space Science Reviews* 150: 7–22. http://dx.doi.org/10.1007/s11214-010-9631-5.

Wählisch M, Willner K, Oberst J, et al. (2010) A new topographic image atlas of Phobos. *Earth and Planetary Science Letters* 294: 547–553. http://dx.doi.org/10.1016/j.epsl.2009.11.003.

Wandelt BD and Gòrski KM (2001) Fast convolution on the sphere. *Physical Review D* 63: 123002. http://dx.doi.org/10.1103/PhysRevD.63.123002.

Ward WR (1975) Past orientation of the lunar spin axis. *Science* 189: 377–379.

Watters T (2003) Lithospheric flexure and the origin of the dichotomy boundary on Mars. *Geology* 31: 271–274.

Watts AB (2001) *Isostasy and Flexure of the Lithosphere*. Cambridge, UK: Cambridge University Press.

Watts AB and Burov EB (2003) Lithospheric strength and its relationship to the elastic and seismogenic layer thickness. *Earth and Planetary Science Letters* 213: 113–131.

Watts AB and Zhong S (2000) Observations of flexure and the rheology of oceanic lithosphere. *Geophysical Journal International* 142: 855–875.

Webb DJ (1982) Tides and the evolution of the Earth–Moon system. *Geophysical Journal of the Royal Astronomical Society* 70: 261–271.

Werner RA (1997) Spherical harmonic coefficients for the potential of a constant density polyhedron. *Computers & Geosciences* 23: 1071–1077.

Werner RA and Scheeres DJ (1997) Exterior gravitation of a polyhedron derived and compared with harmonic and mascon gravitation representations of asteroid 4769 Castalia. *Celestial Mechanics and Dynamical Astronomy* 65: 313–344.

Wessel P and Smith WHF (1991) Free software helps map and display data. *Eos, Transactions, American Geophysical Union* 72.

Wiaux Y, McEwen J, and Vielva P (2007) Complex data processing: Fast wavelet analysis on the sphere. *Journal of Fourier Analysis and Applications* 13: 477–493. http://dx.doi.org/10.1007/s00041-006-6917-9.

Wieczorek M and Phillips RJ (1999) Lunar multiring basins and the cratering process. *Icarus* 139: 246–259.

Wieczorek MA (2008) Constraints on the composition of the Martian south polar cap from gravity and topography. *Icarus* 196: 506–517. http://dx.doi.org/10.1016/j.icarus.2007.10.026.

Wieczorek MA, Jolliff BJ, Khan A, et al. (2006) The constitution and structure of the lunar interior. In: Jolliff BJ, Wieczorek MA, Shearer CK, and Neal CR (eds.) *New Views of the Moon. Reviews in Mineralogy and Geochemistry*, vol. 60, pp. 221–364. Mineralogical Society of America.

Wieczorek MA and Le Feuvre M (2009) Did a large impact reorient the Moon? *Icarus* 200: 358–366. http://dx.doi.org/10.1016/j.icarus.2008.12.017.

Wieczorek MA, Neumann GA, Nimmo F, et al. (2013) The crust of the Moon as seen by GRAIL. *Science* 339: 671–675. http://dx.doi.org/10.1126/science.1231530.

Wieczorek MA and Phillips RJ (1997) The structure and compensation of the lunar highland crust. *Journal of Geophysical Research* 102: 10933–10943.

Wieczorek MA and Phillips RJ (1998) Potential anomalies on a sphere: Applications to the thickness of the lunar crust. *Journal of Geophysical Research* 103: 1715–1724. http://dx.doi.org/10.1029/97JE03136.

Wieczorek MA and Simons FJ (2005) Localized spectral analysis on the sphere. *Geophysical Journal International* 162: 655–675. http://dx.doi.org/10.1111/j.1365-246X.2005.02687.x.

Wieczorek MA and Simons FJ (2007) Minimum-variance multitaper spectral estimation on the sphere. *Journal of Fourier Analysis and Applications* 13: 665–692. http://dx.doi.org/10.1007/s00041-006-6904-1.

Wieczorek MA and Zuber MT (2004) Thickness of the Martian crust: Improved constraints from geoid-to-topography ratios. *Journal of Geophysical Research* 109: E01009. http://dx.doi.org/10.1029/2003JE002153.

Willemann RJ and Turcotte DL (1981) Support of topographic and other loads on the Moon and on the terrestrial planets. *Lunar and Planetary Science Conference* 12B: 837–851.

Williams JG, Boggs DH, and Folkner WM (2013) *DE430 Lunar Orbit, Physical Librations, and Surface Coordinates*. Jet Propulsion Laboratory, Interoffice Memorandum IOM 335-JW,DB,WF-20130722-016, July 22.

Williams JG, Konopliv AS, Boggs DH, et al. (2014) Lunar interior properties from the GRAIL mission. *Journal of Geophysical Research: Planets*, in press.

Williams JP, Ruiz J, Rosenburg MA, Aharonson O, and Phillips RJ (2011) Insolation driven variations of Mercury's lithospheric strength. *Journal of Geophysical Research* 116: E01008. http://dx.doi.org/10.1029/2010JE003655.

Yamamoto S, Nakamura R, Matsunaga T, et al. (2010) Possible mantle origin of olivine around lunar impact basins detected by SELENE. *Nature Geoscience* 3: 533–536. http://dx.doi.org/10.1038/ngeo897.

Yoder CF (1995) Astrometric and geodetic properties of Earth and the solar system. In: Ahrens TJ (ed.) *Global Earth Physics: A Handbook of Physical Constants. AGU Reference Shelf*, vol. 1, pp. 1–31. American Geophysical Union.

Yuan DN, Sjogren WL, Konopliv AS, and Kucinskas AB (2001) Gravity field of Mars: A 75th degree and order model. *Journal of Geophysical Research* 106: 23377–23401.

Zharkov VN, Leontjev VV, and Kozenko AV (1985) Models, figures and gravitational moments of the Galilean satellites of Jupiter and icy satellites of Saturn. *Icarus* 61: 92–100.

Zhong S (2002) Effects of lithosphere on the long-wavelength gravity anomalies and their implications for the formation of the Tharsis rise on Mars. *Journal of Geophysical Research* 107: 5054. http://dx.doi.org/10.1029/2001JE001589.

Zuber M, Smith D, Lehman D, Hoffman T, Asmar S, and Watkins M (2013a) Gravity Recovery and Interior Laboratory (GRAIL): Mapping the lunar interior from crust to core. *Space Science Reviews:* 1–22. http://dx.doi.org/10.1007/s11214-012-9952-7.

Zuber MT (2001) The crust and mantle of Mars. *Nature* 412: 237–244.

Zuber MT, Bechtel TD, and Forsyth DW (1989) Effective elastic thicknesses of the lithosphere and mechanisms of isostatic compensation in Australia. *Journal of Geophysical Research* 94: 9353–9367.

Zuber MT, Phillips RJ, Andrews-Hanna JC, et al. (2007) Density of Mars' south polar layered deposits. *Science* 317: 1718–1719. http://dx.doi.org/10.1126/science.1146995.

Zuber MT and Smith DE (1997) Mars without Tharsis. *Journal of Geophysical Research* 102: 28673–28685.

Zuber MT, Smith DE, Cheng AF, et al. (2000a) The shape of 433 Eros from the NEAR-Shoemaker Laser Rangefinder. *Science* 289: 2097–2101.

Zuber MT, Smith DE, Lemoine FG, and Neumann GA (1994) The shape and internal structure of the Moon from the Clementine mission. *Science* 266: 1839–1843. http://dx.doi.org/10.1126/science.266.5192.1839.

Zuber MT, Smith DE, Phillips RJ, et al. (2012) Topography of the northern hemisphere of Mercury from MESSENGER laser altimetry. *Science* 336: 217–220. http://dx.doi.org/10.1126/science.1218805.

Zuber MT, Smith DE, Solomon SC, et al. (2008) Laser altimeter observations from MESSENGER's first Mercury flyby. *Science* 321: 77–79. http://dx.doi.org/10.1126/science.1159086.

Zuber MT, Smith DE, Watkins MM, et al. (2013b) Gravity field of the Moon from the Gravity Recovery and Interior Laboratory (GRAIL) mission. *Science* 339: 668–671. http://dx.doi.org/10.1126/science.1231507.

Zuber MT, Solomon SC, Phillips RJ, et al. (2000b) Internal structure and early thermal evolution of Mars from Mars Global Surveyor topography and gravity. *Science* 287: 1788–1793.